SYNTHESIS, CHARACTERIZATION AND APPLICATION OF MOLYBDENUM DISULFIDE NANOMATERIALS

CHUI YING SAN

DOCTOR OF PHILOSOPHY

CITY UNIVERSITY OF HONG KONG

SEPTEMBER 2014

CITY UNIVERSITY OF HONG KONG
香港城市大學

Synthesis, Characterization and Application of Molybdenum Disulfide Nanomaterials
二硫化鉬納米材料的制備、表徵與應用

Submitted to
Department of Physics and Materials Science
物理及材料科學系
in Partial Fulfillment of the Requirements
for the Degree of Doctor of Philosophy
哲學博士學位

by

CHUI Ying San
崔應新

September 2014
二零一四年九月

Abstract

Graphene has attracted intensive research interest in the recent few years mainly due to its unique two-dimensionality and remarkable high carrier mobility. However, pristine graphene lacks a bandgap that limits its electronic and optoelectronic applications. Molybdenum disulfide (MoS_2) is a typical type of transition metal dichalcogenides (TMDs) having a layered structure analogous to graphite, with strong in-plane covalent bonding and weak out-of-plane van der Waals interactions. In contrast to graphene, monolayer MoS_2 possesses an intrinsic direct bandgap of ~1.8 eV that is able to complement graphene as two-dimensional semiconductors. On the other hand, nanostructured MoS_2 also shows promising for sensing, lithium-ion storage and electrocatalytic applications. MoS_2 is an emerging material that offers great opportunities for the exploration of new chemical and physical properties beyond graphene. In this thesis, main efforts were devoted to the synthesis, characterization and application of MoS_2 nanomaterials. Si-based lithium-ion battery (LIB) was also introduced in correlated to the up-rising concern of energy related application of nanomaterials.

In this work, large-area MoS_2 atomically thin layer was successfully synthesized by direct sulfurization of pre-deposited MoO_3 thin film on SiO_2/Si substrate. The size of MoS_2 atomic layer that can be prepared depended on the size of the receiving

substrate. The emerging PL signal at 652 nm indicated the as-synthesized MoS_2 atomic layer was optically active with a direct bandgap. Both Raman spectroscopy and AFM measurement confirmed bi-layer thickness of the MoS_2 atomic layer. Raman and PL mappings revealed the optical signals of the MoS_2 atomic layer were uniform over a large area. The facile sulfurization and preparation of MoS_2 atomic layer paved the way for the synthesis of large-area 2D semiconductor for future integrated circuits.

Since the MoS_2 atomic layer prepared by sulfurization was reported to be polycrystalline with nanoscale grain size, CVD method was applied to synthesize MoS_2 layer with larger grain size. The CVD synthesis of MoS_2 was conducted at different pressures in order to study its growth behaviors. Experimental results showed that both sulfur concentration and pressure played important roles for 2D MoS_2 growth. While large-area MoS_2 film can be obtained at vacuum, MoS_2 triangular flakes with size of about 20 μm were synthesized under pressure. Larger MoS_2 layer can be formed when the MoS_2 triangular flakes grew and merge with each other. The emerging of PL peaks manifested direct exitonic transition of the as-synthesized 2D MoS_2 layers.

In addition to the preparation of 2D MoS_2 atomic layers, MoS_2 nanosphere network was synthesized via facile one-step PVP-assisted hydrothermal reaction. The

size of the MoS_2 nanospheres decreased with increasing the PVP concentration. The MoS_2 nanospheres interlinked with each other forming a network, and were characterized to have randomly oriented layers with expanded interlayer separation in the (002) plane. LIBs with anode based on the MoS_2 nanosphere network demonstrated enhanced electrochemical performance, with a high reversible capacity of ~850 mA h g^{-1} at current density of 0.5 C for 200 cycles. The electrochemical enhancement can be attributed to unique structure of the MoS_2 nanosphere network which facilitated both electronic and ionic transports. Apart from LIB application, the MoS_2 nanosphere network also showed significant enhancement for hydrogen evolution reaction (HER). The enhancement can be ascribed to the expanded interlayer distance in the (002) plane which exposed the reactive edge sites for electrochemical reactions.

In the research of nanomaterials for LIB, it is worth to mention Si for its highest theoretical specific capacity of ~4200 mA h g^{-1} for LIB application. However, the severe pulverization of Si upon the lithiation and delithiation processes restricts it from practical implementation. In this work, 3D porous Cu supported Si thin film was introduced as LIB anode and delivered a high reversible capacity of ~2500 mAh g^{-1} at current density of 0.33 C. A remarkable reversible capacity of 955 mAh g^{-1} was retained even under high current density of 3 C after 2000 cycles. The high

performance of the Si anode can be ascribed to the unique structure of the 3D porous Cu skeleton, which allowed facile strain relaxation of Si during cycling, and imparted both structural reinforcement and electrical pathway to the Si active material.

CITY UNIVERSITY OF HONG KONG

Qualifying Panel and Examination Panel

Surname:	CHUI
First Name:	Ying San
Degree:	Doctor of Philosophy
College/Department:	Department of Physics & Materials Science

The Qualifying Panel of the above student is composed of:

Supervisor(s)

Prof. ZHANG Wenjun	Department of Physics & Materials Science City University of Hong Kong

Co-supervisor(s)

Dr. Juan Antonio ZAPIEN	Department of Physics & Materials Science City University of Hong Kong

Qualifying Panel Member(s)

Dr. LI Yangyang	Department of Physics & Materials Science City University of Hong Kong

This thesis has been examined and approved by the following examiners:

Dr. VELLAISAMY Arul Lenus Roy	Department of Physics & Materials Science City University of Hong Kong
Prof. LEE Chun Sing	Department of Physics & Materials Science City University of Hong Kong
Prof. ZHANG Wenjun	Department of Physics & Materials Science City University of Hong Kong
Dr. YAN Feng	Department of Applied Physics The Hong Kong Polytechnic University

Acknowledgements

I would like to take this opportunity to express my deep and sincere gratitude to my Ph. D supervisor, Prof. Wenjun Zhang, for his invaluable guidance, full support and constant encouragement that greatly helped me finishing my Ph. D study and research at City University of Hong Kong.

I would like to thank Prof. Shuit-Tong Lee, Prof. Chun-Sing Lee and Dr. Juan Antonio Zapien, for their generous advices and invaluable suggestions on my Ph. D research.

I want to thank Mr. Felix Wong and Mr. Kin Wai Tong for their technical supports and experimental assists throughout my study.

Also, I would like to appreciate all the members and staffs of COSDAF, especially Dr. Chundong Wang and Dr. Jian-An Huang, for their precious discussion and help.

Finally, I would like to express my deep thanks to my Parents, whose endless support and encouragement enable me to complete this work.

Table of Contents

List of Figures

Lists of Symbols and Abbreviations

2D	Two-dimensional
3D	Three-dimensional
AFM	Atomic Force Microscope
Ar^+	Argon Ion
CBM	Conduction Band Minimum
CH_4N_2S	Thiourea
Cu	Copper
CV	Cyclic Voltammetric
CVD	Chemical Vapor Deposition
DFT	Density Functional Theory
EDX	Energy-dispersive X-ray
EIS	Electrochemical Impedance Spectroscopy
FET	Field Effect Transistor
HER	Hydrogen Evolution Reaction
HfO_2	Hafnium(IV) Oxide
HRTEM	High Resolution Transmission Electron Microscope
Li	Lithium
LIB	Lithium-ion battery
$LiPF_6$	Lithium Hexafluorophosphate
Mo	Molybdenum
MoO_3	Molybdenum(VI) Oxide
MoS_2	Molybdenum(IV) Sulfide / Molybdenum Disulfide
$MoSe_2$	Molybdenum(IV) Selenide
MOSFET	Metal-oxide-semiconductor Field-effect Transistor
$(NH_4)_6Mo_7O_{24}\cdot 4H_2O$	Ammonium Molybdate Tetrahydrate
$(NH_4)_2\ MoS_4$	Ammonium Thiomolybdates
NO	Nitrogen Monoxide
NO_2	Nitrogen Dioxide
OLED	Organic Light Emitting Diode
OM	Optical Microscope
Pa	Pascal
PL	Photoluminescence
PS	Polystyrene
PTAS	Perylene-3,4,9,10-tetracarboxylic Acid Tetrapotassium Salt
PTCDA	Perylene-3,4,9,10-tetracarboxylic Dianhydride

PVP	Polyvinylpyrrolidone
rGO	Reduced Graphene Oxide
S	Sulfur
sccm	Standard Cubic Centimeter per Minute
Se	Selenium
SEI	Solid-electrolyte Interface
SEM	Scanning Electron Microscope
Si	Silicon
SiO_2	Silicon Dioxide
TEM	Transmission Electron Microscope
TFT	Thin Film Transistor
TMDs	Transition Metal Dichalcogenides
VBM	Valence Band Maximum
WS_2	Tungsten(IV) Sulfide
WSe_2	Tungsten(IV) Selenide
XPS	X-ray Photoelectron Spectroscopy
XRD	X-ray Diffraction

Chapter 1 Introduction

1.1 2D Materials beyond Graphene and the Emerging of MoS_2 Nanomaterials

An atomically thin two-dimensional (2D) material is defined as a material in which free charge carriers are immobile in one spatial dimension but mobile in the other two dimensions.[1] This unique property enables 2D materials to have new or superior functions that are distinct from thin films and their bulk counterparts. Many 2D materials exist in bulk form as stack layers with strong intralayer bonding and weak interlayer attraction, which allows to exfoliate into individual and atomically thin layers.[2] In 2004, the successful exfoliation of graphite into atomically thin 2D graphene aroused the research interest of 2D materials. In the past few years, graphene has received tremendous attention and it is often regarded as "wonder material" of the 21st century due to its exceptional carrier mobility, thermal conductivity, optical and mechanical properties.[3,4] However, the zero energy bandgap of graphene hinders its semiconducting applications such as transistors.[5] Although bandgap can be engineered in graphene by nanostructuring,[6-8] chemical functionalization[9] or applying a high electric field to bilayer graphene,[10] these methods increase complexity and decrease mobility. In contrast, several 2D transition metal dichalcogenides (TMDs) possess intrinsic bandgaps at around 1-2 eV, which can complement graphene and show promising application for 2D electronic and

optoelectronic devices.[11]

TMDs have a graphite-like layered structure with the formula MX_2, where M is a transition metal element and X is a chalcogen (S, Se or Te) as highlighted in figure 1.1. Partial highlights for Co, Rh, Ir and Ni indicate only some of the dichalcogenides form layered structures.[12] Figure 1.2 summarizes the properties of different layered TMDs. Since these layered structures are weakly bonded by van der Waals interaction like graphite, they can be easily exfoliated and their 2D counterparts usually show distinct properties which open up opportunities for new physics. In 2010, Mak *et al.* systematically examined the thickness dependent of the photoluminescent (PL), absorption and photoconductivity spectra of MoS_2, and the experimental results reveal that MoS_2 undergoes a transition from indirect to direct bandgap when its thickness is thinned down to monolayer.[13] This discovery then sparked research interest in 2D TMDs.

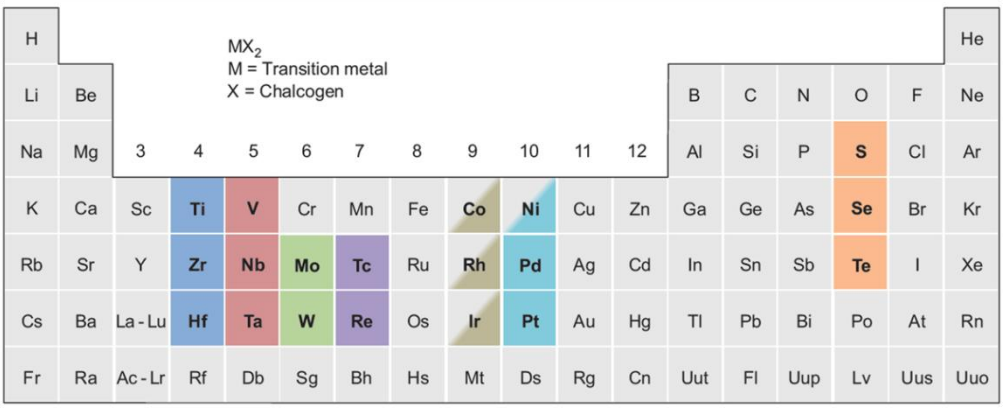

Figure 1.1 Highlight of transition metal elements and chalcogens for the composition of layered transition metal dichalcogenides (TMDs) in periodic table.[12]

Group	M	X	Properties
4	Ti, Hf, Zr	S, Se, Te	Semiconducting (E_g = 0.2–2 eV). Diamagnetic.
5	V, Nb, Ta	S, Se, Te	Narrow band metals (ρ ~ 10^{-4} Ω.cm) or semimetals. Superconducting. Charge density wave (CDW). Paramagnetic, antiferromagnetic, or diamagnetic.
6	Mo, W	S, Se, Te	Sulfides and selenides are semiconducting (E_g ~ 1 eV). Tellurides are semimetallic (ρ ~ 10^{-3} Ω cm). Diamagnetic.
7	Tc, Re	S, Se, Te	Small-gap semiconductors. Diamagnetic.
10	Pd, Pt	S, Se, Te	Sulfides and selenides are semiconducting (E_g = 0.4 eV) and diamagnetic. Tellurides are metallic and paramagnetic. $PdTe_2$ is superconducting.

ρ, in-plane electrical resistivity.

Figure 1.2 Properties of different layered TMDs.[14]

With an intrinsic direct bandgap of 1.8 eV, 2D MoS_2 has been demonstrated excellent performance in semiconducting applications. For instant, field effect transistor (FET) based on monolayer MoS_2 showed an on/off ratio exceeding 10^8 at room temperature,[15] outperforms that based on graphene. Currently, the feature length of Si-based metal-oxide-semiconductor field-effect transistors (MOSFETs) is 18 nm and subsequent reduction in scale is approaching limits due to quantum effects and difficulty in heat dissipation.[16] As a 2D semiconductor, atomically thin MoS_2 is promising to replace Si for the next generation MOSFET. Similar to graphene, 2D MoS_2 shows excellent mechanical properties, making it attractive for flexible electronic and optoelectronic devices.[17] Apart from 2D MoS_2, MoS_2 nanomaterials also show potential applications in energy related field such as lithium-ion battery

(LIB) and hydrogen evolution reaction (HER). MoS_2 has become one of the most promising materials beyond graphene in multidiscipline application fields.

1.2 Structures and Properties of 2D MoS_2

1.2.1 Crystal Structure

MoS_2 crystals are naturally occurred in the Earth crust. They have a stacked layered structure of the form S-Mo-S, in which each layer is constituted by one hexagonal plane of Mo atoms sandwiched between two hexagonal planes of S atoms, with layer thickness of 0.6-0.7 nm.[12] The intralayer bonding is strong covalent interaction while adjacent layers are held by weak van der Waals force, allowing them to be readily exfoliated into thin layers.[13] Two structural polytypes, 2H and 3R, can be identified in naturally occurred MoS_2.[18,19] Both have a trigonal prismatic coordination. While 2H-MoS_2 is dominant and more stable in nature, having two layers per unit cell stacked in hexagonal symmetry, 3R-MoS_2 has three layers per unit cell in rhombohedral symmetry and it can transform to 2H phase upon heating.[19] In case of MoS_2 nanosheets that are prepared by chemical exfoliation other than mechanical exfoliation, the MoS_2 nanosheets will undergo a phase transformation to a 1T metastable structure in which the coordination of Mo atoms becomes octahedral.[20] The 1T phase will transform back to the 2H phase under moderate annealing.[21] Figure 1.3 schematically summarizes the three structural polytypes of MoS_2.

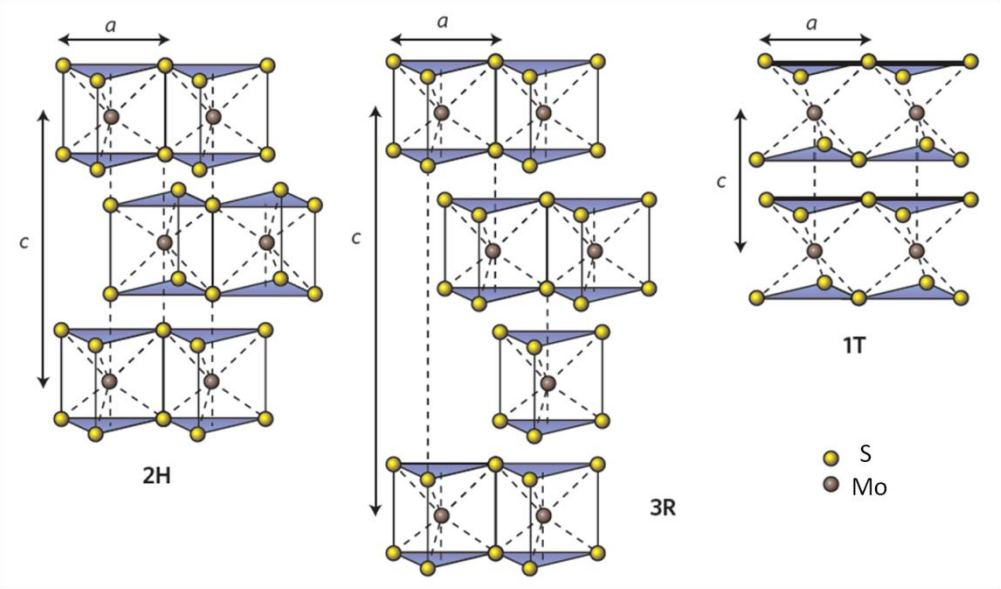

Figure 1.3 Schematic of MoS_2 structural polytypes.[11]

1.2.2 Mechanical Properties

The elastic properties of exfoliated MoS_2 nanosheets with thickness ranging from 5 to 25 layers were examined by Castellanos-Gomez *et at.* and they found that the average Young's modulus of MoS_2 nanosheets is comparable to that of graphene oxide, with value 0.33 ± 0.07 TPa, which is higher than that of bulk MoS_2 (0.24 TPa) mainly due to lower density of stacking faults present in nanosheets.[22] The nanosheets also exhibited low pre-strain and could elastically deform up to tens of nanometers without breaking. Another work conducted by Bertolazzi *et al.* shows that the measured Young's modulus of single-layer MoS_2 was about 0.27 TPa, which was lower than that of multi-layers but higher than that of bulk MoS_2.[23] The measured strength of single-layer MoS_2 was 6-11% of its Young's Modulus, which approaches

the theoretical upper limit of a material's breaking strength. The exceptional elastic properties of single- and multi-layer MoS_2 nanosheets make them attractive 2D semiconductors for flexible electronic and optoelectronic devices.[17]

1.2.3 Electronic Structure

Bulk MoS_2 is a semiconductor with an indirect bandgap of 1.29 eV.[13] When the MoS_2 thickness decreases down to single layer, there is a dramatic changes of the electronic structure where single-layer MoS_2 possesses a direct bandgap of 1.90 eV.[13] Figure 1.4 shows the band structures of bulk and few- to single-layer MoS_2 calculated by first principles density functional theory (DFT). The red and blue lines respectively indicate the conduction band and valence band edges while the horizontal dash lines represent the energy of band maximum at the K point. The band structures show that bulk MoS_2 has an indirect bandgap with a valence band maximum (VBM) at the Γ point and a conduction band minimum (CBM) at the middle of the Γ-K symmetry line. With reduced layer thickness, the indirect bandgap becomes larger while the direct excitonic transition at the K point remains relatively unchanged. For single-layer MoS_2, it becomes a direct bandgap material with both VBM and CBM coinciding at the K point. Such indirect- to direct- bandgap transition of MoS_2 is due to quantum confinement and changes in interlayer coupling when the thickness going from bulk form to single layer.[13]

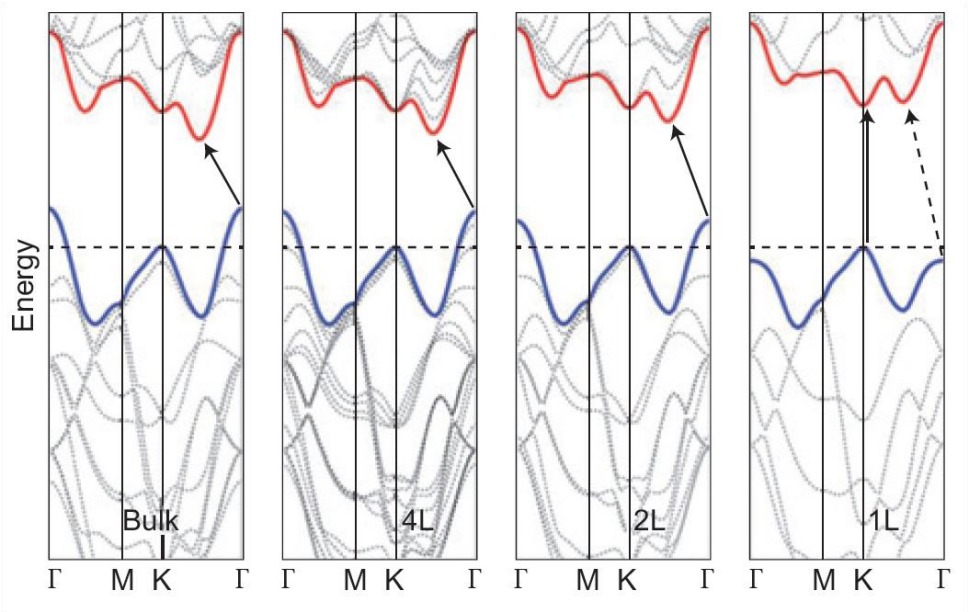

Figure 1.4 Calculated band structures of MoS_2 with different layer number.[24]

1.2.4 Optical Properties

1.2.4.1 Photoluminescence

The indirect- to direct-bandgap transition of MoS_2 when going from the bulk form to single layer is manifested in its photoluminescence (PL). Figure 1.5 shows the evolution of PL of MoS_2 with thickness gradually decreased to single layer. For bulk MoS_2, there is no observable PL due to its indirect bandgap nature. But when the MoS_2 thickness decreased down to 6 layers or less, two PL peaks appear at about 675 nm and 620 nm respectively corresponding to A1 and B1 direct excitonic transition,[24-26] whereas the PL is the strongest for single layer MoS_2 mainly due to much slower electronic relaxation arising from its unique electronic structure.[24] The occurrence of the two PL peaks is due to the spin-orbital splitting of the valence

band.[25,26] The emerging PL of single layer MoS_2 is consistent with the theoretical prediction of indirect- to direct-bandgap transition when going from the bulk to single layer MoS_2.

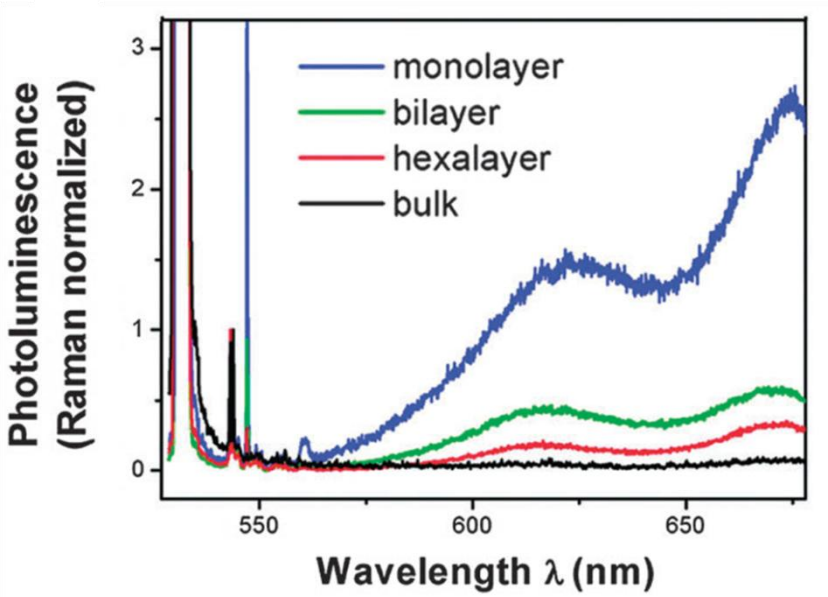

Figure 1.5 Emerging photoluminescence in single layer MoS_2.[24]

1.2.4.2 Raman Scattering

It is interesting to characterize how the week van der Waals interlayer interaction affects the intralayer bonding and lattice vibrations of MoS_2, like graphene. Figure 1.6 (a) shows the Raman spectra of bulk MoS_2 and few layer to single layer MoS_2. All the Raman spectra shows two vibrational modes, E^1_{2g} and A_{1g}, which respectively represents the in-plane and out-of-plane vibrational mode of MoS_2,[27] as schematically illustrated in the inset figure 1.6 (b). With increasing the layer number, it can be noted that the frequency of E^1_{2g} peak decreases while that of A_{1g} peak

increases. It can be explained that when the layer number increases, the interlayer van der Waals interaction of MoS_2 suppresses atom vibrations and resulting in larger force constants.[28] Both the E^1_{2g} and A_{1g} vibrational modes are supposed to shift to higher frequencies. But in reality, only the blue-shift of A_{1g} mode with increasing layer number is consistent with such prediction. For E^1_{2g} mode, it shows a red-shift instead of blue shift, suggesting the increase of interlayer van der Waals interaction shows little influence while stacking-induced structural changes or long-range interlayer Coulombic interactions in multilayer MoS_2 may play an important role to the changes of atomic vibration.[29,30] For MoS_2 with 4 or more layers, the frequencies of both vibrational modes are comparable to the bulk values.

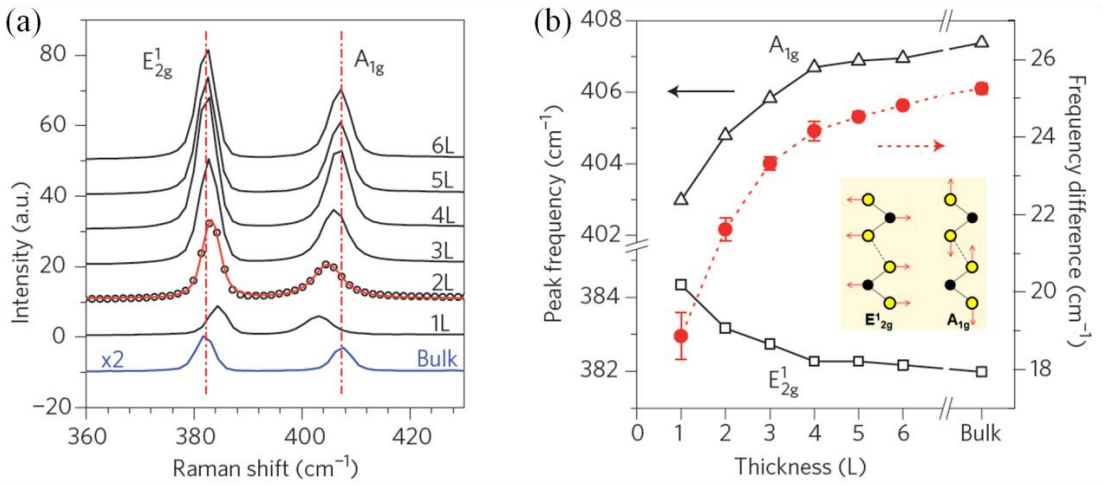

Figure 1.6 (a) Raman spectra of bulk MoS_2 and few layer to single layer MoS_2. (b) Frequency of E^1_{2g} and A_{1g} Raman modes (left vertical axis) and their frequency difference (right vertical axis) as a function of layer number. The inset schematically illustrate the E^1_{2g} and A_{1g} Raman modes of MoS_2.[29]

Figure 1.6 (b) shows the MoS_2 peak frequency of E^1_{2g} and A_{1g} Raman modes and their difference as a function of layer number. It is important to note that the peak frequency difference between the E^1_{2g} and A_{1g} modes can offer a convenient and preliminary estimation of the MoS_2 layer thickness. For single layer MoS_2, the peak frequency difference is below 20 cm^{-1}.

1.3 Synthesis of 2D MoS_2

To obtain high quality 2D MoS_2, mechanical exfoliation of bulk MoS_2 crystal is the best method but with low throughput. Liquid exfoliation can achieve mass production for application, but the as-exfoliated 2D MoS_2 flakes are usually defect rich which hinder electronic applications requiring high carrier mobility. For practical application, it is necessary to develop synthesis methods for large area and high quality 2D MoS_2. Below is the review of methods for the preparation of 2D MoS_2 and is categorized into top-down and bottom-up approaches.

1.3.1 Top-down Approach

1.3.2.1 Mechanical Exfoliation

Due to the week interlayer van der Waals interaction of MoS_2, mechanical exfoliation is a convenient method to obtain 2D MoS_2,[5] similar to the case of graphene. In a typical practice, a freshly exposed surface of MoS_2 crystal is rubbed

against a target substrate (e.g. SiO_2/Si wafer) and flakes of crystal will be detached and leave on the substrate surface.[5] Single layer MoS_2 can always be found among thicker flakes. A similar method by using scotch tape-based micromechanical exfoliation can also effectively obtain single layer MoS_2.[15] Figure 1.7 shows the optical microscope (OM) images and the corresponding AFM images of single layer and bilayer MoS_2 crystal flakes on SiO_2/Si substrate.

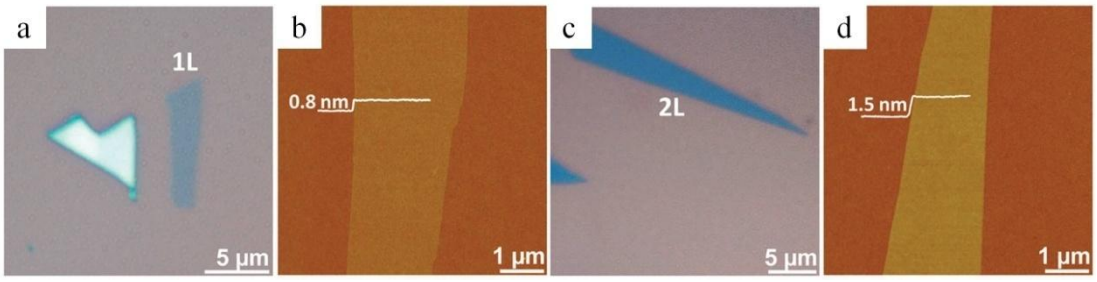

Figure 1.7 OM images (a and c) and corresponding AFM images (b and d) of (a and b) single layer MoS_2 and (c and d) bilayer MoS_2.[31]

Mechanical exfoliation can obtain high quality pristine single-crystal 2D MoS_2 flakes which are suitable for fundamental characterization and for fabrication of individual devices.[11] However, this method is not scalable and the thickness and size of the flakes cannot be systematically controlled.[11]

1.3.2.2 Liquid Exfoliation

Although mechanical exfoliation can produce pristine 2D MoS_2, its low throughput resists it from practical applications. On the other hand, liquid phase exfoliation is able to realize mass production of 2D MoS_2 and allows forming

functional composites with other materials for applications such as thin film devices.[17,32,33] The suspension of liquid exfoliated 2D MoS_2 can be facilely form thin films or coatings by filtration, inject printing, spray coating and doctor blading.[11]

Liquid exfoliation of TMDs, and here, MoS_2, is usually assisted with ionic species[34-39] to intercalate into interlayers for exfoliation. The intercalation method was first introduced in the 1975[39] and the intercalation-driven exfoliation of TMDs was later demonstrated in 1986.[35] This method involves putting bulk MoS_2 powder in a lithium-containing solution overnight to allow lithium ions intercalating into the interlayers, followed by mixing the intercalated material with water. The water then reacts strongly with the lithium, generating hydrogen gas which pushes adjacent layers apart and promotes the exfoliation of the layers.[11,35,37]

Recently, electrochemical Li-intercalation and exfoliation method has been developed to produce 2D TMDs in a more effective way.[38,40] Figure 1.8 (a) schematically shows the experimental procedure of this method. In short, layered bulk material such as MoS_2 is used as cathode and Li foil is used as anode in a Li-ion battery setup. After a discharge process where Li-ion intercalation occurs, the Li-intercalated material is sonicated in water or ethanol to obtain 2D MoS_2 nanosheets. Figure 1.8 (b) and (c) respectively shows the TEM image and AFM image of the as-exfoliated 2D MoS_2 nanosheets. The inset of figure 1.8 (b) shows the solution of

MoS_2 nanosheets with good dispersion. This method is able to provide high yield of single layer MoS_2 (~92% after purification) within 6 hours in room temperature, in contrast to traditional exfoliation methods which require high temperature (e.g. 100^oC) and long reaction time (more than a day).[41,42] In addition, it allows well-control of the Li-intercalation process by monitoring the discharge curve to avoid insufficient Li-intercalation resulting in low yield of product, or over Li-intercalation leading to structural decomposition of the 2D MoS_2 nanosheets.[17]

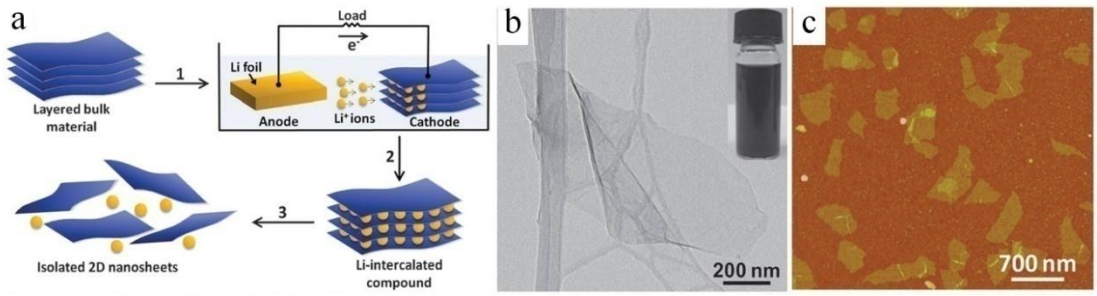

Figure 1.8 (a) Schematic of electrochemical lithiation and exfoliation of 2D MoS_2 from the bulk form.[38] (b) TEM image and (c) AFM image of the exfoliated 2D MoS_2.[38]

Although ion-intercalation exfoliation method can produce massive amount of 2D MoS_2, the ex-exfoliated material may have structural and electronic properties different from the bulk form.[37] For instant, the Mo atom coordination will change from trigonal prismatic (2H-MoS_2) to octahedral (1T-MoS_2), which requires annealing for structural restoration.[20,43-45] Alternatively, bulk MoS_2 can be directly exfoliated by ultrasonication in appropriate liquids including organic solvents, aqueous

surfactants or solution of polymers in solvent.[32,33,46,47] The condition is that the surface energy of the solvents should match with that of the MoS_2 in order to minimize the enthalpy of exfoliation.[11,17] The surface energy of MoS_2 is about 70 mJ m^{-2}, and solvents like N-methyl-pyrrolidone is able to effectively exfoliate the MoS_2.[17,32]

1.3.2.3 Laser and Plasma Thinning

To obtain high quality 2D MoS_2 with controllable size and shape, high energy induced thinning of MoS_2 nanosheets has been performed by focused laser beam[48] and Ar^+ plasma irradiation[49]. In the laser thinning process, mechanical exfoliated multilayer MoS_2 flakes can be thinned down to single layer by moving a focused laser beam over the flakes with high power. The thinning process is based on the sublimation of the upper layers due to laser induced heating. Because of the poor interlayer van der Waals interaction of MoS_2 and relatively difficult heat dissipation through the substrate, upper layers can be removed easily.[48] However, the bottom layer is in close contact with the substrate which acts as a heat sink, heat can be dissipated easily and the bottom layer can be retained on the substrate until higher laser powder is applied.[48] Laser scan rate as fast as 8 μm^2 min^{-1} can be performed and patterned feature size of 200 nm can be generated. Figure 1.9 (a) shows a multilayer MoS_2 flake deposited on a SiO_2/Si substrate and the marked region is the laser

scanning area. After laser scanning, there is a significant color change of scanning area as shown in figure 1.9 (b). AFM measurement in figure 1.9 (c) indicates that the laser-thinned MoS_2 has a thickness of about 0.9 nm, approximate to the single layer thickness (~0.62 nm). Figure 1.9 (d) shows the Raman spectra of the laser-thinned single layer MoS_2 and pristine MoS_2 flakes with thickness ranging from 1-53 layers. It is obvious that after laser thinning, the frequency difference between the E^1_{2g} and A_{1g} Raman modes of the laser-thinned single layer MoS_2 decreases significantly to 21 cm^{-1}, approximate to that of the pristine single layer MoS_2 (19 cm^{-1}). Raman mapping of the frequency difference between the two Raman modes (figure 1.9 (e)) shows that uniform thickness of the laser-thinned single layer MoS_2. PL spectra in figure 1.9 (f) reveals comparable PL peak positions and intensity of the pristine and laser-thinned single layer MoS_2.

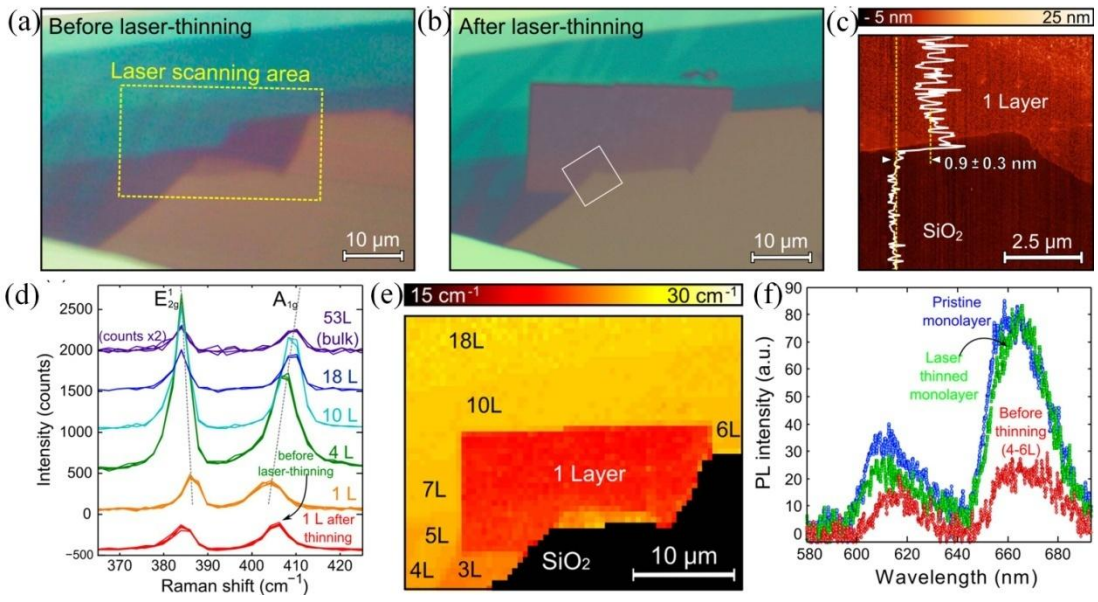

Figure 1.9 OM image of a multilayer MoS_2 flake deposited on a 285 nm SiO_2/Si

substrate (a) before and (b) after laser thinning in the region as marked by the dashed rectangle in (a). (c) Topographic AFM image of the region marked by the square in (b). (d) Raman spectra of the laser-thinned single layer MoS_2 and pristine MoS_2 flakes with thickness ranging from 1 layer to 53 layers. (e) Spatial Raman mapping of the frequency difference between the E^1_{2g} and A_{1g} Raman modes measured in the laser-thinned region in (b). (f) PL of the pristine single layer MoS_2 and the 4-6 layer MoS_2 flakes before and after laser thinning.[48]

Plasma thinning is similar to the laser thinning method but using Ar^+ plasma instead of laser beam to remove upper layers. Both methods allows to obtain high quality 2D MoS_2 with controllable size and shape. However, they are difficult to scale up.[11]

1.3.2 Bottom-up Approach

The development of synthesis methods for large-area and uniform 2D MoS_2 is important to applications such as wafer-scale fabrication of electronic devices and transparent and flexible optoelectronics.[11] Previous success chemical vapor deposition (CVD) of graphene on metal substrates such as Cu,[50] has been a major breakthrough for large-scale fabrication of 2D devices. Recently, considerable CVD research has been focused on the synthesis of large-area 2D TMDs, especially for 2D MoS_2.[51-58] This section highlights the recent development of large-area synthesis of

2D MoS_2, and the synthesis methods can be generally classified into two categories: (1) Direct sulfurization of Mo containing thin film;[51-54] (2) CVD through vaporizing Mo and S sources,[55-57] or direct vaporization of MoS_2 source.[58]

1.3.2.1 Sulfurization

The first synthesis of atomically thick MoS_2 layer was reported by Zhan *et al.* in 2012.[51] The synthesis process includes the pre-deposition of molybdenum (Mo) thin film on a SiO_2/Si substrate and subsequent sulfurization of the Mo film at temperature of 750 ^oC in vacuum system, as schematically illustrated in figure 1.10 (a). The thickness of the as-synthesized MoS_2 layer is determined by that of the pre-deposited Mo thin film.[51] This method can easily obtain wafer-scale atomically thick MoS_2 layer, but it was reported that the as-synthesized MoS_2 film is polycrystalline with grain size ranging from 10-30 nm.[51] Similar method was also demonstrated by Lin *et al.* where they pre-deposited molybdenum trioxide (MoO_3) instead of Mo thin film.[52] Figure 1.10 (b) and (c) respectively shows the OM image and TEM image of the as-synthesized MoS_2 with large area. Figure 1.10 (d) and (e) are the high resolution TEM (HRTEM) images captured at the edges of the MoS_2 film, indicating the as-synthesized MoS_2 film possesses a stack layered structure with 2-3 layers.

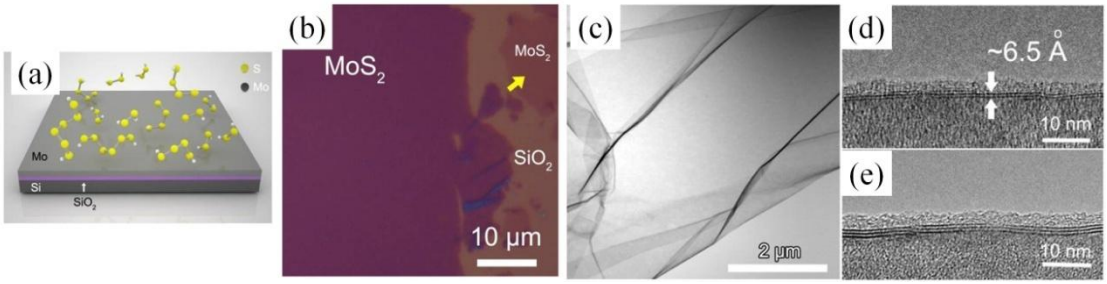

Figure 1.10 (a) Schematic of sulfurization of Mo thin film. (b) OM image and (c) TEM image of MoS_2 atomic layer. (d) and (e) HRTEM images of the as-synthesized MoS_2 atomic layer.[51]

Alternatively, a two-step thermolysis process was introduced to deposit MoS_2 film with 3 layers by dip-coating in ammonium thiomolybdates ($(NH_4)_2MoS_4$) and converting to MoS_2 by annealing at 500 ^oC followed by sulfurization at 1000 ^oC,[53] as schematically illustrated in figure 1.11. The first annealing leads to the formation of MoS_2 through the chemical reaction $(NH_4)_2MoS_4 + H_2 \rightarrow 2NH_3 + 2H_2S + MoS_2$.[53] The second annealing at higher temperature aims to improve the crystallinity of the MoS_2.[53] This method is able to synthesize large-area and highly crystalline MoS_2 atomic layers.

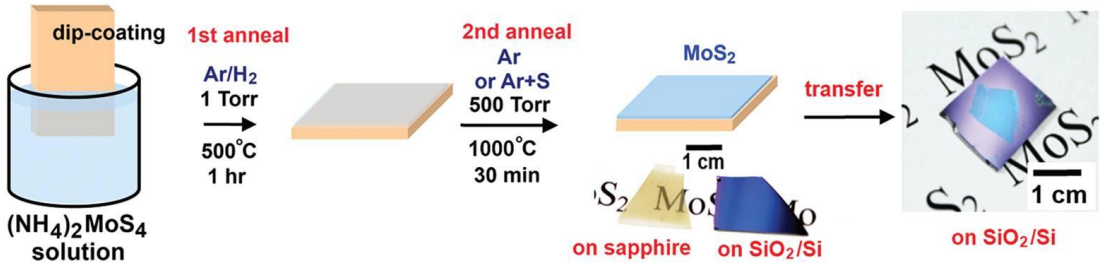

Figure 1.11 Schematic of 2D MoS_2 synthesis via thermal decomposition and sulfurization of $(NH_4)_2MoS_4$.[53]

Another way to obtain highly crystalline MoS_2 with large grain size is to grow MoO_2 crystals followed by sulfurization, as reported by Wang *et al.*[54] During the synthesis, MoO_3 was reduced by vaporized S at 650-850 ^oC, resulting in MoO_2 microplates nucleated on the receiving substrate.[54] By further annealing the MoO_2 microplates in S vapor at elevated temperature of 850-950 ^oC, the surface of the MoO_2 microplates were sulfurized to MoS_2 with various number of layer depending on the reaction time.[54] The MoS_2 layer can then be separated and transferred to other substrates by polymer-based transfer techniques. Figure 1.12 (a) shows the synthesis strategy of the MoS_2 flakes with thickness depending on the reaction time. Figure 1.12 (b) and (c) respectively shows the OM images of the as-synthesized MoS_2/MoO_2 microplates and the MoS_2 flakes after separation from the underlying MoO_2. The as-synthesized MoS_2 flakes have grain size equivalent to their original size, which is larger than 10 μm. The Raman spectra shown in figure 1.12 (d) evidences high purity of MoS_2 can be obtain after separation from the microplates. This method offers a way to obtain highly crystalline and large grain-sized 2D MoS_2, however, it remains challenge to obtain large-area MoS_2 film unless the prior formation of a large-area continuous MoO_2 template.

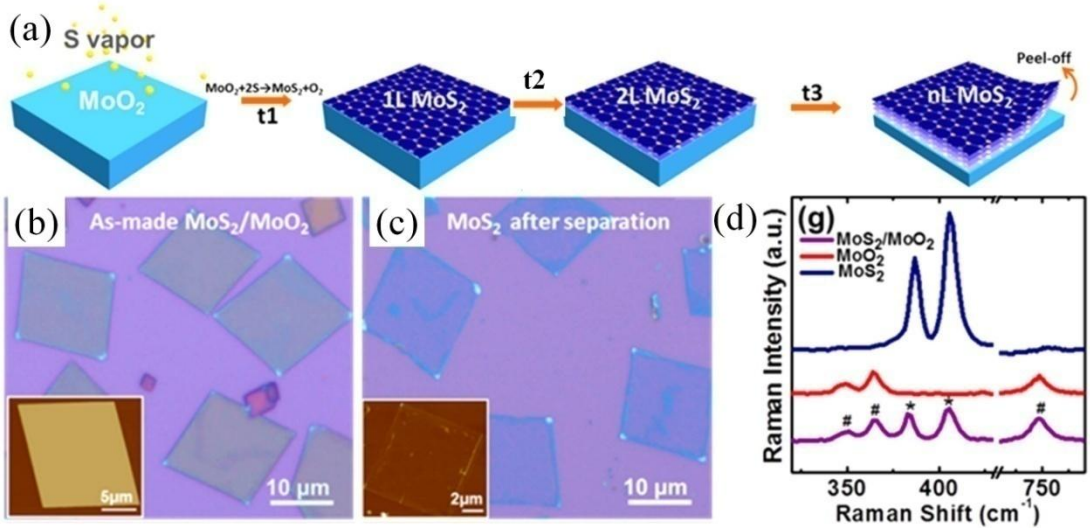

Figure 1.12 (a) Strategy of synthesizing highly crystalline large grain-sized MoS_2 flakes with thickness depending on sulfurization time. OM images of (b) as-synthesized MoS_2/MoO_2 microplates, and (c) MoS_2 after separation. (d) Raman spectra of MoS_2, MoO_2 and MoS_2/MoO_2.[54]

1.3.2.2 Chemical Vapor Deposition

The CVD method is based on the simultaneous vaporization of chemical sources, reaction and deposition on particular substrates. The CVD growth of 2D MoS_2 was first reported by Lee *et al.* and they concluded that substrate treatment with aromatic molecules such as reduced graphene oxide (rGO), perylene-3,4,9,10-tetracarboxylic acid tetrapotassium salt (PTAS) and perylene-3,4,9,10-tetracarboxylic dianhydride (PTCDA) is a critical step to promote the growth of 2D MoS_2.[55,56] In a typical synthesis process, the substrate was pretreated with aromatic molecules as seeds prior growth. The substrate was then faced down and placed above the MoO_3 source. 2D

MoS_2 was synthesized via gas-phase reaction of MoO_3 and S at 650 ^oC under ambient pressure.[55] Figure 1.13 (a) schematically illustrates the CVD growth process of 2D MoS_2. The reaction mechanism is supposed to be the reduction of MoO_3 to volatile suboxide MoO_{3-x} by S vapor at high temperature, and the subsequent reaction of the suboxide with S vapor to form MoS_2 on the substrate.[55] Figure 1.13 (b) and (c) respectively shows the OM image and SEM image of the as-synthesized 2D MoS_2. Each individual MoS_2 has a triangular shape with dimensions over 30 μm. Adjacent MoS_2 crystals can merge together and form a continuous film, but it is still a challenge to control over the thickness and uniformity of the MoS_2 film. It was reported that by pre-treating the substrate with PTAS, MoS_2 can be synthesized on diverse surfaces, even on rough surface as shown in figure 1.13 (c).[56] The PL mapping over an individual MoS_2 crystallite at 670 nm as shown in figure 1.13 (d) reveals optically active of the MoS_2 with uniform PL signal.

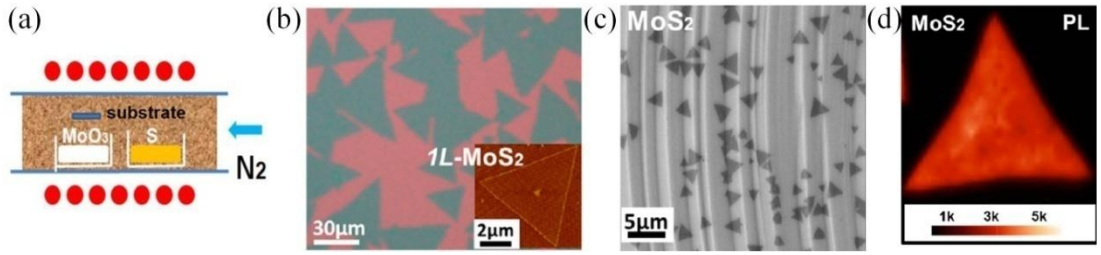

Figure 1.13 (a) Schematic of CVD growth of 2D MoS_2. (b) OM image (inset: AFM image) and (c) SEM image of the as-synthesized 2D MoS_2. (d) PL mapping of an individual single layer MoS_2 crystallite at 670 nm.[55,56]

The above mentioned CVD method relies on aromatic molecules as seeding materials. Alternatively, Najmaei *et al.* reported the CVD synthesis of 2D MoS_2 without the assist of aromatic molecules, but using a patterned substrate instead.[57] During the CVD growth of 2D MoS_2, they found that edges of the substrate and any surface roughness like scratches can act as nucleation sites for 2D MoS_2 growth.[57] In order to grow large-area continuous 2D MoS_2 films, they increased the density of the nucleation site through patterning the substrate,[57] as shown in figure 1.14 (e). Figure 1.14 (a) to (d) are the SEM images showing the growth process of MoS_2 from small triangles to continuous films through the coalescence of adjacent MoS_2 triangles. Figure 1.14 (e) shows the OM image of a continuous MoS_2 film synthesized on the square-patterned substrate. The Raman spectra at three different points as marked in figure 1.14 (f) are shown in figure 1.14 (g). By measuring the frequency difference of the two Raman modes, it reveals that single and bilayer MoS_2 films were formed between the patterns while multilayer MoS_2 films can be identified on the patterns. Large-area continuous 2D MoS_2 film can be synthesized by this pattern-assisted method, and the transfer of the large-area MoS_2 film is shown in figure 1.14 (h). The grain size of the film is determined by the size of the MoS_2 triangle.

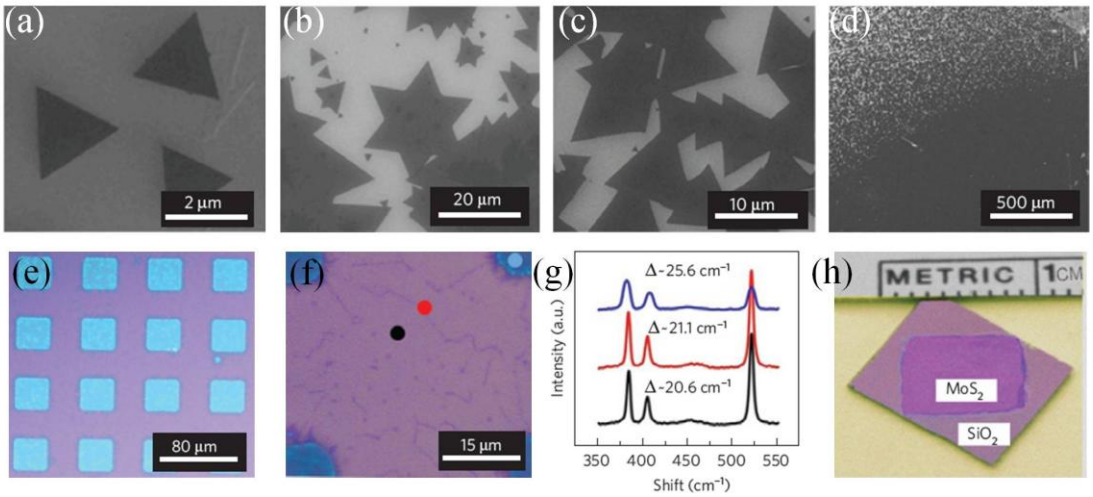

Figure 1.14 (a)-(d) SEM images showing the growth process of MoS_2 from small triangles to continuous films. (e) OM image showing a continuous large-area MoS_2 film synthesized on a patterned substrate. (f) Magnified OM image showing continuous film between patterns. (g) Raman spectra of MoS_2 at different positions marked in (f). (h) Large-area MoS_2 film transferred to a new substrate from the patterned substrate.[57]

A comparably easy way to obtain 2D MoS_2 is by direct vaporizing the MoS_2 source at high temperature.[58] The vaporized MoS_2 gas will be transferred and condense on the receiving substrate placed at a lower temperature zone, forming 2D MoS_2 triangular flakes. Figure 1.15 (a) shows the schematic of the synthesis process. Figure 1.15 (b) shows the SEM image of the as-synthesized 2D MoS_2 triangular flakes. This method is relatively easy but large-area 2D MoS_2 film is challenge to be formed. Possible way to achieve large-area film may require the increase of nucleation sites through substrate treatments as mention above.

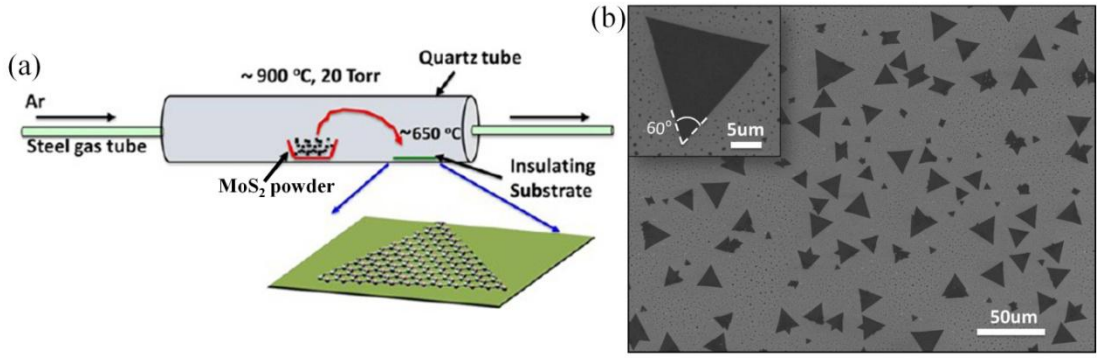

Figure 1.15 (a) Schematic of vapor-solid growth of MoS_2. (b) SEM image of as-synthesized 2D MoS_2 flakes.[58]

1.4 Applications of 2D MoS_2

1.4.1 Electronic Devices

The unique properties of 2D MoS_2 having a direct bandgap of 1.9 eV allow it to be 2D semiconductors for transistors in digital electronics. Early back-gate FETs based on MoS_2 nanosheets with SiO_2 as dielectric showed carrier mobility less than 10 $cm^2\ V^{-1}\ s^{-1}$.[59] To improve the FET performance, Radisavljevic *et al.* fabricated a top-gate FET based on single-layer MoS_2 as the channel and hafnium(IV) oxide (HfO_2) as the dielectric material. The HfO_2 with a dielectric constant of 25 and a bandgap of 5.7 eV significantly increased the room-temperature carrier mobility of MoS_2 to over 200 $cm^2\ V^{-1}\ s^{-1}$,[5] which is comparable to that of Si.[60] The MoS_2-based FET showed an excellent on/off current ratio of 10^8, along with an ultralow standby power dissipation.[5] In addition, the abrupt switching behavior and immunity to short channel effects allow it to be promising 2D FET device.[61] The current-voltage curves

for the top-gated MoS_2-base FET are shown in figure 1.16.

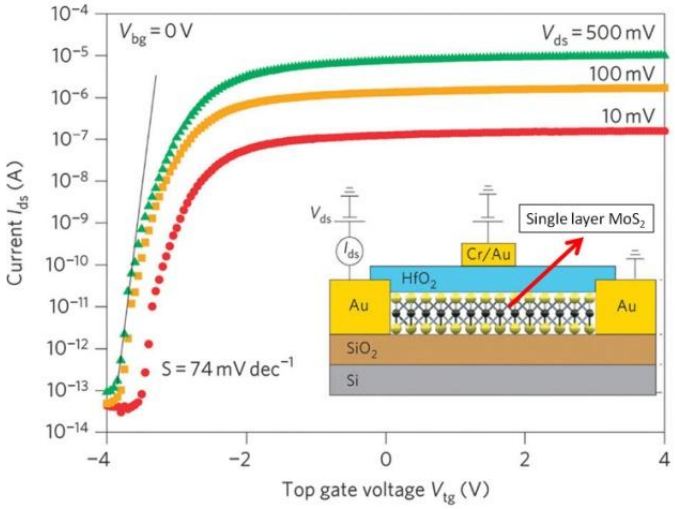

Figure 1.16 Source-drain current versus top-gate voltage curve recorded for a bias voltage ranging from 10 mV to 500 mV. Inset showing the schematic of the top-gated MoS_2-based FET.[5]

The integration of individual transistors into a logic circuit is an important step towards electronic application. A simple integrated circuit composed of two transistors fabricated on a single MoS_2 flake has been demonstrated, which can be used to amplify signals and process basic logic operations.[62] The integration of MoS transistors into complex circuits was further demonstrated by Wang *et al.* where they integrated up to 12 transistors side-by-side based on a single bilayer MoS_2 nanosheet, which is able to perform multiple functions including inverter, logical NAND gate, static random access memory and five-stage ring oscillator.[63] This work shows that 2D MoS_2 is promising building block for future integrated circuits and practical electronic devices.

1.4.2 Optoelectronic Devices

The excellent mechanical properties and intrinsic direct bandgap in the visible region make 2D MoS_2 to be prospective component for flexible optoelectronic devices. Figure 1.17 (a) shows a bottom-gated single-layer MoS_2 based FET fabricated by Yin *et al*., which was used as a phototransistor.[13] Figure 1.17 (b) depicts the photoswitching characteristic of the phototransistor of how the photocurrent in response to different incident light power (wavelength of light < 676 nm). The photoswitching rate between on and off state was found to be within 50 ms (figure 1.17 (c)), which is higher than that of single-layer graphene based device. The photoswitching stability is good as shown in figure 1.17 (d). Another work about light detection by MoS_2-based phototransistors was reported by Lee *et al*.[65] In their work, single- double- and triple-layer MoS_2 phototransistors were fabricated. The phototransistors based on single-layer (bandgap of 1.82 eV) and double-layer (bandgap of 1.65 eV) MoS_2 are promising for green light detection, while that based on triple-layer MoS_2 with bandgap of 1.35 eV is suitable for red light detection.[65]

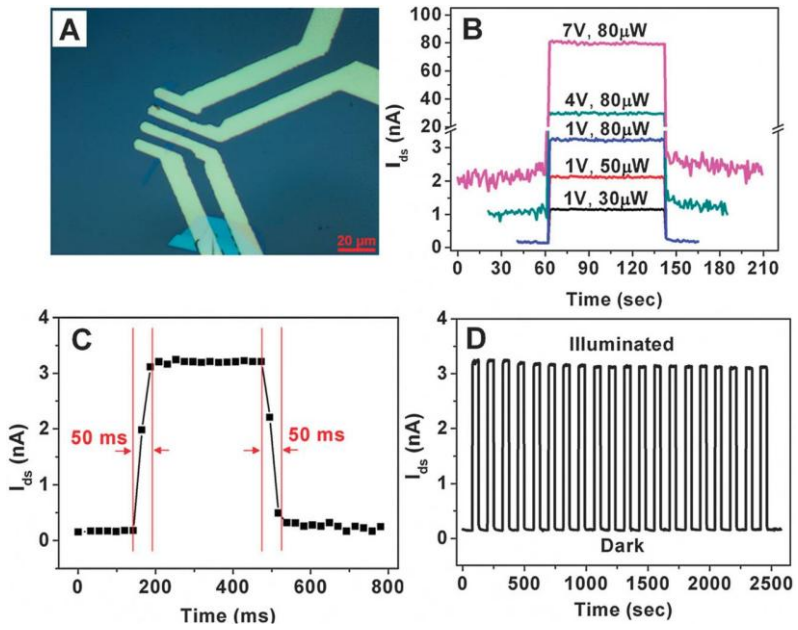

Figure 1.17 (a) OM image of a FET device based on single-layer MoS_2 sheet. (b) Photoswitching behaviors of a single-layer MoS_2 phototransistor at different optical power and drain voltage. (c) Photoswitching rate and (d) stability of photoswtiching behavior of the MoS_2 phototransistor at 1V drain voltage and 80 μW optical power.[64]

Organic light emitting diodes (OLEDs) are currently one of the most promising optoelectronic devices for future lighting panels and displays. Thin film of chemically exfoliated MoS_2 sheets has been demonstrated to be the anode for OLED by Frey *et al*.[66] In their work, the MoS_2 film was plasma treated by oxygen to generate a thin MoO_3 layer on the MoS_2 surface, where the MoS_2 with a large working function acted as hole injector and the wide-gap MoO_3 layer acted as an electron-blocking layer.[66] The resulting combination of the hole-injection and electron-extraction layers improved the carrier balance leading to significant enhancement on light emitting performance and efficiency.[66]

1.4.3 Sensors

FET-based sensors are able to detect molecules by monitoring the conductance changes of the FET channel upon adsorption of target molecules.[17] Recently, Li *et at*. has demonstrated the detection of NO gas by FET-sensors based on mechanically exfoliated single- and multi-layer MoS_2.[31] Since exfoliated MoS_2 is n-type in nature, and NO gas is a type of electron-withdrawing molecules, the exposure of MoS_2 channel to NO gas will cause p-doping of the channel, resulting in an abrupt increase of resistance and decrease of current.[31] The sensors exhibited high sensitivity with detection limit down to 0.8 ppm. Alternatively, they also demonstrated NO gas detection by thin film transistors (TFTs) based on exfoliated MoS_2 obtained by electrochemical lithiation and exfoliation method.[31,38,40,] Unlike mechanical exfoliated MoS_2 nanosheets, MoS_2 nanosheets obtained by chemical exfoliated method have a p-type semiconducting property. As a result, when the TFTs are exposed to NO gas, an increase of channel current will be observed, with detection limit of 190 ppt.[31]

1.5 Energy Related Applications of MoS_2 Nanomaterials

1.5.1 Lithium-ion Batteries

Lithium-ion battery (LIB) has been regarded as one of the most promising energy storage system and has attracted tremendous researches on developing

nanomaterials for high capacity electrodes. Currently, the commercially used LIB anode materials are mainly based on graphitic materials, which have a low specific capacity of 372 mA h g^{-1}. As a material analogous to graphite, MoS_2 has a stack layered structure which allows Li ions to intercalate, with a higher theoretical specific capacity of 670 mA h g^{-1}. While bulk MoS_2 shows poor electrochemical performance as LIB anode material, nanostructured MoS_2 has been reported to have significant improvement on the LIB performance in terms of cycle stability, Coulombic efficiency and rate capability.[67-71] When mixing nanostructured MoS_2 with graphene to form a composite electrode, reversible specific capacity as high as 1290 mA h g^{-1} can be achieved.[72] The higher specific capacity and good electrochemical performance of nanostructured MoS_2 make it promising to replace conventional graphite as future LIB anode material.

High rate LIBs are desired nowadays for fast charging up of electronic devices or electric vehicles. For MoS_2, it was found that by expanding the interlayer distance and disordering the layer orientations through nanostructure engineering, its rate capability can be greatly enhanced.[67] Figure 1.18 (a) schematically shows a way to achieve MoS_2 nanoplates with disordered layers and expanded interlayer distance. HRTEM image and fast Fourier transformed image shown in figure 1.18 (c) confirm that the interlayer distance of the MoS_2 nanoplates is 0.69 nm, larger than that of the

pristine one (0.62 nm). Figure 1.18 (d) shows that rate capability as high as 50 C can be achieved by the MoS_2, with high reversible capacity of 700 mA h g^{-1} and about 550 mA h g^{-1} retention after 20 cycles. The enhanced rate capability is ascribed to the disordered layers and expanded interlayer distance which provide additional and fast diffusion channels for Li ions.[67]

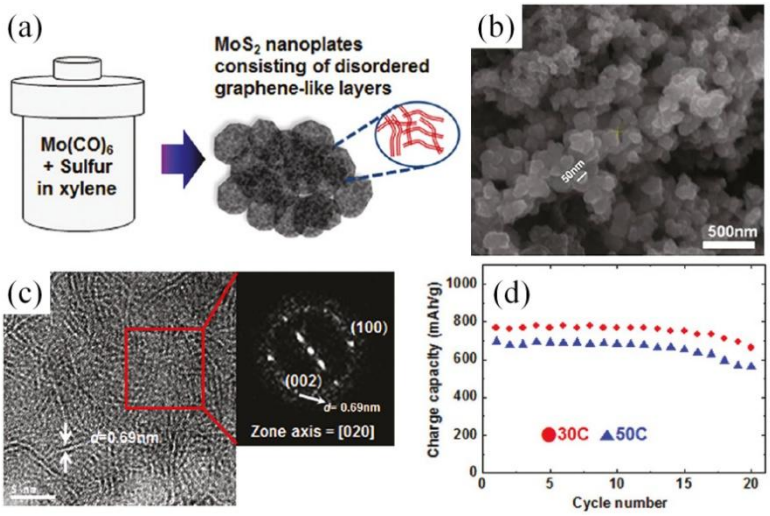

Figure 1.18 (a) Schematic of synthesis MoS_2 nanoplates. (b) SEM image of as-synthesized MoS_2 nanoplates. (c) HRTEM image of the MoS_2 nanoplates with digitalized fast Fourier transformed image. (d) Plot of cycling performances of the MoS_2 nanoplates under current densities of 30 C and 50 C.[67]

1.5.2 Hydrogen Evolution Reaction

As a clean fuel, hydrogen has been considered as one of the most promising alternative for fossil fuels in the future.[73] The electrocatalytic hydrogen evolution reaction (HER) is considered as one of the most important method for efficient

hydrogen production.[74] Currently, the most effective electrocatalysts are based on noble metals especially platinum.[75] However, the high price and rareness of noble metals resist them for practical use. Alternatively, MoS_2 has been recently studied and confirmed as an active electrocatalyst for HER by exposing the edge sites which is electrochemically active in contrast to the inactive basal plane.[76-78] On this basis, good HER can be achieved through optimizing the edge sites of MoS_2 nanomaterials. For instant, Xie *et al*. synthesized defect-rich MoS_2 nanosheets for HER through hydrothermal reaction of Mo-containing source with excess amount of S-containing source.[77] Figure 1.19 (a) and (b) respectively show the SEM image and HRTEM image of the defect-rich MoS_2. The HRTEM image shows that the defects causing discontinuous of the nanosheets, which in turn generating electroactive edge sites for HER.[77] The polarization curves of HER in figure 1.19 (c) reveal superior HER performance of the defect-rich MoS_2 nanosheets due to more dense of the electroactive edge sites induced by the defects.

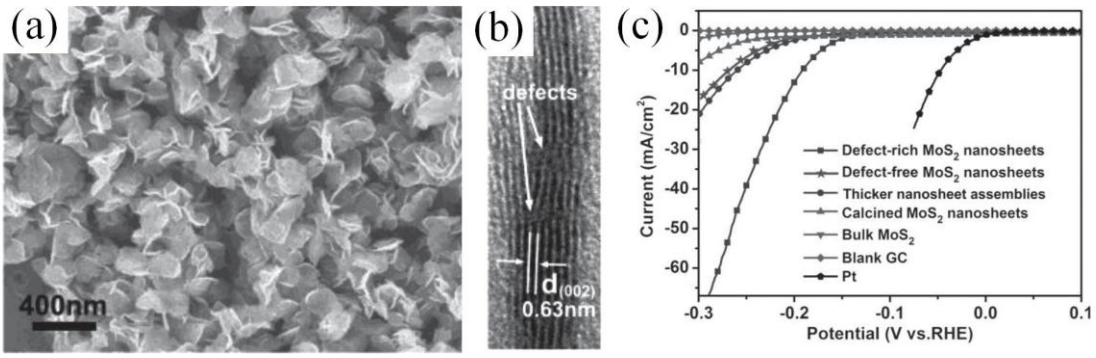

Figure 1.19 (a) SEM image and (b) HRTEM image of defect-rich MoS_2 nanosheets. (c)

HER polarization curves of various materials.[77]

Apart from defect engineering, the density of MoS_2 active edge sites can be increased by enlarging the interlayer distance of MoS_2.[78] Figure 1.20 (a) shows the HRTEM image of MoS_2 layers with edge sites exposed on the surface. In order to optimizing the density of edge sites, the MoS_2 layers were intercalated by Li ions to increase the interlayer distance. Figure 1.20 (b) shows the Galvanostatic discharge curve of the MoS_2 lithiation process, and the relationship of lithiation dregree and interlayer distance is shown in figure 1.20 (c) which reveals larger interlayer distance can be achieved by increasing the degree of lithiation. Figure 1.20 (d) shows the HER polarization curves of MoS_2 at different degree of lithiation and manifest MoS_2 with higher degree of lithiation (1.1 V), or larger interlayer distance, can obtain the best HER result.[78]

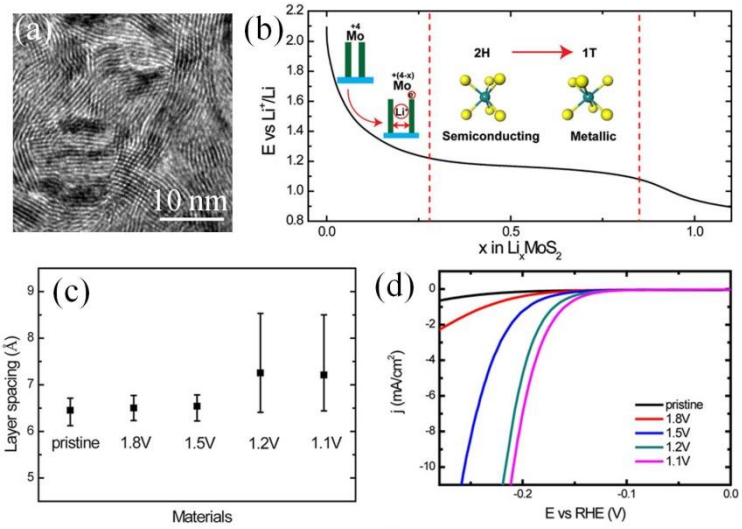

Figure 1.20 (a) HRTEM image of vertical MoS_2 layers. (b) Galvanostatic discharge

curve of the lithiation process. (c) Relationship of lithiation degree and interlayer distance of MoS_2. (d) HER polarization curves of MoS_2 at different lithiation degree.[78]

1.6 Objectives and Outlines

MoS_2 has attracted considerable research attention in recent years due to the emerging properties of its 2D form. Nanostructured MoS_2 also shows promising in multidiscipline applications especially in energy related fields such as lithium-ion battery (LIB) and hydrogen evolution reaction (HER). The objectives of this thesis are:

(1) to synthesize large-area and uniform 2D MoS_2 atomic layer by sulfurization and CVD method, and explore its growth behavior;

(2) to employ simple hydrothermal reaction to prepare MoS_2 nanostructures for LIB and HER applications.

Chapter 2 introduces the preparation of 2D MoS_2 atomic layer by direct sulfurization of MoO_3 thin film and discusses the thickness-dependent of Raman spectroscopy and photoluminescence of the MoS_2 atomic layer. Chapter 3 describes the CVD synthesis of MoS_2 at different pressures and investigates the growth mechanism of 2D MoS_2. Chapter 4 presents the synthesis of MoS_2 nanosphere network and demonstrates its application for LIB and HER. In the research of nanomaterials for LIB, it is worth to mention Si for its highest theoretical specific

capacity for LIB application. Chapter 5 introduces a novel design of 3D porous Cu supported Si nanostructure as LIB anode and discusses how empty space engineering benefit Si for LIB application. Finally, the thesis will be concluded in Chapter 6 with a brief summary and prospective future works.

1.7 References

[1] S. Das, M. Kim, J. Lee, W. Choi. *Critical Reviews in Solid State and Materials Sciences*, **2014**, 39, 231-252.

[2] K. S. Novoselov, D. Jiang, F. Schedin, T. J. Booth, V. V. Khotkevich, S. V. Morozov, A. K. Geim. *Proc. Natl Acad. Sci. USA*, **2005**, 102, 10451-10453.

[3] K. S. Novoselov, A. K. Geim, S. V. Morozov, D. Jiang, Y. Zhang, S. V. Dubonos, I. V. Grigorieva, A. A. Firsov. *Science*, **2004**, 206, 666-669.

[4] X. Huang, Z. Yin, S. Wu, X. Qi, Q. He, Q. Zhang, Q. Yan, F. Boey, H. Zhang, *Small*, **2011**, 7, 1876-1902.

[5] B. Radisavljevic, A. Radenovic, J. Brivio, V. Giacometti, A. Kis. *Nature Nanotechnology*, **2011**, 6, 147-150.

[6] M-W. Lin, C. Ling, Y. Zhang, H. J. Yoon, M. M. Cheng, L. A. Agapito, N. Kioussis, N. Widjaja, Z. Zhou. *Nanotechnology*, **2011**, 22, 265201.

[7] X. Li, X. Wang, L. Zhang, S. Lee, H. Dai. *Science*, **2008**, 319, 1229-1232.

[8] M. Y. Han, B. Ozyilmaz, Y. Zhang, P. Kim. *Phys. Rev. Lett.*, **2007**, 98, 206805.

[9] R. Balog *et al*. *Nature Mater.*, **2010,** 9, 315-319.

[10] Y. Zhang *et al*. *Nature*, **2009**, 459, 820-823.

[11] Q. H. Zhang, K. Kalantar-Zadeh, A. Kis, J. N. Coleman, M. S. Strano. *Nature Nanotechnology*, **2012**, 7, 699-712.

[12] M. Chhowalla, H. S. Shin, G. Eda, L-J. Li, K. P. Loh, H. Zhang. *Nature Chemistry*, **2013**, 5, 263-275.

[13] K. F. Mak, C. Lee, J. Hone, J. Shan, T. F. Heinz. *Physical Review Letters*, **2010**, 205, 136805.

[14] J. A. Wilson, A. D. Yoffe. *Adv. Phys.*, **1969**, 18, 193-335.

[15] B. Radisavljevic, A. Radenovic, J. Brivio, V. Giacometti, A. Kis. *Nat. Nanotechnol.*, **2011**, 6, 147-150.

[16] http://www.itrs.net/Links/2013ITRS/Home2013.htm

[17] X. Huang, Z. Zeng, H. Zhang. *Chem. Soc. Rev.*, **2013**, 42, 1934-1946.

[18] A. R. Beal, J. C. Knights, W. Y. Liang. *J. Phys. C: Solid State Phys.*, **1972**, 5, 3540.

[19] A. N. Enyashin, L. Yadgarov, L. Houben, I. Popov, M. Weidenbach, R. Tenne, M. Bar-Sadan, G. Seifert. *J. Phys. Chem. C*, **2011**, 115, 24586-24591.

[20] S. J. Sandoval, D. Yang, R. F. Frindt, J. C. Irwin. *Phys. Rev. B: Condens. Matter Mater. Phys.*, **1991**, 44, 3955-3962.

[21] G. Eda, H. Yamaguchi, D. Voiry, T. Fujita, M. W. Chen, M. Chhowalla. *Nano Lett.*, **2011**, 11, 5111-5116.

[22] A. Castellanos-Gomez, M. Poot, G. A. Steele, H. S. J. van der Zant, N. Agrait, G. Rubio-Bollinger, *Adv. Mater.*, **2012**, 24, 772-775.

[23] S. Bertolazzi, J. Brivio, A. Kis. *ACS Nano*, **2011**, 5, 9703-9709.

[24] A. Splendiani, L. Sun, Y. B. Zhang, T. S. Li, J. Kim, C. Y. Chim, G. Galli, F. Wang. *Nano Lett.*, **2010**, 10, 1271-1275.

[25] R. Coehoorn, C. Haas, J. Dijkstra, C. J. F. Flipse, R. A. de Groot, A. Wold. *Phys. Rev. B*, **1987**, 35, 6195-6202.

[26] R. Coehoorn, C. Haas, R. A. de Groot. *Phys. Rev. B*, **1987**, 35, 6195-6206.

[27] P. A. Bertrand. *Phys. Rev. B*, **1991**, 44, 5745-5749.

[28] A. G. Bagnall, W. Y. Liang, E. A. Marseglia, B. Welber. *Physica*, **1980**, 99B, 343-346.

[29] C. Lee, H. Yan, L. E. Brus, T. F. Heinz, J. Hone, S. Ryu. *ACS Nano*, **2011**, 5, 7707-7712.

[30] H. Li, Q. Zhang, C. C. R. Yap, B. K. Tay, T. H. T. Edwin, A. Olivier, D. Baillargeat. *Adv. Funct. Mater.*, **2012**, 22, 1385-1390.

[31] H. Li, Z. Y. Yin, Q. Y. He, X. Huang, G. Lu, D. W. H. Fam, A. I. Y. Tok, Q. Zhang, H. Zhang. *Small*, **2012**, 8, 63-67.

[32] J. N. Coleman *et al*. *Science,* **2011**, 331, 568-571.

[33] R. J. Smith *et al*. *Adv. Mater.*, **2011**, 23, 3944-3948.

[34] R. Bissessur, J. Heising, W. Hirpo. *Chem. Mater.*, **1996**, 8, 318-320.

[35] P. Joensen, R. F. Frindt, S. R. Morrison. *Mater. Res. Bull.*, **1986**, 21, 457-461.

[36] M. Osada, T. Sasaki. *J. Mater. Chem.*, **2009**, 19, 2503-2511.

[37] G. Eda *et al*. *Nano Lett.*, **2011**, 11, 5111-5116.

[38] Z. Zeng *et al*. *Angew. Chem. Int. Ed.*, **2011**, 50, 11093-11097.

[39] M. B. Dines. *Mater. Res. Bull.*, **1975**, 10, 287-291.

[40] Z. Zheng, T. Sun, J. Zhu, X. Huang, Z. Yin, G. Lu, Z. Fan, Q. Yan, H. H. Hng, H. Zhang. *Angew. Chem. Int. Ed.*, **2012**, 51, 9052-9056.

[41] H. Matte, A. Gomathi, A. K. Manna, D. J. Late, R. Datta, S. K. Pati, C. N. R. Rao. *Angew. Chem. Int. Ed.*, **2010**, 49, 4059-4062.

[42] B. K. Miremadi, S. R. Morrison. *J. Catal.*, **1991**, 131, 127-132.

[43] G. L. Frey, K. J. Reynolds, R. H. Friend, H. Cohen, Y. Feldman. *J. Am. Chem. Soc.*, **2003**, 125, 5998-6007.

[44] R. Bissessur, M. G. Kanatzidis, J. L. Schindler, C. R. Kannewurf. *J. Chem. Soc. Chem. Commun*., **1993**, 1582-1585.

[45] R. A. Gordon, D. Yang, E. D. Crozier, D. T. Jiang, R. F. Frindt, *Phy. Rev. B*, **2002**, 65, 125407.

[46] K-G. Zhou, N-N. Mao, H-X. Wang, Y. Peng, H-L. Zhang. *Angew. Chem. Int. Ed.*, **2011**, 50, 10839-10842.

[47] P. May, U. Khan, J. M. Hughes, J. N. Coleman. *J. Phys. Chem. C*, **2012**, 116, 11393-11400.

[48] A. Castellanos-Gomez, M. Barkelid, A. M. Goossens, V. E. Calado, H. S. J. van der Zant, G. A. Steele, *Nano Lett.*, **2012**, 12, 3187-3192.

[49] Y. Liu, H. Nan, X. Wu, W. Pan, W. Wang, J. Bai, W. Zhao, L. Sun, X. Wang, Z. Ni. *ACS Nano*, **2013**, 5, 4202-4209.

[50] X. Li *et al*. *Science*, **2009**, 324, 1312-1314.

[51] Y. Zhan, Z. Liu, S. Najmaei, P. M. Ajayan, J. Lou. *Small*, **2012**, 8, 996-971.

[52] Y-C. Lin, W. Zhang, J-K. Huang, K-K. Liu, Y-H. Lee, C-T. Liang, C-W. Chu, L-J. Li. *Nanoscale*, **2012**, 4, 6637-6641.

[53] K-K. Liu, W. Zhang, Y-H. Lee, Y-C. Lin, M-T. Chang, C-Y. Su, C-S. Chang, H. Li, Y. Shi, H. Zhang, C-S. Lai, L-J. Li. *Nano Lett.*, **2012**, 12, 1538-1544.

[54] X. Wang, H. Feng, Y. Wu, L. Jiao. *JACS*, **2013**, 135, 5304-5307.

[55] Y-H. Lee, X-Q. Zhang, W. Zhang, M-T. Chang, C-T. Lin, K-D. Chang, Y-C. Yu, J. T-W. Wang, C-S. Chang, L-J. Li. *Adv. Mater.*, **2012**, 24, 2320-2325.

[56] Y-H. Lee, L. Yu, H. Wang, W. Fang, X. Ling, Y. Shi, C-T. Lin, J-K. Huang, M-T. Chang, C-S. Chang, M. Dresselhaus, T. Palacios, L-J. Li, J. Kong. *Nano Lett.*, **2013**,

13, 1852-1857.

[57] S. Najmaei, Z. Liu, W. Zhou, X. Zou, G. Shi, S. Lei, B. I. Yakobson, J-C. Idrobo, P. M. Ajayan, J. Lou. *Nature Mater.*, **2013**, 12, 754-759.

[58] S. Wu, C. Huang, G. Aivazian, J. S. Ross, D. H. Cobden, X. Xu. *ACS Nano*, **2013**, 7, 2768-2772.

[59] K. S. Novoselov, D. Jiang, F. Schedin, T. J. Booth, V. V. Khotkevich, S. V. Morozov, A. K. Geim. *Proc. Natl. Acd. Sci. USA*, **2005**, 102, 10451-10453.

[60] V. Podzorov, M. E. Gershenson, C. Kloc, R. Zeis, E. Bucher, *Appl. Phys. Lett.*, **2004**, 84, 3301-3303.

[61] Y. Yoon, K. Ganapathi, S. Salahuddin. *Nano Lett.*, **2011**, 11, 3768-3773.

[62] B. Radisavljevic, M. B. Whitwick, A. Kis, *ACS Nano*, **2011**, 5, 9934-9938.

[63] H. Wang, L. Yu, Y-H. Lee, Y. Shi, A. Hsu, M. L. Chin, L-J. Li, M. Dubey, J. Kong, T. Palacios, *Nano Lett.*, **2012**, 12, 4674-4680.

[64] Z. Y. Yin, H. Li, L. Jiang, Y. M. Shi, Y. H. Sun, G. Lu, Q. Zhang, X. D. Chen, H. Zhang. *ACS Nano*, **2012**, 6, 74-80.

[65] H. S. Lee, S-W. Min, Y-G. Chang, M. K. Park, T. Nam, H. Kim, J. H. Kim, S. Ryu, S. Im. *Nano Lett.*, **2012**, 12, 3695-3700.

[66] G. L. Frey, K. J. Reynolds, R. H. Friend, H. Cohen, Y. Feldman. *J. Am. Chem. Soc.*, **2003**, 125, 5998-6007.

[67] H. Hwang, H. Kim, J. Cho. *Nano Lett.*, **2011**, 11, 4826-4830.

[68] S. Liang, J. Zhou, J. Liu, A. Pan, Y. Tang, T. Chen, G. Fang. *CrystEngComm*, **2013**, 15, 4998-5002.

[69] S. Ding, D. Zhang, J. S. Chen, X. W. Lou. *Nanoscale*, **2012**, 4, 95-98.

[70] P-P Wang, H. Sun, Y. Ji, W. Li, X. Wang. *Adv. Mater.*, **2014**, 26, 964-949.

[71] S-K. Park, S-H. Yu, S. Woo, J. Ha, J. Shin, Y-E. Sung, Y. Piao. *CrystEngComm*, **2012**, 14, 8323-8325.

[72] K. Chang, W. Chen, *Chem. Commun.*, **2011**, 47, 4252-4254.

[73] M. S. Dresselhaus, I. L. Thomas, *Nature*, **2011**, 414, 332-337.

[74] J. A. Turner. *Science*, **2004**, 305, 972-974.

[75] J. K. Norskov, C. H. Christensen. *Science*, **2006**, 312, 1322-1323.

[76] T. F. Jaramillo, K. P. Jogensen, J. Bonde, J. H. Nielsen, S. Horch, I. Chorkendorff. *Science*, **2007**, 317, 100-102.

[77] J. Xie, H. Zhang, S. Li, R. Wang, X. Sun, M. Zhou, J. Zhou, X. Lou, Y. Xie. *Adv. Mater.*, **2013**, 25, 5807-5813.

[78] H. Wang, Z. Lu, S. Xu, D. Kong, J. J. Cha, G. Zheng, P-C. Hsu, K. Yan, D. Bradshaw, F. B. Prinz, Y. Cui. *PNAS*, **2013**, 110, 19701-19706.

Chapter 2 Synthesis of Large-area MoS_2 Atomic Layer via Direct MoO_3 Sulfurization

2.1 Introduction

Graphene has attracted intensive research interest in the recent few years due to its unique two-dimensionality and remarkable high carrier mobility.[1] However, pristine graphene lacks a bandgap which restricts its applications in digital logic and optoelectronic devices.[2] Bandgap can be engineered in graphene but will increase fabrication complexity and induce defects that would diminish the carrier mobility.[3-7] Recently, research interest has shifted to the study of graphene-like 2D transition metal dichalcogenides (TMDs) such as MoS_2, $MoSe_2$, WS_2 and WSe_2 which have intrinsic direct bandgaps when the thickness is thinned down to atomic layer.[8,9] Among all the 2D TMDs, particular research effort has been devoted to MoS_2 due to its structural and chemical stability, direct bandgap (~1.9 eV) in the visible region, low cost and abundance in the nature.[9] MoS_2 has a layered structure of which each layer is constituted by a Mo hexagonal layer sandwiched between two S hexagonal layers by strong covalent bonds.[8] The interaction between S-Mo-S units is weak van der Waals force, making it easy for exfoliation like graphene.[1,8]

Currently, MoS_2-based devices are mainly fabricated from exfoliated MoS_2 nanosheets which normally have size of only several micrometers that are only

suitable for fundamental characterizations.[2,10] However, for practical implementation, large-area and uniform atomically thin MoS_2 is desirable. Sulfurization of MoO_3 using CVD has been adopted for 2D-MoS_2 synthesis, however, the resulting structures are normally nanoparticles or nanorods.[11,12] Laser[13] and plasma[14] thinning of bulk MoS_2 have been successfully demonstrated to controllable obtain atomic layered MoS_2 with desired shapes, but they are difficult to scale up. Zhan *et al*. paved a way for the synthesis of large-area MoS_2 atomic layer via the sulfurization of Mo thin film.[10] The as-synthesized MoS_2 is 1-5 lay thick with a polycrystalline microstructure. However, the emerging of PL signal from MoS_2, which is an intuitive indication of a direct bandgap, was not reported.

In this work, we successfully synthesized atomically thin MoS_2 via direct sulfurization of MoO_3 to MoS_2. OM and SEM images show that large-area and continuous 2D MoS_2 layer was synthesized. Both Raman spectroscopy and AFM measurement confirmed that the as-synthesized MoS_2 was bilayer in thickness. HRTEM image revealed hexagonal arrangement of the MoS_2 lattice structure. PL spectrum showed two peaks at 652 nm and 612 nm, indicates direct excitonic transition of the MoS_2 layer. Moreover, both the Raman and PL mappings showed that the as-synthesized MoS_2 layer was optically active over large area.

2.2 Experimental Section

2.2.1 Synthesis of Atomically Thin MoS_2

The synthesis of atomically thin MoS_2 by this method involved two steps: 1. thermal evaporation of MoO_3 thin film in a thermal evaporator; 2. sulfurization of the MoO_3 thin film in a tube furnace vacuum system. Prior to thermal evaporation of MoO_3 thin film, 300 nm SiO_2/Si substrates were cleaned with acetone and ethanol. Thermal evaporation of MoO_3 thin film on the 300 nm SiO_2/Si substrates was conducted when the ultimate pressure reached 10^{-5} Pa. 1 nm and 10 nm MoO_3 thin films were respectively deposited with thermal evaporation rate of 0.2 Å/s. After the thermal evaporation, the MoO_3/SiO_2/Si wafer was transferred and placed at the center of a single-zone tube furnace. The S powder was put at the up-stream of the gas flow where the local temperature was about 120 ^oC (evaporation point of S) with respect to the center temperature of 650 ^oC. The tube furnace was pumped to 2×10^{-2} Torr and then purged with 20 sccm Ar gas. For the sulfurization of MoO_3, the center reaction zone was first heated up to 650 ^oC with a ramping rate of 30 ^oC/min and kept for 15 minutes, and then to 850 ^oC with a rate of 10 ^oC/min for 10 minutes. When the center temperature reached 650 ^oC, the S source started to vaporize and reduce the MoO_3 to MoS_2. Higher temperature of 850 ^oC was applied to improve the crystallinity

of the MoS_2 atomic layer. After the reaction, the vacuum system was allowed to naturally cool down to room temperature. Figure 2.1 shows the schematic illustration of the MoO_3 sulfurization process in a single-zone tube furnace vacuum system.

Figure 2.1 Schematic of MoO_3 sulfurization process in a single-zone tube furnace vacuum system.

2.2.2 Characterization

The morphology and structure of the as-synthesized MoS_2 atomic layer were characterized by an optical microscope (Olympus), a Philips FEG-SEM and a Philips CM200 TEM operated at 200 kV. HRTEM image of the MoS_2 layer was captured by Gatan GIF 200 equipped to the TEM. The thickness of the MoS_2 layer was measured by AFM. The binding energies of Mo and S of the MoS_2 layer were characterized by XPS. Raman and PL spectra of the MoS_2 layers were collected by a Renishaw Raman microscope in ambient air with a 514 nm excitation laser.

2.3 Results and Discussion

2.3.1 Morphology and Structure

Figure 2.2 (a) shows the OM image of the as-synthesized MoS_2 atomic layer on the SiO_2/Si substrate. The MoS_2 layer can be clearly identified with pale blue color in contrast to the SiO_2/Si substrate. The boundary between the MoS_2 and SiO_2/Si is obvious which is marked by dashed red line. Figure 2.2 (b) shows the SEM image of the MoS_2 layer on the SiO_2/Si substrate and the boundary can be clearly observed. Both the OM image and SEM image reveal that the MoS_2 atomic layer synthesized on the SiO_2/Si substrate is continuous over large area, in contrast to the micrometer size of mechanically exfoliated MoS_2 flakes.[1,15] The AFM topographic image of the MoS_2 atomic layer is shown in figure 2.2 (c) and the AFM cross-sectional profile (figure 2.2 (d)) along the white line in figure 2.2 (c) shows that the thickness of the as-synthesized MoS_2 layer is 1.6 nm, which corresponds to the thickness of bilayer MoS_2.[10,13,16]

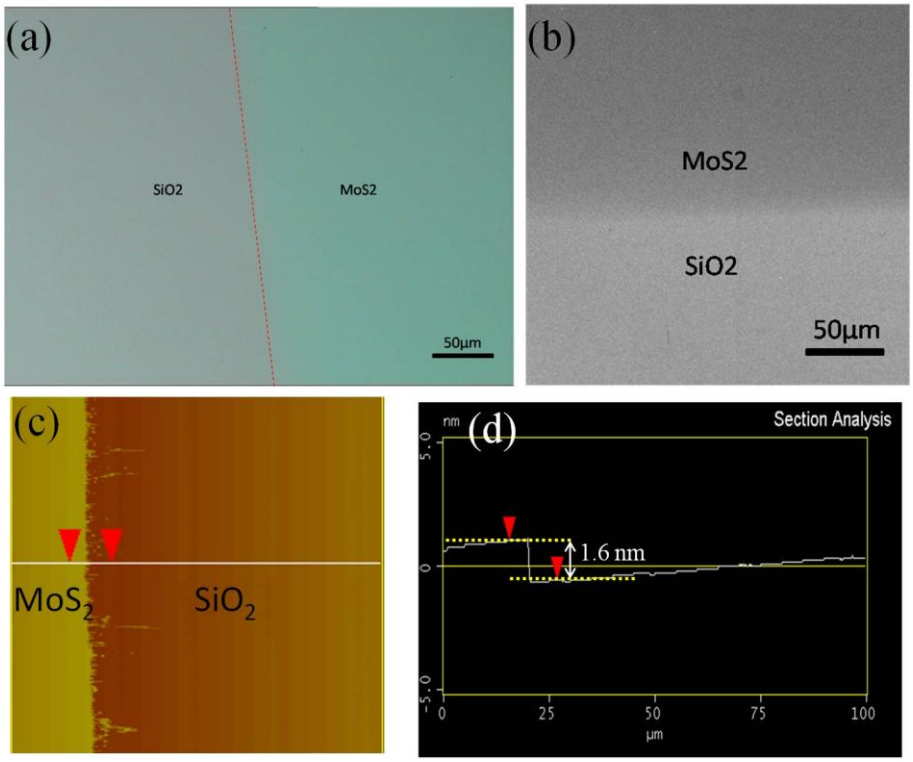

Figure 2.2 (a) OM image, (b) SEM image and (c) AFM image of the as-synthesized MoS_2 atomic layer on SiO_2/Si substrate. (d) AFM cross-sectional profile along the line indicated in (c).

Figure 2.3 shows the HRTEM image of the as-synthesized MoS_2 atomic layer. The HRTEM image reveals hexagonal lattice structure of the MoS_2 atomic layer as highlighted by the red dots, with lattice spacing of 0.27 nm and 0.16 nm respectively assigned to the (100) and (110) planes. XPS was performed to measure the binding energies of Mo and S of the MoS_2 bilayer. Figure 2.4 (a) and (b) respectively shows the XPS survey scans for Mo and S. The Mo 3d shows two peaks at 233.5 eV and 230.35 eV, which correspond to the doublet $Mo3d_{3/2}$ and $Mo3d_{5/2}$, respectively. For S 2p, the two peaks at 164.35 eV and 163.15 eV can be respectively assigned to the

spin-orbit $S2p_{1/2}$ and $S2p_{3/2}$. The XPS results are comparable to the previous reported values for MoS_2 crystals.[17,18]

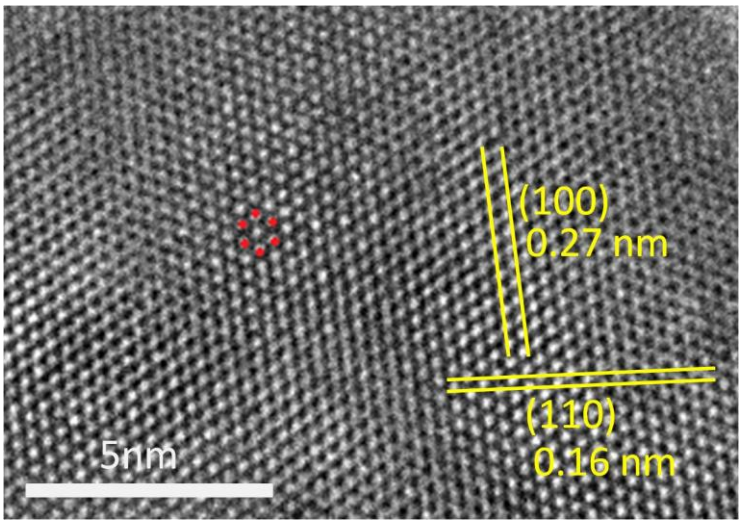

Figure 2.3 HRTEM image of the as-synthesized MoS_2 atomic layer.

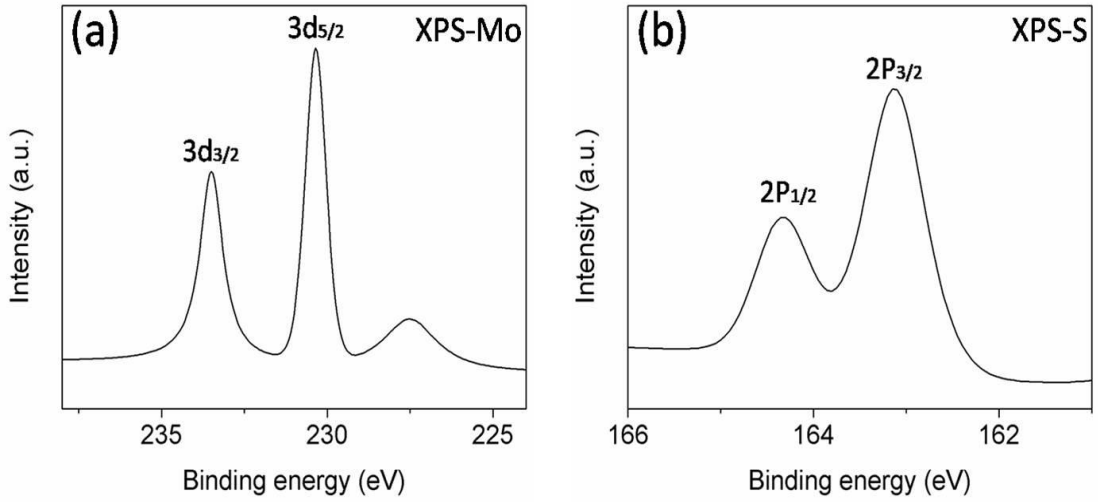

Figure 2.4 XPS spectra of the as-synthesized MoS_2 atomic layer for (a) Mo 3d and (b) S 2p.

2.3.2 Optical Properties

Figure 2.5 (a) shows the Raman spectra of MoS_2 synthesized from 1 nm and 10 nm pre-deposited MoO_3 thin films. The peaks at 384 cm^{-1} (or 380 cm^{-1}) and 404 cm^{-1}

(or 407 cm^{-1}) respectively represents the in-plane (E^1_{2g}) and out-of-plane (A_{1g}) vibrational modes of MoS_2.[19,20] The Raman peak intensity of the thicker MoS_2 layer is higher than that of the thinner one, which may due to more active material to be excited for the thicker layer. It is obvious that the two Raman peaks (E^1_{2g} and A_{1g}) of the MoS_2 atomic layer synthesized from 1 nm pre-deposited MoO_3 thin film shift towards each other as compared to that synthesized from 10 nm pre-deposited MoO_3. The shift of the Raman peaks can be attributed to changes of atomic vibrations resulting from ineffective interlayer interaction of thinner MoS_2 atomic layer.[20] From the frequency difference between the E^1_{2g} and A_{1g} Raman modes, the MoS_2 atomic layer synthesized from 1 nm pre-deposited MoO_3 shows a frequency difference of 20 cm^{-1}, which is in relevant to the value for bilayer MoS_2.[20] The Raman characterization is in good agreement with the AFM measurement that both results confirm bilayer of the MoS_2 synthesized from 1 nm pre-deposited MoO_3 thin film.

Figure 2.5 (b) shows the PL spectra of MoS_2 atomic layers synthesized from 1 nm pre-deposited MoO_3 at different synthesis temperatures (the PL spectrum of MoS_2 synthesized from 10 nm pre-deposited MoO_3 was plotted as reference). While the reference spectrum shows no PL peaks (due to indirect bandgap of thick MoS_2), all the bilayer MoS_2 PL spectra show two PL peaks at about 652 nm and 606 nm which can be respectively assigned to the A1 and B1 direct excitonic transition of the bilayer

MoS_2.[21] With higher synthesis temperature, the intensity of the PL peaks increases, suggesting higher synthesis temperature would lead to higher quality of the MoS_2 due to improvement of crystallinity.

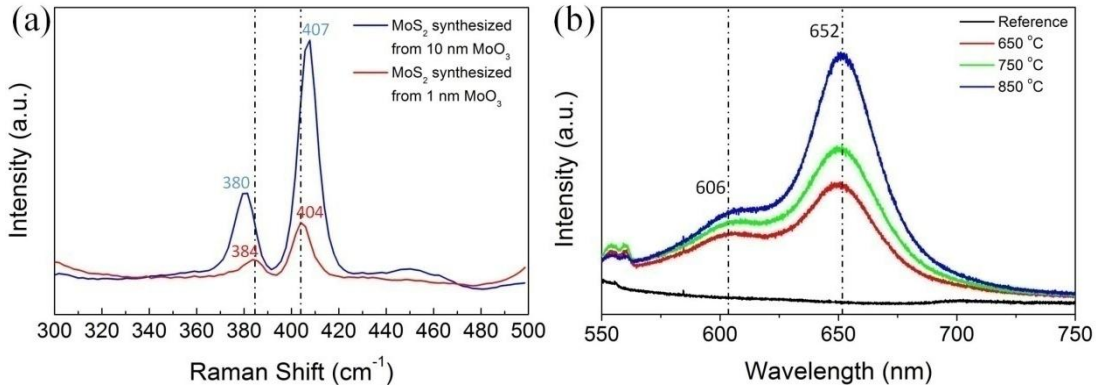

Figure 2.5 (a) Raman spectra of MoS_2 layer synthesized from 1 nm and 10 nm MoO_3 thin films. (b) PL spectra of MoS_2 for different synthesis temperatures (Reference is the PL spectrum of MoS_2 synthesized from 10 nm MoO_3 thin film).

To examine the uniformity of the as-synthesized MoS_2 atomic layer, Raman and PL mappings were performed. Figure 2.6 (a) and (b) respectively shows the Raman mapping of the MoS_2 atomic layer at peak position of 384 cm^{-1} and 404 cm^{-1} over a large area of 80×80 μm^2. The Raman signals are quite uniform throughout the MoS_2 layer. Brighter color shows locally thicker of the layer while the black color may due to the occurrence of pin holes. Figure 2.6 (c) shows the PL mapping of the MoS_2 layer with the same scanned area as the Raman mappings and reveals that the MoS_2 is optically active throughout the scanned area with minor inactive points.

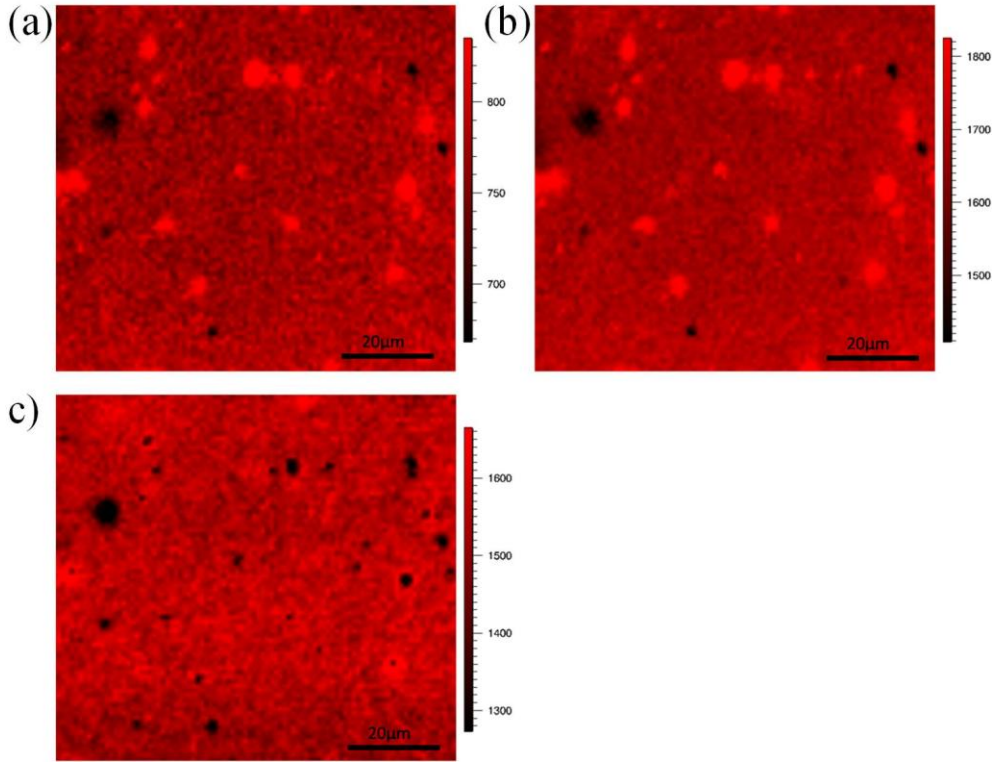

Figure 2.6 Raman mapping of the as-synthesized MoS_2 atomic layer at (a) 384 cm^{-1} and (b) 404 cm^{-1}. (c) PL mapping of the MoS_2 atomic layer at 652 nm.

2.4 Conclusion

Large-area MoS_2 atomically thin layers were successfully prepared by direct sulfurization of MoO_3 pre-deposited thin film. The size of MoS_2 thin layer that can be synthesized depends on the size of the pre-deposited MoO_3 thin film, and wafer-scale synthesis of MoS_2 atomic layer is possible by applying this method. Both Raman characterization and AFM measurement suggested the as-synthesized MoS_2 atomic layer from 1 nm pre-deposited MoO_3 thin film was bilayer in thickness. The evolution of PL peaks at 606 nm and 652 nm manifested direct excitonic transition of the

as-synthesized MoS_2 atomic layer.

2.5 References

[1] K. Novoselov, D. Jiang, F. Schedin, T. Booth, V. Khotkevich, S. Morozov, A. Geim. *Proc. Natl. Acad. Sci. U. S. A.*, **2005**,102, 10451.

[2] B. Radisavljevic, A. Radenovic, J. Brivio, V. Giacometti, A. Kis. *Nature Nanotechnology*, **2011**, 6, 147-150.

[3] M-W. Lin, C. Ling, Y. Zhang, H. J. Yoon, M. M. Cheng, L. A. Agapito, N. Kioussis, N. Widjaja, Z. Zhou. *Nanotechnology*, **2011**, 22, 265201.

[4] X. Li, X. Wang, L. Zhang, S. Lee, H. Dai. *Science*, **2008**, 319, 1229-1232.

[5] M. Y. Han, B. Ozyilmaz, Y. Zhang, P. Kim. *Phys. Rev. Lett*., **2007**, 98, 206805.

[6] R. Balog *et al*. *Nature Mater.*, **2010,** 9, 315-319.

[7] Y. Zhang *et al*. *Nature*, **2009**, 459, 820-823.

[8] K. F. Mak, C. Lee, J. Hone, J. Shan, T. F. Heinz. *Physical Review Letters*, **2010**, 205, 136805.

[9] Q. H. Zhang, K. Kalantar-Zadeh, A. Kis, J. N. Coleman, M. S. Strano. *Nature Nanotechnology*, **2012**, 7, 699-712.

[10] Y. Zhan, Z. Liu, S. Najmaei, P. M. Ajayan, J. Lou. *Small*, **2012**, 8, 996-971.

[11] X. L. Li , Y. D. Li. *Chem. Eur. J*., **2003** , 9 , 2726-2731.

[12] S. Balendhran, J. Z. Ou, M. Bhaskaran, S. Sriram, S. Ippolito, Z. Vasic, E. Kats,

S. Bhargava, S. Zhuiykovd, K. Kalantar-zadeh. *Nanoscale*, **2012**, 4 , 461-466.

[13] A. Castellanos-Gomez, M. Barkelid, A. M. Goossens, V. E. Calado, H. S. J. van der Zant, G. A. Steele, *Nano Lett.*, **2012**, 12, 3187-3192.

[14] Y. Liu, H. Nan, X. Wu, W. Pan, W. Wang, J. Bai, W. Zhao, L. Sun, X. Wang, Z. Ni. *ACS Nano*, **2013**, 5, 4202-4209.

[15] H. Li, Z. Y. Yin, Q. Y. He, X. Huang, G. Lu, D. W. H. Fam, A. I. Y. Tok, Q. Zhang, H. Zhang. *Small*, **2012**, 8, 63-67.

[16] K-K. Liu, W. Zhang, Y-H. Lee, Y-C. Lin, M-T. Chang, C-Y. Su, C-S. Chang, H. Li, Y. Shi, H. Zhang, C-S. Lai, L-J. Li. *Nano Lett.*, **2012**, 12, 1538-1544.

[17] C. N. R. Rao, A. Nag. *Eur. J. Inorg. Chem.*, **2010**, 27, 4244-4250.

[18] C. Altavilla, M. Sarno, P. A. Ciambelli. *Chem. Mater.*, **2011**, 23, 3879-3883.

[19] P. A. Bertrand. *Phys. Rev. B*, **1991**, 44, 5745-5749.

[20] C. Lee, H. Yan, L. E. Brus, T. F. Heinz, J. Hone, S. Ryu. *ACS Nano*, **2011**, 5, 7707-7712.

[21] A. Splendiani, L. Sun, Y. B. Zhang, T. S. Li, J. Kim, C. Y. Chim, G. Galli, F. Wang. *Nano Lett.*, **2010**, 10, 1271-1275.

Chapter 3 CVD Synthesis of 2D MoS_2 and the Study of Its Growth Mechanism

3.1 Introduction

Transition metal dichalcogenides (TMDs) especially MoS_2 have received considerable attention recently due to the indirect- to direct-bandgap transition when the thickness of TMDs decrease to atomically thin layer,[1,2] which show promising to supplement graphene for novel electronic and optoelectronic applications. Although FETs based on exfoliated 2D MoS_2 have demonstrated as low standby-power devices,[3] excellent logic operators,[4,5] sensitive photodetectors[6] and gas sensors,[7] the small size of exfoliated MoS_2 is only suitable for fundamental characterization.[2,8] For practical applications, large area and high quality 2D MoS_2 layer is required as building block for future electronic and optoelectronic integrated circuits.

During the past two years, substantial efforts have been devoted to the synthesis of MoS_2 atomic layers. Early works relied on the sulfurization of Mo-containing thin films to obtain MoS_2 thin layers,[8-10] but the mobilities of the as-prepared MoS_2 thin layers were one to two orders of magnitude less than that of the mechanically exfoliated samples, mainly due to planar defects and randomly distributed nanoscale grains of the sulfurized films.[8] Recently, CVD synthesis of 2D MoS_2 layer through simultaneous vaporization and reaction of Mo and S sources has been reported to

successfully prepare large grain-size (tens of micrometers) 2D MoS_2 layers with mobilities comparable to the mechanically exfoliated MoS_2 layers.[11-14] However, there remain challenges to synthesize large-area 2D MoS_2 with uniform thickness by CVD method. It is therefore necessary to investigate the growth mechanism of MoS_2 in order to obtain reproducible, large-area and uniform 2D MoS_2 atomic layers.

In this work, CVD synthesis of 2D MoS_2 was conducted at different pressures in order to study its growth behaviors. The experimental results revealed that the concentration of S played an important role for MoS_2 growth. While large-area MoS_2 film can be obtained at vacuum, MoS_2 triangular flakes with size of about 20 μm were synthesized under pressure. Larger MoS_2 layers can be formed when the MoS_2 triangular flakes grew and merge with each other. The growth mechanism of 2D MoS_2 was proposed and discussed.

3.2 Experimental Section

3.2.1 CVD Synthesis of 2D MoS_2

Figure 3.1 schematically illustrates the experimental setup for the CVD synthesis of 2D MoS_2 atomic layers. The CVD system was equipped with a tunable valve which allows controlling the synthesis condition inside the system to be either vacuum, ambient or pressure. For a typical synthesis, 2 mg MoO_3 powder (ACS

reagent, ≥99.5%, Sigma-Aldrich) with cleaned SiO_2/Si substrate next to it in the downstream of gas flow was placed at the center of the furnace, and 0.5 g S powder (purum p.a., ≥99.5%, Sigma-Aldrich) was located at the upstream of gas flow where the local temperature was about 120 ^oC (evaporation point of S) when the center temperature reached 650 ^oC. Prior to synthesize, the CVD system was pumped and purged with Ar gas for 10 minutes, and then the pressure was adjusted for the synthesis by controlling the tunable valve. In this experiment, MoS_2 nanostructures were synthesized at different pressures: vacuum (0.2 Torr), ambient pressure (760 Torr) and higher pressure (900 Torr). For the samples synthesized at vacuum (0.2 Torr), the center zone was heated to 650 ^oC with a ramping rate of 20 ^oC/min under 20 sccm Ar flow and hold for 5 minutes before allowing the system to be naturally cooled down to room temperature. In case of the samples synthesized at ambient pressure or higher pressure, a higher temperature was required for the vaporization of MoO_3. The center zone was first heated to 650 ^oC with a ramping rate of 20 ^oC/min and then to 850 ^oC with a rate of 10 ^oC/min under 20 sccm Ar flow. The temperature of 850 ^oC was kept for 5 minutes before naturally cooling the system to room temperature.

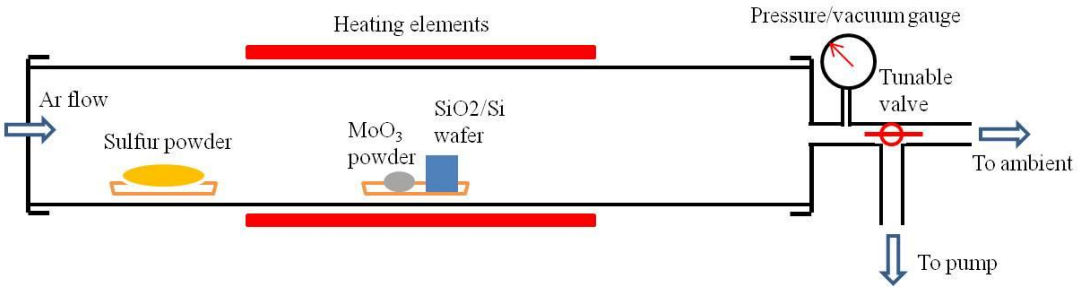

Figure 3.1 Schematic of CVD synthesis of 2D MoS_2 layers in a pressure-adjustable single tube furnace.

3.2.2 Characterization

The morphologies and structures of the as-synthesized MoS_2 nanostructures were characterized by an optical microscope (Olympus) and a Philips FEG-SEM. The thickness of the MoS_2 atomic layer was measured by AFM. The binding energies of Mo and S of the MoS_2 layers were characterized by XPS. Raman and PL spectra of the MoS_2 layers were collected by a Renishaw Raman microscope in ambient air with a 514 nm excitation laser.

3.3 Results and Discussion

3.3.1 Morphology, Structure and Optical Property of CVD Synthesized MoS_2 at Different Growth Pressures

In order to investigate the growth mechanism of 2D MoS_2 atomic layers, the synthesis was conducted at various pressures. Figure 3.2 shows the representative SEM images of the as-synthesized nanostructures which reveals totally different

morphologies obtained at different growth pressures. At growth pressure of 0.2 Torr, the as-synthesized structures were microplates vertically grown from the substrate as shown in figure 3.2 (a). Raman spectrum of the microplates (figure 3.3 (a), Vacuum 1) reveals the characteristic Raman peaks of oxisulfide ($MoOS_2$),[14,15] indicating insufficient supply of S vapor in the synthesis process. If the S source was placed a little bit closer to the center heating zone so that more S was vaporized, large-area and continuous flat layer can be prepared (figure 3.2 (b), the white color indicates scratches in contrast to the layer) and Raman characterization confirmed the as-synthesized layer was MoS_2 (figure 3.3 (b), Vacuum 2). When the synthesis was processed at ambient pressure, rhombic microplates were formed (figure 3.2 (c)) and the Raman spectrum (figure 3.3 (a), Ambient) shows that the rhombic microplates were $MoOS_2$.[14] The rhombic $MoOS_2$ microplates can be further sulfurized and separated to obtain highly crystalline MoS_2 flakes as previously reported.[11] Figure 3.2 (d) and (e) show the SEM images of the nanostructures synthesized at pressure of 900 Torr. It is obvious that triangular flakes with size of about 20 μm were deposited on the SiO_2/Si substrate under pressure. Raman characterization confirmed the as-synthesized triangular flakes were MoS_2 (figure 3.3 (b), Pressure) and the frequency difference between the two characterization peaks (20 cm^{-1}) suggests the MoS_2 triangular flakes were bi-layer in thickness.[16] From figure 3.2 (e), it can be

observed that individual MoS_2 triangular flakes gradually grew and merged with each other to form a larger and continuous MoS_2 layer. It can be deduced that by continuously supplying the reacting sources, large-area and continuous MoS_2 layer can be eventually synthesized.

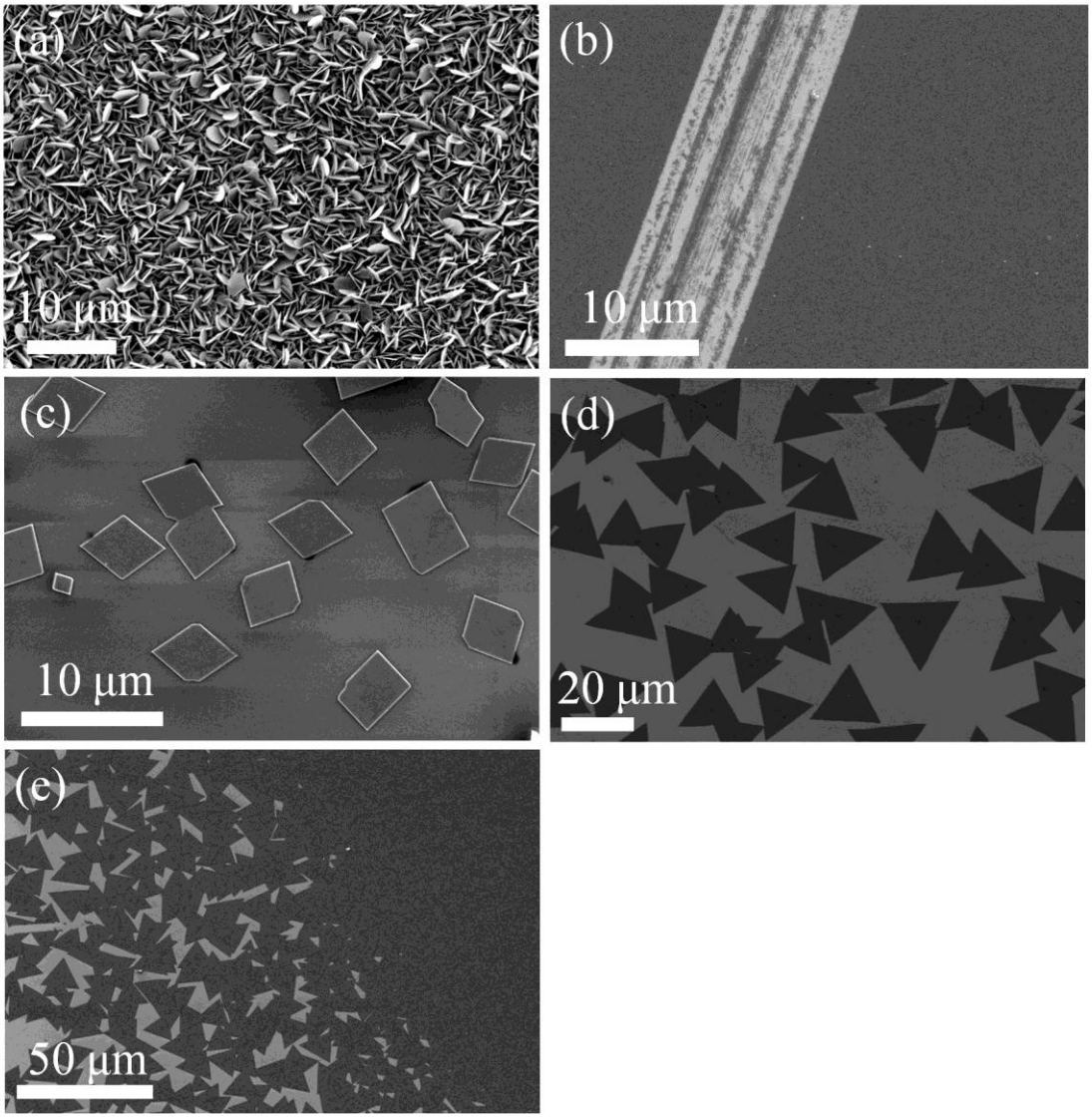

Figure 3.2 SEM images of CVD synthesized MoS_2 nanostructures under growth pressure of (a) and (b) 0.2 Torr, (c) ambient pressure (760 Torr), (d) and (e) 900 Torr.

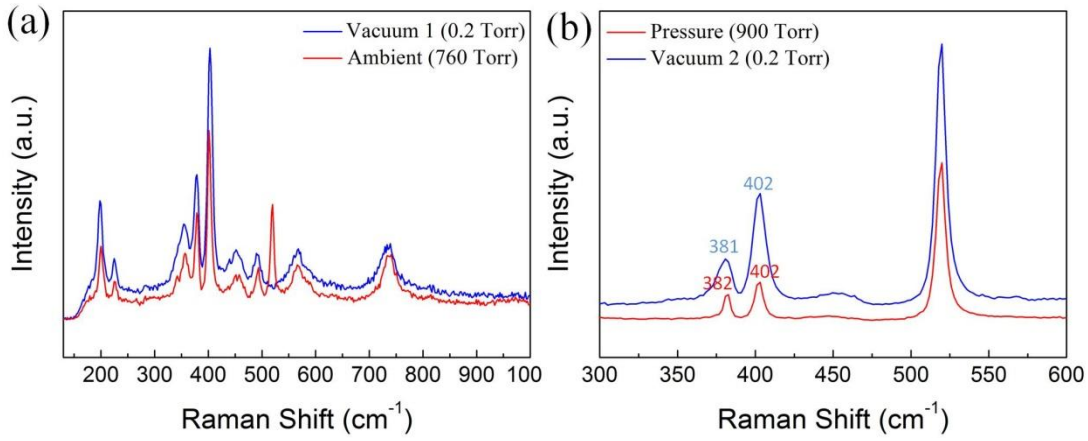

Figure 3.3 Raman spectra of CVD synthesized nanostructures under growth pressure of (a) 0.2 Torr (Vacuum 1) and ambient pressure, and (b) 0.2 Torr (Vacuum 2, with S source placed closer to the center heating zone in respect to the case of Vacuum 1) and 900 Torr (Pressure).

The formation of atomically thin MoS_2 triangular flakes can be directly visualized by optical microscope since interference color alters when the atomic layers add up from the substrate.[17] Figure 3.4 shows the OM images of the MoS_2 triangular flakes deposited on the SiO_2/Si substrate. From figure 3.4 (a), there is an obvious dot at the center of each triangular flakes. These dots may account for the nucleation sites for the flake growth. By comparing figure 3.4 (a) and (b), individual MoS_2 triangular flakes continuously grew and merged with each other to form larger layers. Figure 3.5 (a) shows the AFM topographic image of the MoS_2 triangular flakes and reveals that the surface of the as-synthesized MoS_2 flakes were not very smooth. The occurrence of particles on the surface may be the nucleation sites for additional

layer growth of the flakes. The triangular flakes tend to merge with each other to form larger layers and each flake represents a grain of a particular layer. Figure 3.5 (b) shows the AFM cross-sectional profile along the dashed red line of figure 3.5 (a). The measured thickness of the MoS_2 layers was 1.48 nm and 1.84 nm, corresponding to MoS_2 with 2-3 layers, which is in good agreement with the Raman characterization result (figure 3.3 (b), Pressure).

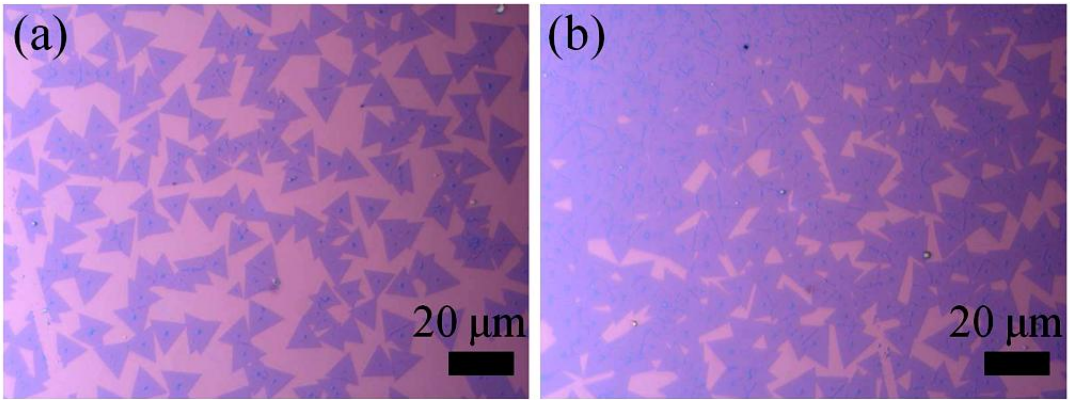

Figure 3.4 OM images of MoS_2 triangular flakes synthesized at pressure of 900 Torr.

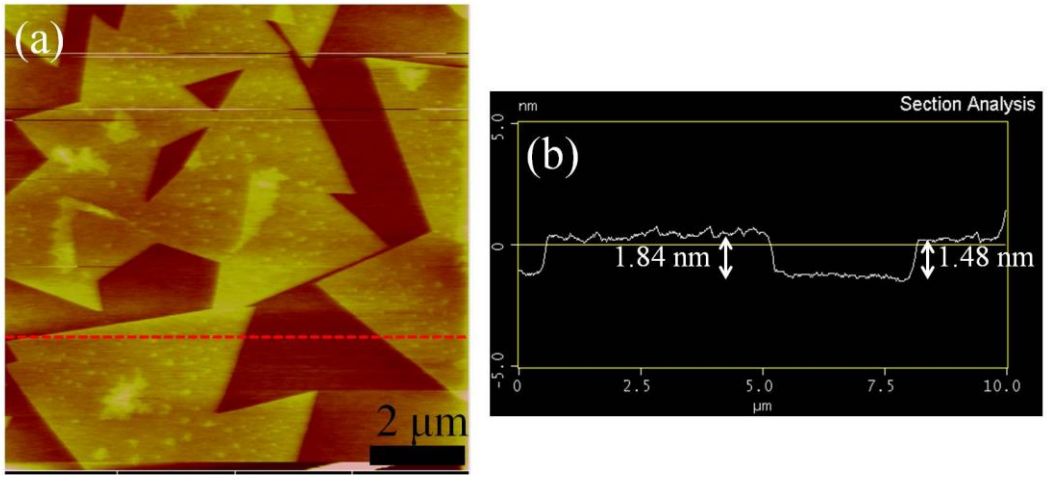

Figure 3.5 (a) AFM topographic image of the as-synthesized MoS_2 triangular flakes on SiO_2/Si substrate. (b) AFM cross-sectional profile along the dashed red line indicated in (a).

Figure 3.6 (a) and (b) respectively shows the XPS survey scans for Mo and S of the MoS_2 triangular flakes. The Mo 3d shows two peaks at 232.2 eV and 229.2 eV, which correspond to the doublet $Mo3d_{3/2}$ and $Mo3d_{5/2}$, respectively. For S 2p, the two peaks at 163.1 eV and 162 eV can be respectively assigned to the spin-orbit $S2p_{1/2}$ and $S2p_{3/2}$. The XPS results are comparable to the previous reported values for MoS_2 crystals.[18,19]

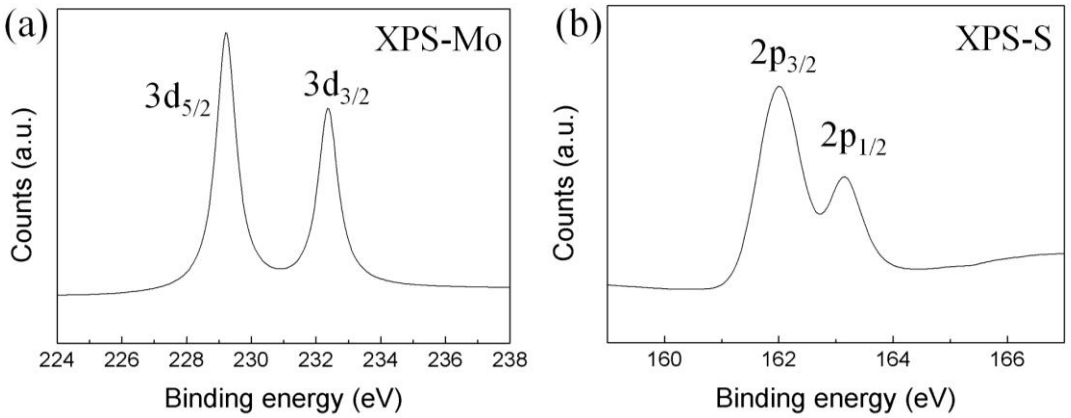

Figure 3.6 XPS spectra of the as-synthesized MoS_2 triangular flakes for (a) Mo 3d and (b) S 2p.

The PL spectra of MoS_2 nanostructures synthesized at different pressures are shown in figure 3.7. It is reasonable that there are no PL signals for the $MoOS_2$ microplates synthesized at 0.2 Torr (Vacuum 1) and ambient pressure. For the MoS_2 layer synthesized at 0.2 Torr (Vacuum 2, with S source placed closer to the center heating zone), a pronounced PL peak at 664 nm can be observed. On the other hand, the MoS_2 triangular flakes synthesized at pressure of 900 Torr showed a PL peak at

682 nm with a smaller full-width at half maximum (FWHM). The difference between the PL peak positions may due to different synthesis pressures or the different layer thickness, which requires further investigations. The emergence of PL indicates direct excitonic transition of the as-synthesized MoS_2 atomic layers. Figure 3.8 (b) shows the PL mapping image of the MoS_2 triangular flakes at 682 nm in the marked region of figure 3.8 (a). The MoS_2 flakes are optically active over large area and the dark fringes denote the boundaries of adjacent MoS_2 layers. The MoS_2 layers can further grow and join together to form larger and continuous layers.

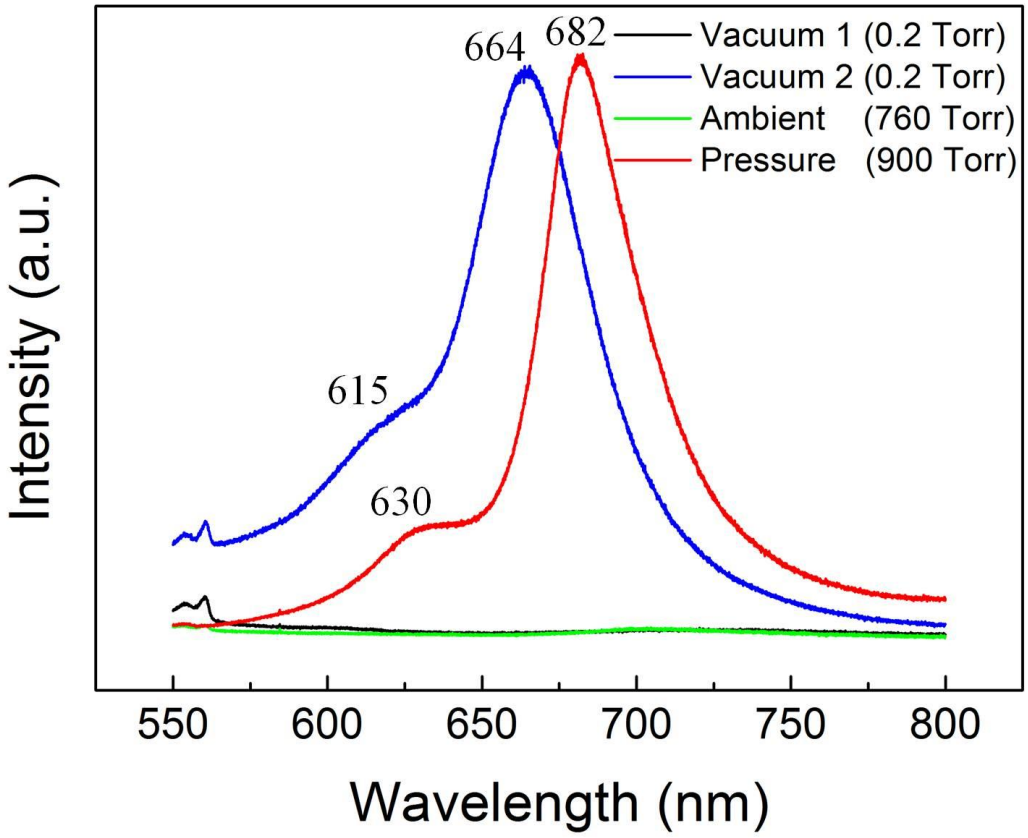

Figure 3.7 PL spectra of MoS_2 nanostructures synthesized at different pressures.

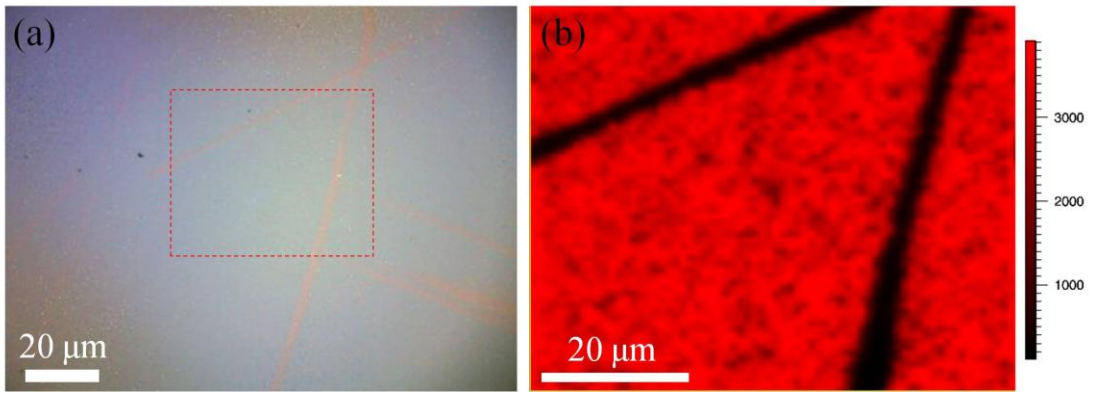

Figure 3.8 (a) OM image of several MoS_2 flakes ready to merge with each other. (b) PL mapping image at 682 nm in the marked region of (a).

By using similar synthesis method, $MoSe_2$ thin film was successfully synthesized on SiO_2/Si substrate at vacuum through simultaneous vaporization of Mo and Se sources. Figure 3.9 (a) shows the Raman spectrum of the as-synthesized $MoSe_2$ film and the peaks of 239 cm^{-1} and 285 cm^{-1} respectively represent the A_{1g} and E^1_{2g} Raman modes of $MoSe_2$.[20] Figure 3.9 (b) shows the PL spectrum of the $MoSe_2$ film, and the occurrence of the PL peak at 785 nm manifests direct excitonic transition of the as-synthesized $MoSe_2$ film.[20] The PL mapping image of the $MoSe_2$ film is shown in figure 3.9 (c) and the PL signal is uniform over large area.

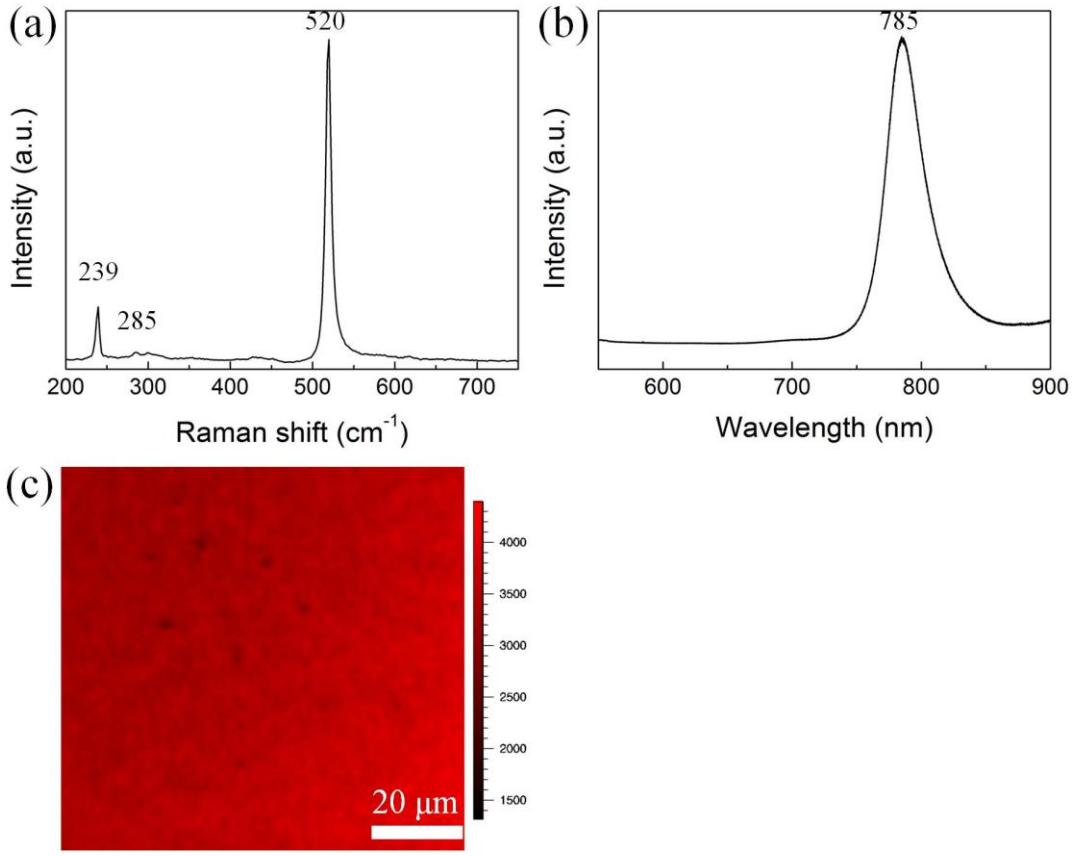

Figure 3.9 (a) Raman spectrum and (b) PL spectrum of CVD synthesized $MoSe_2$ layer. (c) PL mapping image of the as-synthesized $MoSe_2$ layer at 785 nm.

3.3.2 Study of the Growth Mechanism of MoS_2

From the results of the MoS_2 nanostructures synthesized at vacuum (0.2 Torr), the position of the S source in the synthesis process, or the supply of S vapor, is critical to the formation of MoS_2 layers. If the S source was placed at the point of local temperature 120 ^{o}C (evaporation point of S) relative to the center zone temperature of 650 ^{o}C, only oxisulfide $MoOS_2$ microplates formed. However, MoS_2 thin film can be synthesized if the S source was moved a little bit closer (5 cm) to the

center heating zone. Hence, it can be deduced that in the synthesis process under vacuum, the S vapor first reduced the MoO_3 to volatile intermediate suboxide MoO_{3-x}.[12,14,21] Subsequently, the MoO_{3-x} diffused to the receiving substrate and further reduced by S vapor to form MoS_2 film if sufficient amount of S vapor was supplied, otherwise $MoOS_2$ would form instead.[12,14,21]

In case of the synthesis conducted at ambient pressure, only rhombic $MoOS_2$ microplates formed wherever the S powder placed and whatever how much S powder loaded (up to 1.2 g). Previous literatures have shown that MoS_2 layers can be synthesized at ambient pressure with the assist of aromatic molecules as catalysts.[12,13] However, it can be predicted that without the presence of catalysts, a higher concentration of S vapor is required for the formation of MoS_2 layers. One way to increase the S concentration is to increase the partial pressure of S vapor by adjusting the gas outlet valve. In case of the synthesis processed at pressure of 900 Torr, MoS_2 triangular flakes were formed and validates higher S concentration is critical for MoS_2 formation under pressure. The S vapor reduced the MoO_3 source to MoO_{3-x} species and the MoO_{3-x} eventually diffused to and further reacted with S to form MoS_2 nuclei on the receiving substrate. The nuclei can be clearly identified at the center of each MoS_2 flakes as shown in OM image of figure 3.4 (a). The MoS_2 then grew to form triangular flakes and merged with each other to form larger layers when the reaction

proceeded. The formation and coalescence of MoS_2 triangular flakes are shown in SEM images of figure 3.2 (d) and (e), and OM images in figure 3.4. Each triangular flake represents a grain of a merged MoS_2 layer. While the MoS_2 triangular flakes grew laterally to larger size, the bottom-up layer growth also happened simultaneously as shown in the AFM topographic image of figure 3.5 (a).

The study of MoS_2 growth at different pressures can help to know more about the growth behaviors of MoS_2. But it is still challenging to controllable prepare large-area MoS_2 layer with uniform thickness by CVD method. A feasible solution to this problem is to explore catalytic substrate for epitaxial growth of MoS_2, similar to the case of CVD graphene growth on Cu substrate.

3.3 Conclusion

MoS_2 nanostructures with different morphologies were synthesized at different growth pressures by CVD method. At vacuum (0.2 Torr), large-area MoS_2 thin film formed if sufficient amount of S vapor was supplied for the reduction of MoO_3 source, otherwise vertical $MoOS_2$ microplates formed instead. At ambient pressure, only rhombic $MoOS_2$ microplates formed. By increasing the synthesis pressure to 900 Torr, the S concentration increased and MoS_2 triangular flakes with size of 20 μm can be prepared. Both the MoS_2 samples prepared at vacuum and pressure showed a pronounced PL peak, indicating direct excitonic transition of the as-synthesized MoS_2

atomic layers. Raman characterization and AFM measurement revealed the thickness of as-synthesized MoS_2 triangular flakes was 2-3 layers. Base on the experimental results, sufficient supply of S vapor is critical for the MoS_2 formation. The MoS_2 CVD growth mechanism can be proposed to be S reduction of MoO_3 to MoO_{3-x} followed by subsequent S reduction of MoO_{3-x} to MoS_2 on the substrate surface. For MoS_2 triangular flakes, they grow and merge with each other to form large layers if the reaction proceeds.

3.4 References

[1] K. F. Mak, C. Lee, J. Hone, J. Shan, T. F. Heinz. *Physical Review Letters*, **2010**, 205, 136805.

[2] Q. H. Zhang, K. Kalantar-Zadeh, A. Kis, J. N. Coleman, M. S. Strano. *Nature Nanotechnology*, **2012**, 7, 699-712.

[3] B. Radisavljevic, A. Radenovic, J. Brivio, V. Giacometti, A. Kis. *Nature Nanotechnology*, **2011**, 6, 147-150.

[4] B. Radisavljevic, M. B. Whitwick, A. Kis, *ACS Nano*, **2011**, 5, 9934-9938.

[5] H. Wang, L. Yu, Y-H. Lee, Y. Shi, A. Hsu, M. L. Chin, L-J. Li, M. Dubey, J. Kong, T. Palacios, *Nano Lett.*, **2012**, 12, 4674-4680.

[6] Z. Y. Yin, H. Li, L. Jiang, Y. M. Shi, Y. H. Sun, G. Lu, Q. Zhang, X. D. Chen, H. Zhang. *ACS Nano*, **2012**, 6, 74-80.

[7] H. Li, Z. Y. Yin, Q. Y. He, X. Huang, G. Lu, D. W. H. Fam, A. I. Y. Tok, Q. Zhang, H. Zhang. *Small*, **2012**, 8, 63-67.

[8] Y. Zhan, Z. Liu, S. Najmaei, P. M. Ajayan, J. Lou. *Small*, **2012**, 8, 996-971.

[9] Y-C. Lin, W. Zhang, J-K. Huang, K-K. Liu, Y-H. Lee, C-T. Liang, C-W. Chu, L-J. Li. *Nanoscale*, **2012**, 4, 6637-6641.

[10] K-K. Liu, W. Zhang, Y-H. Lee, Y-C. Lin, M-T. Chang, C-Y. Su, C-S. Chang, H. Li, Y. Shi, H. Zhang, C-S. Lai, L-J. Li. *Nano Lett.*, **2012**, 12, 1538-1544.

[11] X. Wang, H. Feng, Y. Wu, L. Jiao. *JACS*, **2013**, 135, 5304-5307.

[12] Y-H. Lee, X-Q. Zhang, W. Zhang, M-T. Chang, C-T. Lin, K-D. Chang, Y-C. Yu, J. T-W. Wang, C-S. Chang, L-J. Li. *Adv. Mater.*, **2012**, 24, 2320-2325.

[13] Y-H. Lee, L. Yu, H. Wang, W. Fang, X. Ling, Y. Shi, C-T. Lin, J-K. Huang, M-T. Chang, C-S. Chang, M. Dresselhaus, T. Palacios, L-J. Li, J. Kong. *Nano Lett.*, **2013**, 13, 1852-1857.

[14] S. Najmaei, Z. Liu, W. Zhou, X. Zou, G. Shi, S. Lei, B. I. Yakobson, J-C. Idrobo, P. M. Ajayan, J. Lou. *Nature Mater.*, **2013**, 12, 754-759.

[15] T. Weber, J. C. Muijsers, J. H. M. C. van Wolput, C. P. J. Verhagen, J. W. Niemantsverdriet. *J. Phys. Chem.*, **1996**, 100, 14144-14150.

[16] C. Lee, H. Yan, L. E. Brus, T. F. Heinz, J. Hone, S. Ryu. *ACS Nano*, **2011**, 5, 7707-7712.

[17] K. Novoselov, D. Jiang, F. Schedin, T. Booth, V. Khotkevich, S. Morozov, A. Geim. *Proc. Natl. Acad. Sci. U. S. A.*, **2005**,102, 10451.

[18] C. N. R. Rao, A. Nag. *Eur. J. Inorg. Chem.*, **2010**, 27, 4244-4250.

[19] C. Altavilla, M. Sarno, P. A. Ciambelli. *Chem. Mater.*, **2011**, 23, 3879-3883.

[20] S. Tongay, J. Zhou, C. Ataca, K. Lo, T. S. Matthews, J. Li, J. C. Grossman, J. Wu. *Nano Lett.*, **2012**, 12, 5576-5580.

[21] X. L. Li, Y. D. Li. *Chem. Eur. J.*, **2003**, 9, 2726 – 2731.

Chapter 4 Facile PVP-assisted Hydrothermal Synthesis of MoS_2 Nanosphere Network as High Performance Lithium-ion Battery Anode and Superior Electrocatalyst for Hydrogen Evolution Reaction

4.1 Introduction

Rechargeable lithium-ion batteries (LIBs) have been practically applied in a wide range of portable electronics owing to their high voltage delivery, high energy density and safety.[1,2] However, there remain challenges for the development of LIBs with higher energy density and higher rate performance in powering future advanced electrical devices and electric vehicles (EVs). The current commercially available LIBs are mainly based on graphitic anodes, where the low specific capacity of graphitic materials (372 mA h g^{-1}) hinders their practical uses for future application demands. Among all the LIB anode materials, Si posses the highest specific capacity of 4200 mA h g^{-1}[3,4] and has been regarded as one of the most promising next generation anode materials. However, Si suffers from severe pulverization due to large volume variation up to 280 % upon lithiation and delithiation, which causes rapid capacity fading.[5,6] Although recent reports showed that core-shell Si-C empty space engineered nanostructures can improve the performance of Si-based LIBs,[7-10] such empty space engineering increases the fabrication complexity. As analogues of

graphite, transition metal dichalcogenides (TMDs), such as MoS_2 and WS_2, have received extensive research interests due to their unique layered structure with higher specific capacity, among which MoS_2 has attracted much attention because of the emerging physical and chemical properties of its 2D counterpart.[11-13] As a typical TMD, MoS_2 has a layered S-Mo-S structure in which weak van der Waals force interacts between the layers.[11] Owing to the weakly bonded layered structure and relatively reactive edge sites, MoS_2 has contributed to a diverse range of applications such as super lubricant,[14,15] transistors,[12] gas sensors,[16] hydrodesulfurization (HDS) in oil refining,[17] hydrogen evolution reaction (HER)[18,19] and LIBs.[20-24] For LIB applications, MoS_2 shows high specific capacity of 670 mA h g^{-1} with a 4-electron transfer reaction during the charge and discharge processes.[22] While bulk MoS_2 exhibits poor electrochemical performance, nanostructured MoS_2, for instant, nanorods,[25] nanotubes,[24] nanosheets,[22] nanoplates[23] and nanospheres[21], have shown improved Li-ion storage capacity, cycling stability and rate capability. On the other hand, carbon-based MoS_2 nanocomposites (MoS_2 dispersed in graphene, carbon nanotubes or amorphous carbon) also show promising electrochemical properties.[26-30] In case of nanostructural engineering, one strategy to effectively enhance the Li-ion storage property and rate performance is to engineer MoS_2 with larger interlayer separation that provides fast Li-ion diffusion channels.[21,23]

Herein, we report the synthesis of MoS_2 nanosphere network by facile PVP-assited hydrothermal reaction process. The as-synthesized MoS_2 nanospheres were characterized to have expanded interlayer distance in the (002) plane which provides fast ion diffusion channels. LIB anodes based on the MoS_2 nanosphere network showed enhanced electrochemical performance that delivered high reversible discharge capacity of ~850 mA h g^{-1} at 0.5 C for 200 cycles, and exhibited high rate capability up to 10 C. Moreover, the MoS_2 nanosphere network was demonstrated as electrocatalyst for hydrogen evolution reaction with enhanced electrocatalytic activity.

4.2 Experimental Section

4.2.1 Synthesis of MoS_2 Nanospheres

In a typical synthesis, 0.5 mmol of ammonium molybdate tetrahydrate ($(NH_4)_6Mo_7O_{24}\cdot 4H_2O$, Sigma-Aldrich) and 7 mmol of thiourea (CH_4N_2S, ACS Reagent, ≥99.0%, Sigma-Aldrich) were dissolved in 30 mL deionized water under stirring for 30 minutes. Then 0.05-0.5 g of Polyvinylpyrrolidone (PVP, Average mol wt 40,000, Sigma-Aldrich) was added to the mixture and stirred for another 30 minutes to form a homogeneous solution. After that, the mixture was transferred to a 45 mL Teflon-lined stainless steel autoclave and reacted at 180 ^oC for 24 hours. After cooling down to room temperature, the final product was washed with deionized

water and absolute ethanol for several times to remove any residue ions and PVP. Finally, the product was frozen and dried in a vacuum freeze dryer overnight.

4.2.2 Synthesis of MoS_2 Nanosheets

The synthesis of MoS_2 nanosheets was exactly the same as the synthetic procedure of MoS_2 nanospheres, but without the addition of PVP.

4.2.3 Cell Assembly and Electrochemical Measurements

The MoS_2 anodes were prepared by mixing the as-synthesized MoS_2 samples with carbon black and sodium carboxymethyl cellulose (Aldrich) at a weight ratio of 7:2:1, followed by mixing with few drops of deionized water to form a slurry. The slurry was transferred and pasted uniformly on a Cu foil. The electrode was then dried at 100 ^oC in a vacuum oven overnight to remove the water content before punching into 9/16 inch disks. Half-cells were assembled in an argon-filled MBraun glovebox (with both H_2O and O_2 contents less than 0.1 ppm) using Li foil as the counter electrode and 1 M $LiPF_6$ dissolved in ethylene carbonate (EC) and ethylene methyl carbonate (DMC) (EC:DMC, 1:1 vol %) as the electrolyte. Galvanostatic charging and discharging in a voltage range of 0.01-3 V were performed on a MACCOR 4000 battery test system at room temperature. Cyclic voltammetric (CV) scans were conducted on a CHI 600D electrochemical workstation in a potential window of

0.01-3 V at a sweep rate of 0.1 mV s^{-1}. Electrochemical impedance spectroscopy (EIS) was carried out on an IM6 electrochemical workstation (ZAHNER elektrik) in a frequency range of 100 kHz-0.01 Hz.

4.2.4 Characterization

The morphologies and structures of the as-synthesized samples were characterized by a Philips scanning electron microscope (SEM) and a Philips CM200 transmission electron microscope (TEM) operated at 200 kV. High resolution transmission electron microscopy (HRTEM) images of the samples were captured by Gatan GIF 200 equipped to the TEM. Energy-dispersive X-ray (EDX) spectroscopy was performed using EDAX system attached to the SEM. X-ray diffraction (XRD) patterns of the samples were carried out on a Philips X'Pert X-ray diffractometer and Raman spectra were collected by a Renishaw Raman microscope in ambient air with a 514 nm excitation laser.

4.3 Results and Discussion

4.3.1 Morphologies and Structures of as-Synthesized MoS_2 Nanostructures

The morphologies of the as-synthesized MoS_2 nanostructures are shown in figure 4.1. Figure 4.1 (a) shows the representative SEM image of the MoS_2 sample without adding PVP during the hydrothermal synthesis, which displays a randomly oriented

flower-like morphology without specific shape. The corresponding EDX spectrum and Mo:S atomic ratio (figure 2 (a)) confirm the sample is stoichiometric MoS_2. The TEM image of the flower-like MoS_2 structure is shown in figure 4.3 (a), which reveals such structure is composed of nanosheets. HRTEM image in figure 4.3 (f) shows that the nanosheets were formed by 4-8 stacked layers with interlayer separation of 0.63 nm, in correspond to the MoS_2 interlayer distance in the (002) plane. Hereafter, we regard this MoS_2 sample without the addition of PVP as MoS_2 nanosheets.

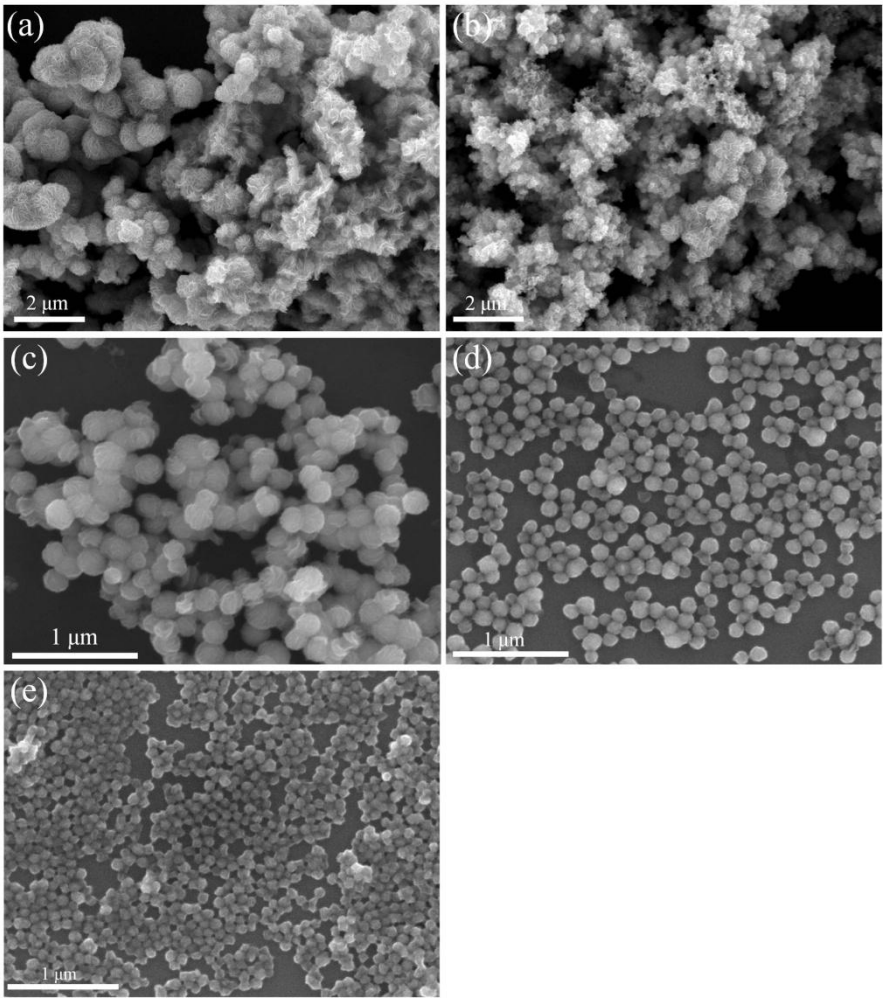

Figure 4.1 Representative SEM images of the as-synthesized MoS_2 nanostructures with PVP addition of (a) 0 g, (b) 0.05 g, (c) 0.1 g, (d) 0.3 g and (e) 0.5 g in the synthesis process.

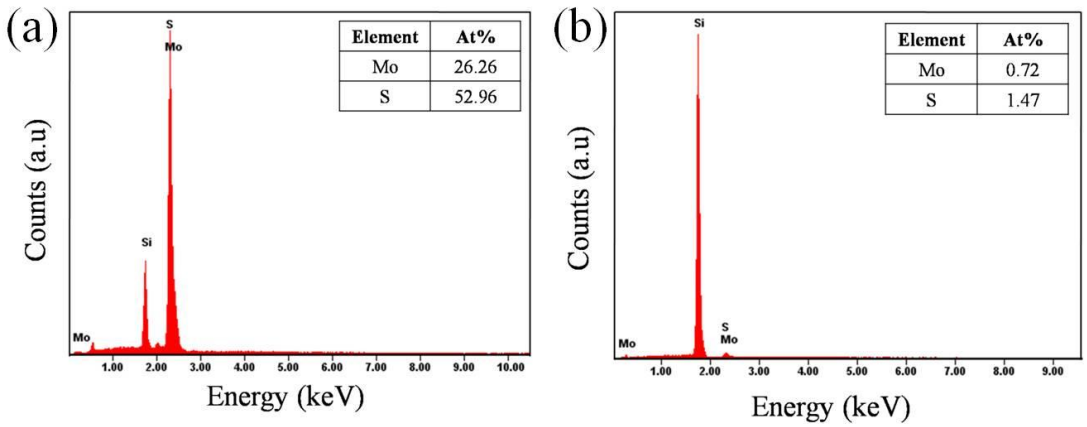

Figure 4.2 EDX spectra and relative atomic weight (inset) of (a) MoS_2 nanosheets without addition of PVP, and (b) MoS_2 nanospheres with 0.5 g PVP addition in the synthesis.

By adding PVP in the synthesis process, MoS_2 nanospheres with narrow size distribution can be obtained and the size of the nanospheres can be manipulated through varying the PVP concentration. Figure 4.1 (b) to (e) respectively show the SEM image of the MoS_2 sample at PVP addition of 0.05 g, 0.1 g, 0.3 g and 0.5 g. At low PVP addition of 0.05 g, no obvious nanospheres can be observed, but the size of the MoS_2 nanostructure significantly shrinks as compared to that of the pristine one (figure 4.1 (a)). Starting from PVP addition of 0.1 g, MoS_2 nanospheres were formed with mean diameter of 180 nm. Further increasing the concentration of PVP induces

smaller size of the as-synthesized MoS_2 nanospheres. The measured mean diameter of the MoS_2 nanospheres at PVP addition of 0.3 g and 0.5 g are 120 nm and 80 nm, respectively. Figure 4.3 (b) to (d) respectively show the TEM image of the MoS_2 nanospheres at PVP addition of 0.1 g, 0.3 g and 0.5 g. It is interesting to note that the nanospheres are in fact interlinked to each other forming a nanosphere network. For electrochemical applications (e.g. Li-ion battery and hydrogen evolution reaction), such a network can be served as effective conductive pathway for efficient electron transport. Higher magnification TEM image of the MoS_2 nanospheres with 80 nm mean diameter (figure 4.3 (e)) reveals that the nanospheres are composed of extensive exposed edge sites. It has been previously reported that such exposed edge sites are beneficial for efficient electrochemical reactions. Figure 4.3 (g) shows the corresponding HRTEM image of the 80 nm MoS_2 nanospheres. The MoS_2 nanospheres consist of randomly oriented discrete layers without long-range ordering of stacked layers that can be observed in the case of MoS_2 nanosheets. The measured interlayer distance is about 0.7 nm, much larger than that of the nanosheets (0.63 nm). It can be deduced that in the PVP-assisted synthesis process, PVP not only serve as surfactant for the formation of MoS_2 nanospheres but also lead to the occurrence of disordered layers with expanded interlayer distance. According to previous literatures, such an expanded interlayer distance of disordered MoS_2 layers can provide fast

conductive channels for Li-ion intercalation and lead to better material utilization in LIB applications. Figure 4.2 (b) shows the EDX spectrum and the Mo:S atomic ratio of the 80 nm MoS_2 nanospheres, suggesting the as-synthesized nanospheres are stoichiometric MoS_2. In this work, we chose the MoS_2 nanosphere network with 80 nm sphere mean diameter as representative Li-ion battery anode material for the electrochemical tests.

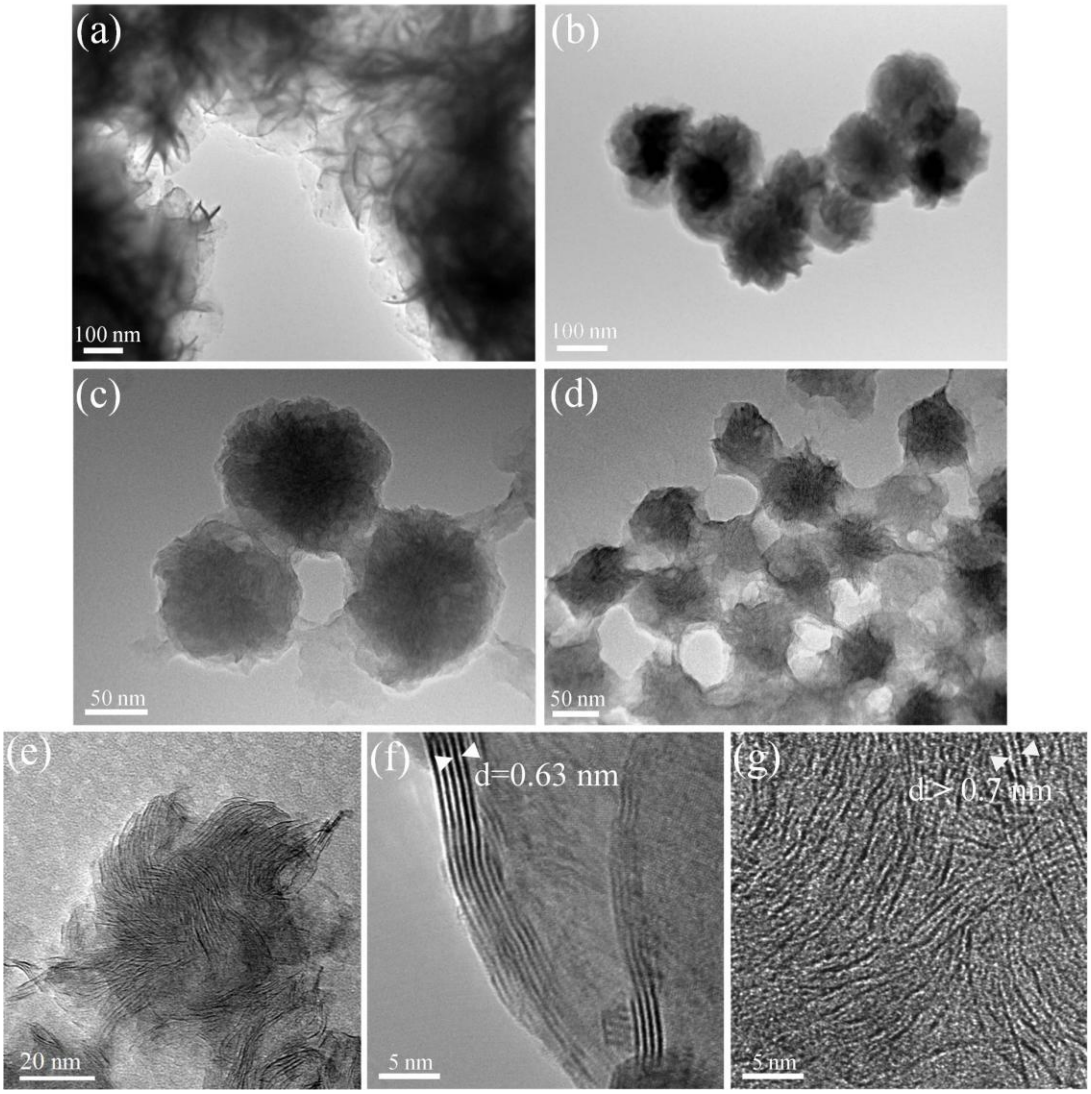

Figure 4.3 TEM image of MoS_2 nanostructures synthesized with PVP addition of (a) 0 g, (b) 0.1 g, (c) 0.3 g and (d) 0.5 g. (e) Higher magnification TEM image of individual

MoS_2 nanosphere from figure 4.3 (d). HRTEM image of MoS_2 nanostructures synthesized with PVP addition of (f) 0 g and (g) 0.5 g.

The crystallographic structures of the as-synthesized MoS_2 nanosheets and nanosphere network were examined by XRD, and the corresponding XRD patterns are shown in figure 4.4 (a). For the MoS_2 nanosheets, the diffraction peaks at around 2θ = 14, 29, 32.8, 35.5, 58 and 60 are well assigned to the (002), (004), (100), (102), (110) and (008) crystal planes of hexagonal MoS_2 phase respectively (JCPDS 37-1492). On the other hand, the MoS_2 nanosphere network exhibits three diffraction peaks at around 2θ = 12.3, 33 and 58. The latter two peaks are respectively correspond to the (100) and (110) crystal planes. However, the first peak shifts significantly to a lower degree with respect to the (002) crystal plane, and the peak value is equivalent to an interlayer distance of about 0.72 nm as calculated by Bragg's equation, which is in consistent with the as-measured interlayer distance from the HRTEM image (figure 4.3 (g)). Figure 4.4 (b) shows the Raman spectrum of the MoS_2 nanosheets and nanosphere network. Both spectrum exhibit two MoS_2 characterization Raman peaks, whereas the lower and higher peak values are respectively correspond to the in-plane phonon mode (E^1_{2g}) and out-of-plane phonon mode (A_{1g}). However, as compared to the MoS_2 nanosheets, the MoS_2 nanosphere network shows smaller difference between the E^1_{2g} and A_{1g} peak frequencies.

According to previous reports, smaller difference between the E^1_{2g} and A_{1g} peak frequencies indicates thinner of the MoS_2 layer thickness. The Raman results suggest the MoS_2 nanospheres are composed of less number of MoS_2 layers.

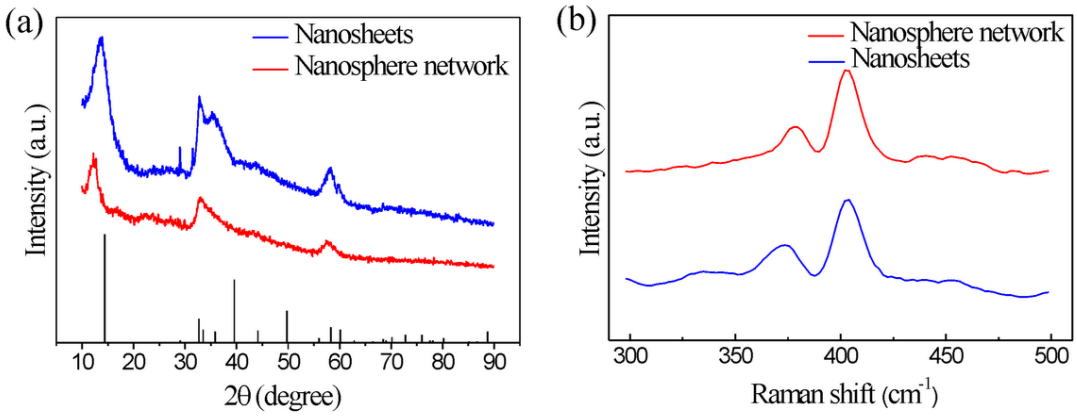

Figure 4.4 (a) XRD patterns and (b) Raman spectra of MoS_2 nanosheets and nanosphere network.

4.3.2 Electrochemical Properties of the as-synthesized MoS_2 Nanosphere Network

To evaluate the electrochemical properties of the MoS_2 nanosphere network, galvanostatic charge and discharge measurements were performed and the cycling performance under current density of 0.5 C (1 C = 670 mA g^{-1}) is shown in figure 4.5 (a). Lower current densities were applied for the first four cycles (0.1 C for the first cycle and 0.2 C for the rest three cycles) in order to activate the active materials in the early stage. The initial discharge and charge capacities of the MoS_2 nanosphere network are respectively 1254 mA h g^{-1} and 917 mA h g^{-1}, corresponding to an initial

Coulombic efficiency of 73.1 %. The capacity loss is mainly attributed to irreversible processes including electrolyte decomposition, solid-electrolyte interface (SEI) layer formation and trapping of Li-ions in the lattice. At the 5^{th} cycle, the MoS_2 nanosphere network delivered a high specific charge capacity of 834 mA h g^{-1}, and remained very stable with a slow increasing trend in the rest of the cycles. After 200 cycles, the specific charge capacity retained 866 mA h g^{-1}, showing excellent capacity retention of 94.4 % with respect to the first charge capacity. For a comparison, the cycling performances of the as-synthesized MoS_2 nanosheets and commercial MoS_2 powders were also demonstrated. In case of the MoS_2 nanosheets, the capacity increased significantly between the 5^{th} and 35^{th} cycles and then dramatically decreased to a level of only 650 mA h g^{-1} at the 90^{th} cycle. The phenomenon of initial capacity increase is probably related to the activation process that associates with more conductive pathways of the active material for Li-ion insertion in every subsequent cycle, and the unstable electrode/electrolyte interface leading to the reversible growth of polymer-like film due to electrolyte decomposition. For the commercial MoS_2 powders, the capacity started to drop significantly in the very beginning and faded out rapidly after around 50 cycles, retained less than 200 mA h g^{-1} after 120 cycles.

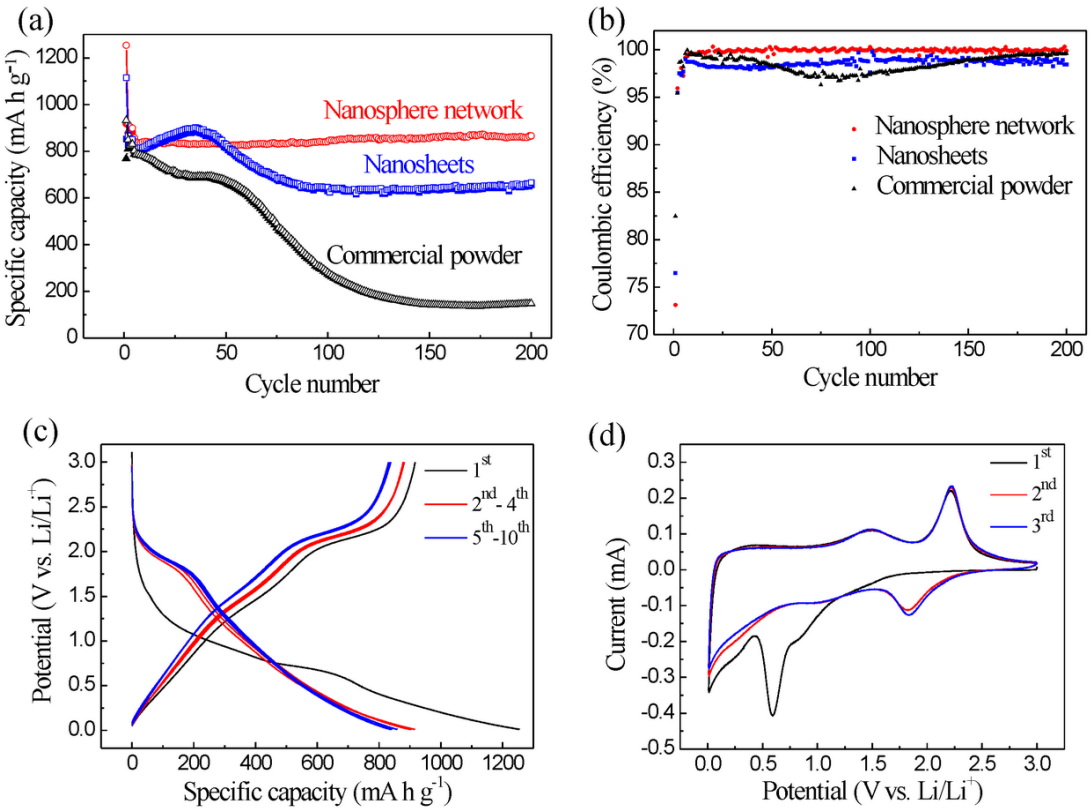

Figure 4.5 (a) Galvanostatic charge and discharge curves and (b) corresponding Coulombic efficiencies of MoS_2 nanosphere network, nanosheets and commercial powder under current density of 0.5 C. (c) Discharge-charge voltage profiles of the MoS_2 nanosphere network for the first 10 cycles. (d) CV scan of the MoS_2 nanosphere network for the first 3 cycles.

The corresponding Coulombic efficiencies of the MoS_2 samples are plotted in figure 4.5 (b). As compared to the initial Coulombic efficiencies of the MoS_2 nanosheets (76.5 %) and commercial MoS_2 powders (82.5 %), the MoS_2 nanosphere network shows a relatively low value of 73.1 %. This may due to the large surface area of the MoS_2 nanosphere network accelerating the electrolyte decomposition in

the first cycle. However, the Coulombic efficiency of the nanosphere network increased remarkably to 96 %, surpassing that of the nanosheets and commercial powders. Starting from the 6^{th} cycle, the nanosphere network attained more than 99 % Coulombic efficiency and even stayed at a level of over 99.8 % from the 20^{th} cycle. On the other hand, both the nanosheets and commercial powders exhibit relatively lower and unstable Coulombic efficiency. By comparing, the MoS_2 nanosphere network shows superior electrochemical performances in terms of cyclability, stability, reversibility and Coulombic efficiency over the MoS_2 nanosheets and commercial powders. Such superior electrochemical performances can be attributed to (1) the small size of the nanospheres (80 nm mean diameter) which provides relatively short Li-ion diffusion pathways; (2) the large surface area to volume ratio of the nanosphere network that is believed to enhance the electrochemical reactions between the Li-ions and MoS_2 nanospheres; (3) the interlinked nanosphere network which facilitates efficient electron transport and (4) the expanded interlayer separation in the (002) plane as well as the disordered layers of the MoS_2 nanospheres that provide fast conduction channels for Li-ion diffusion.

Figure 4.5 (c) shows the discharge-charge voltage profiles of the MoS_2 nanosphere network for the first 10 cycles in correspond to the galvanostatic measurements in figure 4.5 (a), whereas the 1^{st} cycle, 2^{nd} – 4^{th} cycles and 5^{th} – 10^{th}

cycles were respectively under current density of 0.1 C, 0.2 C and 0.5 C. The highly reversible discharge-charge voltage profiles suggest electrochemically stable of the nanosphere network. To further inspect the electrochemical reactions associated with the Li-ions and the MoS_2 nanosphere network, cyclic voltammetric (CV) measures were performed. Figure 4.5 (d) displays the first three CV scans of the nanosphere network. The overall CV behavior is generally in consistent with previous reports. In the first cathodic sweep, the small reduction peak at ~ 0.85 V is related to the Li-ion insertion kinectics which lead to the formation of Li_xMoS_2 ($MoS_2 + x\mathrm{Li}^+ + x\mathrm{e}^- \rightarrow \mathrm{Li}_x\mathrm{MoS}_2$), whereas the sharp reduction peak at ~ 0.6 V is attributed to the conversion reaction process in which the Li_xMoS_2 is electrochemically decomposed to Mo nanoparticles embedded in a Li_2S matrix ($\mathrm{Li}_x\mathrm{MoS}_2 + (4-x)\mathrm{Li}^+ + (4-x)\mathrm{e}^- \rightarrow \mathrm{Mo} + 2\mathrm{Li}_2\mathrm{S}$). In the subsequent two cycles, these two reduction peaks disappear due to amorphous MoS_2 formation after Li-ion extraction in the first cycle. On the other hand, two new reduction peaks at ~ 1.1 V and 1.8 V appears, suggesting a multi-step insertion/conversion mechanism in subsequent cycles. For the anodic sweeps, two oxidation peaks respectively appear at ~ 1.5 V and 2.2 V, corresponding to the Li-ion extraction process and the oxidation of Mo nanoparticles to amorphous MoS_2. The CV results verify highly reversible of the electrochemical reactions associated with Li-ion and the MoS_2 nanosphere network.

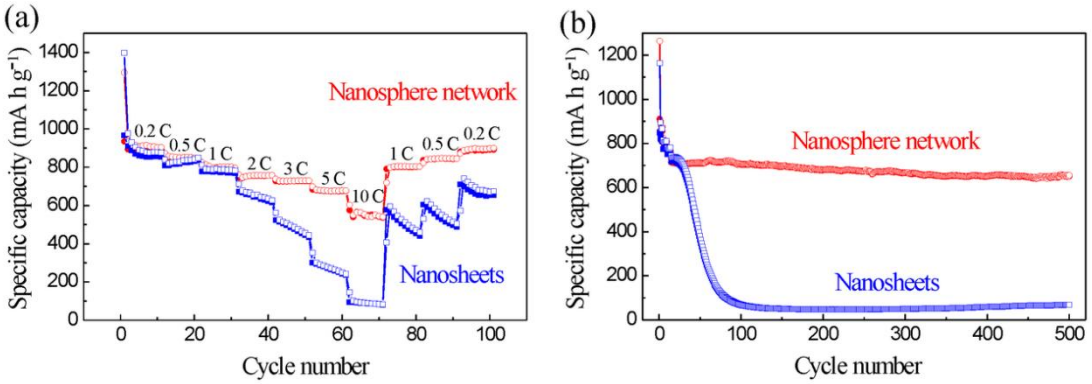

Figure 4.6 (a) Rate capabilities and (b) cycling performances (2C) of MoS_2 nanosphere network and MoS_2 nanosheets.

The unique structure of the MoS_2 nanosphere network realizes enhanced electrochemical performance of MoS_2-based lithium-ion battery with high reversible capacity, cycle stability and Coulombic efficiency. To further investigate its rate capability, the nanosphere network was cycled under various current densities. As shown in figure 4.6 (a), the MoS_2 nanosphere network exhibited excellent cycling performance in respond to high current densities up to 10 C (6.7 A g^{-1}). The specific charge capacity delivery at 0.2 C, 0.5 C, 1 C, 2C, 3 C, 5 C and 10 C were about 900 mA g^{-1}, 850 mA g^{-1}, 800 mA g^{-1}, 760 mA g^{-1}, 730 mA g^{-1}, 680 mA g^{-1} and 550 mA g^{-1}, respectively. In particular, after deep cycling for 70 cycles, the capacity was capable to recover to the same levels as previous measurements when returning back to lower current densities from 10 C. On the contrary, the MoS_2 nanosheets displayed less promising rate capability. Although the performance of the nanosheets is fairly comparable to that of the nanosphere network at low current density, their capacity

delivery dropped significantly beyond current density of 1 C, and retained less than 100 mA g^{-1} at 10 C. Moreover, the capacity of the nanosheets failed to recover to initial levels when returning back to lower current densities. The superior rate capacity of the MoS_2 nanosphere network can be attributed to its unique structure as aforementioned, with small nanosphere size, large surface area to volume ratio, electron conduction network and expanded interlayer separation. In order to examine the long-term cycling performance of the MoS_2 samples at higher current density, both the nanosheets and nanosphere network were cycled at 2 C (1.34 A g^{-1}), whereas the first 14 cycles underwent gradual increase of current density from 0.1 C to 1 C to slowly activate the electrochemical active materials. As shown in figure 4.6 (b), the MoS_2 nanosphere network exhibited remarkably stable long-term cycling performance at higher current density of 2 C over 500 cycles. The first charge capacity delivery at 2 C (15^{th} cycle) was 715 mA h g^{-1}. After 500 cycles, charge capacity of 651 mA h g^{-1} was still retained, corresponding to 91 % capacity retention. In contrast, the capacity of the MoS_2 nanosheets faded out drastically just after 30 cycles, and remained less than 100 mA g^{-1} after 100 cycles. The comparative results verify superior long-term cycling performance of the MoS_2 nanosphere network under higher current density.

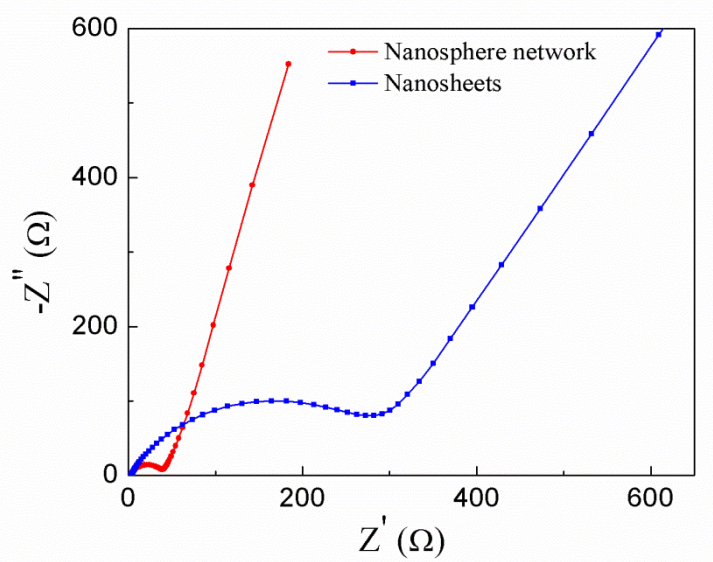

Figure 4.7 Nyquist plots of MoS_2 nanosphere network and MoS_2 nanosheets.

To evident the unique structure of MoS_2 nanosphere network for the enhancement of electron transport and Li-ion diffusion, electrochemical impedance spectroscopy (EIS) measurements were performed. Figure 4.7 shows the Nyquist plots of the MoS_2 nanosphere network and the nanosheets. The semicircle at high frequency region is related to the charge-transfer process, while the straight line at lower frequency region refers to the Warburg impedance in related to the Li-ion diffusion. It is obvious that the semicircle of the nanosphere network is much smaller than that of the nanosheets, indicating smaller charge-transfer resistance of the nanosphere network, which can be explained by the small size and interlinked network feature of the nanospheres that facilitate fast electron transport. At lower frequency, the MoS_2 nanosphere network shows a larger Warburg slope, as compared to the nanosheets. The larger Warburg slope indicates faster Li-ion diffusion, which

can be attributed to the small size of the MoS_2 nanospheres that shortening the Li-ion diffusion length, and the expanded interlayer separation that offering fast diffusion channels for Li-ions.

4.3.3 Hydrogen Evolution Reaction (HER)

MoS_2 has been recently studied and confirmed as an active electrocatalyst for HER by exposing the edge sites which are electrochemically active in contrast to the inactive basal plane. Recent literatures have shown that by expanding the interlayer distance of MoS_2, the edge sites can be exposed and the HER performance based on that kind of MoS_2 can be significantly enhanced. In this experiment, MoS_2 nanospheres were successfully synthesized with expanded interlayer distance and randomly oriented layers. The MoS_2 nanospheres were applied as electrocatalysts for hydrogen evolution reaction (HER). Figure 4.8 shows the electrochemical measurements of MoS_2 nanospheres and MoS_2 nanosheets for HER. Both the MoS_2 nanostructures showed similar onset overpotential of 0.2 V for HER. However, the cathodic current density of the MoS_2 nanospheres is significantly larger than that of the MoS_2 nanosheets beyond 0.2V. Since the cathodic current density is proportional to the amount of hydrogen evolved, the MoS_2 nanospheres show superior HER behavior over the nanosheets. The enhanced HER activity of MoS_2 nanospheres can

be attributed to the exposed edge sites resulting from enlargement of interlayer distance.

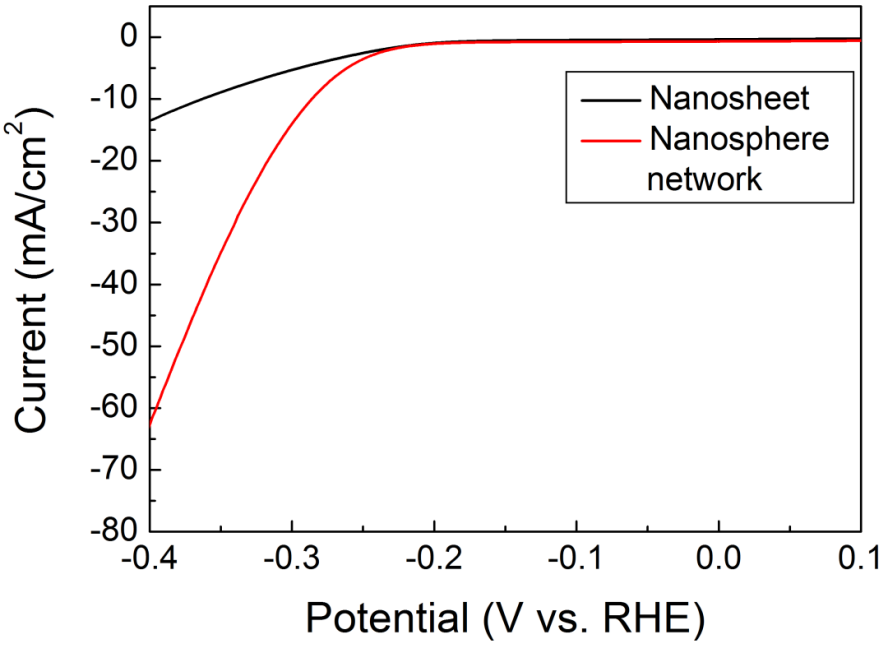

Figure 4.8 Electrochemical measurements of MoS_2 nanosphere network and MoS_2 nanosheets for hydrogen evolution reaction (HER).

4.4 Conclusion

MoS_2 nanosphere network was synthesized by facile PVP-assisted hydrothermal reaction. The size of the nanospheres decreased with increasing the PVP concentration. 80 nm MoS_2 nanospheres can be obtained when 0.5 g PVP were added in the synthesis. The nanospheres interlinked to each other forming a network. The MoS_2 nanosphere network was applied as LIB anode and showed enhanced electrochemical performance. The electrochemical enhancement can be attributed to (1) the small size of the nanospheres which provided relatively short Li-ion diffusion pathways; (2) the

large surface area to volume ratio of the nanosphere network that is believed to enhance the electrochemical reactions between the Li-ions and MoS_2 nanospheres; (3) the interlinked nanosphere network which facilitated efficient electron transport and (4) the expanded interlayer separation in the (002) plane as well as the disordered layers of the MoS_2 nanospheres that provided fast conduction channels for Li-ion diffusion. On the other hand, the MoS_2 nanosphere network showed improved electrocatalytic activity for HER. The improved electrochemical performance can be attributed to the expanded interlayer distance of the MoS_2 resulting in the expose of active edge sites for electrochemical reactions.

4.5 References

[1] J. M. Tarascon, M. Armand. Nature, 2001, 414, 359-367.

[2] K. Kang, Y. S. Meng, J. Breger, C. P. Grey, G. Ceder. Science, 2006, 311, 977-980.

[3] C. J. Wen, R. A. Huggins. *J. Solid State Chem.*, **1981**, 37, 271-278.

[4] C. K. Chan, R. Ruffo, S. S. Hong, R. A. Huggins, Y. Cui. *J. Power Sources*, **2009**, 189, 34-39.

[5] B. A. Boukamp, G. C. Lesh, R. A. Huggins. *J. Electrochem. Soc.*, **1981**, 128, 725.

[6] M. T. McDowell, I. Ryu, S. W. Lee, C. M. Wang, W. D. Nix, Y. Cui. *Adv. Mater.*, **2012**, 24, 6034-6041.

[7] H. Wu, G. Chan, J. W. Choi, I. Ryu, Y. Yao, M. T. McDowell, S. W. Lee, A. Jackson, Y. Yang, L. B. Hu, Y. Cui. *Nature Nanotechnology*, **2012**, 7, 310-315.

[8] T. H. Hwang, Y. M. Lee, B. S. Kong, J. S. Seo, J. W. Choi. *Nano Lett.*, **2012**, 12, 802-807.

[9] H. Wu, G. Y. Zheng, N. Liu, T. J. Carney, Y. Yang, Y. Cui. *Nano Lett.*, **2012**, 12, 904-909.

[10] N. Liu, H. Wu, M. T. McDowell, Y. Yao, C. M. Wang, Y. Cui. *Nano Lett.*, **2012**, 12, 3315-3321.

[11] K. F. Mak, C. Lee, J. Hone, J. Shan, T. F. Heinz. *Physical Review Letters*, **2010**, 205, 136805.

[12] B. Radisavljevic, A. Radenovic, J. Brivio, V. Giacometti, A. Kis. *Nature Nanotechnology*, **2011**, 6, 147-150.

[13] Q. H. Zhang, K. Kalantar-Zadeh, A. Kis, J. N. Coleman, M. S. Strano. *Nature Nanotechnology*, **2012**, 7, 699-712.

[14] T. L. Mogne, C. Donnet, J. M. Martin, A. Tonck, N. Millard-Pinard. *J. Vac. Sci. Technol., A,* **1994**, 12(4), 1998-2004.

[15] H. W. Wang, P. Skeldon, G. E. Thompson. *Surf. Coat. Technol.*, **1997**, 91, 200-207.

[16] H. Li, Z. Y. Yin, Q. Y. He, X. Huang, G. Lu, D. W. H. Fam, A. I. Y. Tok, Q.

Zhang, H. Zhang. *Small*, **2012**, 8, 63-67.

[17] W. Han, P. Yuan, Y. Fan, G. Shi, H. Liu, D. Bai, X. Bao. *J. Mater. Chem.*, **2012**, 22, 25340-25343.

[18] J. Xie, H. Zhang, S. Li, R. Wang, X. Sun, M. Zhou, J. Zhou, X. W. (David) Lou, Y. Xie. *Adv. Mater.*, **2013**, 25, 5807-5813.

[19] D. Y. Chung, S-K. Park, Y-H. Chung, S-H. Yu, D-H. Lim, N. Jung, H. C. Ham, H-Y. Park, Y. Piao, S. J. Yoo, Y-E. Sung. *Nanoscale*, **2014**, 6, 2131-2136.

[20] S. Ding, D. Zhang, J. S. Chen, X. W. (David) Lou. *Nanoscale*, **2012**, 4, 95-98.

[21] S-K. Park, S-H. Yu, S. Woo, J. Ha, J. Shin, Y-E. Sung, Y. Piao. *CrystEngComm.*, **2012**, 14, 8323-8325.

[22] S. Liang, J. Zhou, J. Liu, A. Pan, Y. Tang, T. Chen, G. Fang. *CrystEngComm.*, **2013**, 15, 4998-5002.

[23] H. Hwang, H. Kim, J. Cho. *Nano Lett.*, **2011**, 11, 4826-4830.

[24] P-P. Wang, H. Sun, Y. Ji, W. Li, X. Wang. *Adv. Mater.*, **2014**, 26, 964-969.

[25] C. Zhang, H. B. Wu, Z. Guo, X. W. (David) Lou. *Electrochemistry Comm.*, **2012**, 20, 7-10.

[26] K. Chang. W. Chen. *Chem. Commun.*, **2011**, 47, 4252-4254.

[27] K. Chang, W. Chen. *ACS Nano*, **2011**, 5, 4720-4728.

[28] S. K. Das, R. Mallavajula, N. Jayaprakash, L. A. Archer. *J. Mater. Chem.*, **2012**,

22, 12988-12992.

[29] Y-T. Liu, X-D. Zhu, Z-Q. Duan, X-M. Xie. *Chem. Commun.*, **2013**, 49, 10305-10307.

[30] X. Zhou, L-J. Wan, Y-G. Guo. *Chem. Commun.*, **2013**, 49, 1838-1840.

Chapter 5 Three-dimensional Porous Copper Supported Silicon as High Performance Lithium-ion Battery Anodes

5.1 Introduction

Lithium-ion batteries (LIBs) are integral to nowaday's information-rich society for powering most types of portable electronics. Substantial efforts have been devoted to the development of LIBs with higher capacity, longer cycle life and higher rate capability for future advanced electrical applications.[1] With the highest theoretical capacity (4200 mAh g^{-1}) and relative low discharge potential (< 0.5 V vs. Li^+/Li),[2,3] Si has attracted particular research interest with the attempt to replace commercially used graphite, which has a low theoretical specific capacity of only 372 mAh g^{-1}, as a new generation LIB anode material.[4] Nevertheless, the practical implementation of Si-based anode is impeded by the well-known enormous volume variation (up to 400%) of Si upon Li-Si interactions,[5,6] which generally results in pulverization and eventually electrical disconnection of the Si active material from the current collector.[3] To overcome this issue, proper empty space engineering is essential for the accommodation of huge volume changes during Si alloying and de-alloying with lithium, which allows facile strain relaxation of Si and thus the structural integrity and electrical pathway can be well preserved. To realize this engineering approach, Si nanowires[7] and nanotubes[8] have been fabricated directly on current collectors,

which were reported to possess enhanced cycling performance. However, the small contact area between Si nanowires (or nanotubes) and the current collector would experience strong shear stress upon Li-Si alloying and de-alloying processes, probably resulting in the disconnection of Si nanostructure from the current collector. Alternatively, hybrid carbon-Si core-shell[9-11] and metal-Si core-shell[12-16] nanostructures can circumvent such shortcoming by providing large adhesion surface for Si. Other Si nanostructures such as porous Si,[17,18] carbon coated Si nanotubes,[19] Si nanotubes with mechanical clamping shell,[20] Si nanoparticles encapsulated in carbon nanotubes[21,22] and Si-C yolk-shell design[23] also show promising performance as LIB anodes.

Among all the proposed Si-based anodes, 3D scaffold supported Si architectures show a relatively simple and direct approach for empty space engineering. The 3D scaffold can offer space for Si volume changes during cycling and impart both structural and electrical support to Si, as well as providing large surface area for Si loading and facilitating fast Li-Si reactions. Inverse-opal-based 3D carbon scaffold supported Si anode was first proposed by Ozin's group,[24] which exhibited improved cycling performance and rate capability. However, it is preferable to use electrochemical inactive materials as the scaffold in order to maximize both the mechanical stability and electrical conductivity.[25] Later on, Tu's group introduced 3D

porous nano-Ni supported Si film as high-performance LIB anodes.[26] Recently, 3D inverse-opal Ni scaffold supported bicontinuous Si anodes were synthesized by Braun *et al.*[25] and displayed fairly good performance, but their long cycle life especially under high current density have not been demonstrated.

Herein, we report a 3D porous Cu supported Si (hereafter abbreviated as 3D pCu-Si) nanostructure as anode for LIBs, which demonstrates enhanced electrochemical performance in terms of cycle life and rate capability. The electrochemical inactive 3D porous Cu skeleton directly grown on Cu foil acts as a nanoporous current collector and renders both structural support and electrical pathway to the Si active material. Large surface area of the porous nanostructure is beneficial to hold more active materials and facilitate electron transport. Furthermore, the robust porous Cu skeleton offers sufficient empty spaces to accommodate large volume changes of Si during charge and discharge processes, which helps to alleviate strain-induced mechanical rupture of the Si active material.

5.2 Experimental Section

5.2.1 Preparation of Polystyrene Sphere Template

Cu foils were punched to disks (diameter: 9/16 inches) and cleaned with dilute HCl to remove any surface oxides prior to use. Polystyrene (PS) sphere solution

(Bangs Laboratories, 610 nm, 10% concentration) was diluted by ethanol with a volume ratio of 1:5. 20 μL of the diluted PS sphere solution was dispersed dropwise and spread evenly onto the Cu foil surface, followed by drying at 50 ^{o}C for 5 minutes. The PS spheres randomly self-assembled through capillary action of liquid during the drying process, resulting in about three compact PS sphere layers on the Cu foil surface.

5.2.2 PS Sphere Template Assisted Growth of 3D Porous Cu Skeleton

Cathodic electrodeposition was performed to fill the voids between PS spheres with Cu. The electrodeposition of Cu was conducted in a three-electrode configuration on an IM6 electrochemical workstation (ZAHNER elektrik). The electrolyte was 50 g L^{-1} $CuSO_4 \cdot 5H_2O$ (Sigma Aldrich, ACS reagent, ≥98%) solution. The as-prepared Cu foil covered with PS sphere template was used as the working electrode, while the counter electrode was Pt plate and the reference electrode was Ag/AgCl. Electrodeposition of Cu was carried out under constant potential of -0.4 V for 2 minutes. 3D porous Cu skeleton can then be obtained through simple removal of the PS sphere template with chloroform.

5.2.3 Deposition of Si Nano thin Film on 3D Porous Cu Skeleton and Half-cell Assembly

Si was deposited on the 3D porous Cu skeleton in an Ar-filled chamber by

radio-frequency (RF) sputtering of a Si target (SCI Engineered Materials, Si P-type) at 50 W under working pressure of 2 mTorr for 30 minutes. The as-prepared 3D pCu-Si nanostructures were directly used as LIB anodes without further treatments. Half-cells were assembled in an Ar-filled MBraun glovebox (with both H_2O and O_2 contents less than 0.1 ppm) using Li foil as the counter electrode and 1.2 M $LiPF_6$ in ethylene carbonate (EC) and ethylene methyl carbonate (EMC) (3:7 by weight) as the electrolyte.

5.2.4 Characterization and Electrochemical Measurements

The morphologies of the samples were examined by SEM (Philips). EDX analysis was performed using EDAX system attached to the SEM. The nature of the sputtered Si was characterized by XRD (Philips X'Pert X-ray diffractometer) and Raman spectroscopy (Renishaw, 633nm laser). Cyclic voltammetric (CV) scans were conducted on a CHI 600D electrochemical workstation in a potential window of 0.01-2.7 V at a scan rate of 0.1 mV s^{-1}. Electrochemical properties were characterized at room temperature using a battery test system (MACCOR 4000) in a potential range of 0.01-1 V. The specific capacity and charge/discharge current density were calculated based on the weight of Si in the electrode. After cycling, the batteries were disassembled in the Ar-filled MBraun glovebox. Prior to SEM characterization, the disassembled Si electrodes were cleaned with acetone and ethanol thoroughly to

remove any remaining electrolyte and salts.

5.3 Results and Discussion

5.3.1 Morphological and Elemental Characterizations

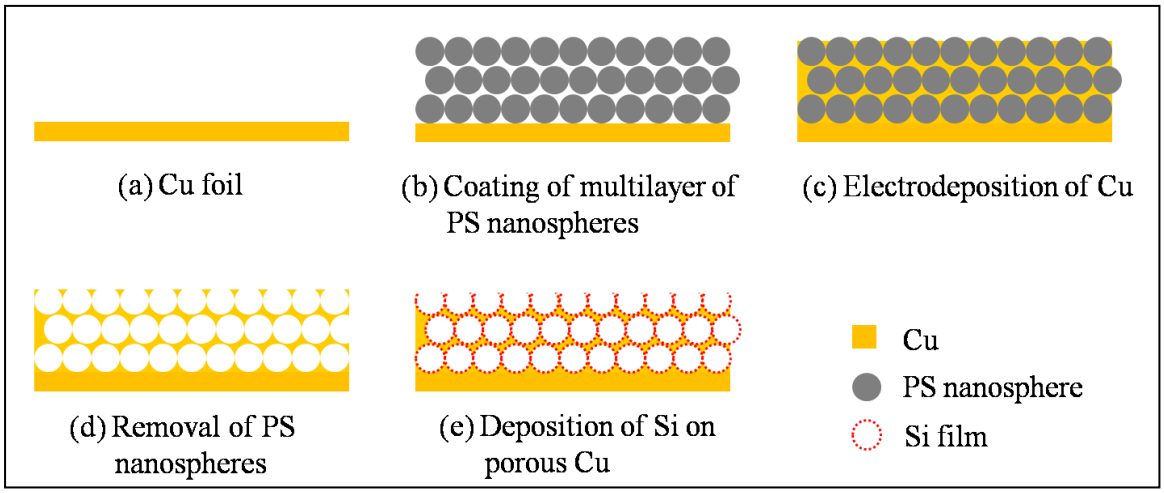

Figure 5.1 Schematic illustration of the fabrication processes of the 3D pCu-Si nanostructure.

The fabrication procedure for the 3D pCu-Si nanostructure is schematically illustrated in figure 5.1. Representative SEM image of the as-fabricated 3D porous Cu skeleton is shown in figure 5.2 (a). It is obvious that the morphology of the 3D porous Cu skeleton has a random inverse opal structure with large porosity which can provide extended surface area to hold Si electro-active material. The average pore size is about 580 nm in diameter, very close to the average size of the PS spheres (610 nm). Figure 5.2 (b) shows the SEM image of the sample right after RF sputtering of Si on the 3D porous Cu skeleton. The as-sputtered material is confirmed to be Si by EDX

(figure 5.2 (c)). The occurrence of little trace of oxygen may be due to unavoidable oxidation of the Si surface during transferring the sample. It is worthy to note that after the deposition of Si active material, the 3D porous morphology of the nanostructure is still retained. The retained pores provide empty space to accommodate Si volume changes upon Li-Si interactions, hence allow facile strain relaxation of the Si active material. The pore size is reduced to an average diameter of about 350 nm after Si deposition. By comparing the pore size before and after Si deposition, it can be deduced that the thickness of the as-deposited Si film is about 115 nm. The nature of the as-deposited Si was characterized by XRD. The XRD pattern shown in figure 5.2 (d) only displays the characteristic peaks of Cu. The absence of typical crystalline Si peaks indicates amorphous nature of the as-deposited Si.[26-28] The amorphous nature of the Si was further confirmed by Raman spectroscopy (figure 5.2 (e)), where the broad peak centered at about 480 cm^{-1} relevant to amorphous Si is observable.[26,29,30] It was reported previously that, as compared to crystalline Si, amorphous Si is more beneficial for LIB application because of its less volume changes upon Li-Si interaction, as well as its better adhesion with the current collector, which can accommodate more strain and better withstand pulverization.[31-33]

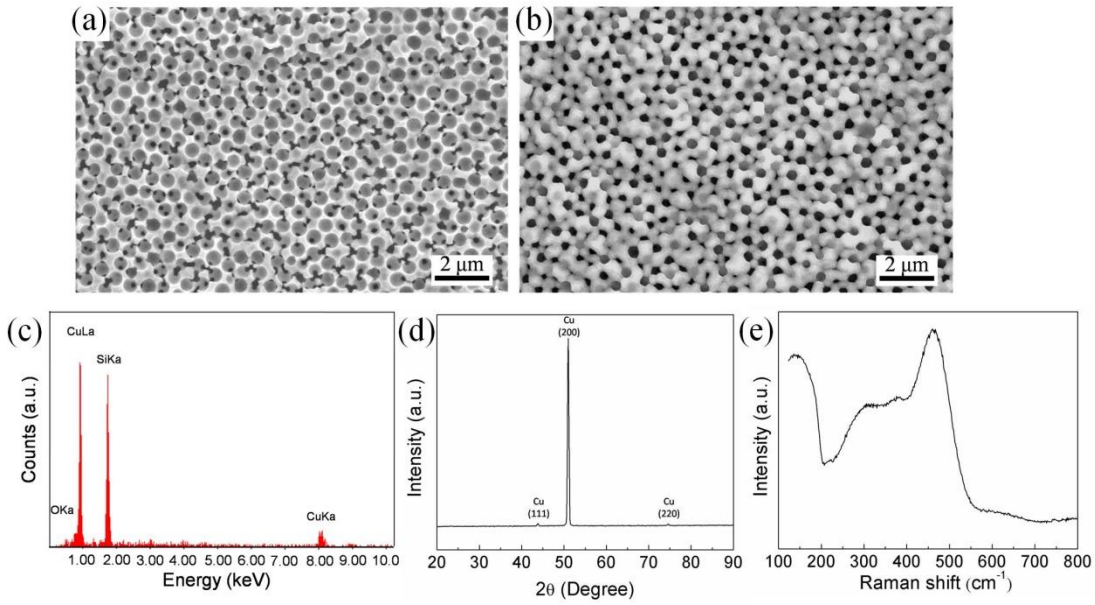

Figure 5.2 SEM image of (a) the 3D porous Cu skeleton, and (b) the 3D pCu-Si nanostructure after the deposition of Si. (c) EDX spectrum (d) XRD pattern and (e) Raman spectrum of the 3D pCu-Si nanostructure.

5.3.2 Electrochemical Properties

The electrochemical performance of the 3D pCu-Si anode was first characterized by cyclic voltammetry (CV). Figure 5.3 (a) shows the CV curves of the 3D pCu-Si anode in a potential window of 0.01-2.7 V (vs. Li^+/Li) at a scan rate of 0.1 mV s^{-1} for the first ten cycles. For the first cathodic scan, there is a broad peak in the potential range of 0.5-2.7 V, which disappeared in subsequent cycles. This peak can be ascribed to the solid-electrolyte interface (SEI) formation as a result of electro-decomposition of the electrolyte on the Si surface in the first cycle.[34,35] The Li-ion insertion process began to go fast from around 0.25 V. Cathodic peak at 0.01 V represents the formation

of a Li-Si alloy phase.[3] In the subsequent cathodic scans, an additional cathodic peak at 0.2 V appeared which can be attributed to the formation of another amorphous Li-Si alloy phase.[3,26] In the case of the first anodic scan, only one peak centered at 0.59 V is observable. This peak shifted to a lower potential of 0.52 V in the second anodic scan and eventually splitted into two peaks at around 0.38 V and 0.51 V in subsequent cycles. These two peaks refer to the de-alloying of the Li-Si alloy phases. [3,16,26] Starting from the 4^{th} cycle, the shape of the CVs do not change significantly. The CV results are consistence with that previously reported for Si-based LIB anodes. [16,26] The highly repeatability of the CV shape suggests good reversibility of the Li-Si alloying/de-alloying reactions.

Galvanostatic charge and discharge test was carried out to check the cycling performance of the 3D pCu-Si nanostructure. The half-cell was cycled in a potential window of 0.01-1 V (vs. Li^+/Li) under a current density of 1.4 A g^{-1} (a smaller current density of 0.42 A g^{-1} was applied in the first cycle and 0.84 A g^{-1} in the latter two cycles in the attempt to slowly activate the Si active material in the early cycling stage). Figure 5.3 (b) displays the capacity and Coulombic efficiencies of the 3D pCu-Si anode versus cycle number. The first discharge and charge capacities are 2711 mAh g^{-1} and 2170 mAh g^{-1}, respectively, resulting in an initial Coulombic efficiency of 80%. The 20% initial capacity loss can be ascribed to the SEI formation and the

irreversible Li-Si alloying in the first discharge process.[3] The efficiency increases to 95.8% in the second cycle and even stays above 99% after the third cycle, suggesting that our 3D pCu-Si anode is electrochemically stable. As referred to the cycling capacity curve, the capacity drastically drops to about 1500 mAh g^{-1} in the 7^{th} cycle and gradually recovers to the level of 2400 mAh g^{-1} in the 50^{th} cycle. Such an initial drop and then rise of capacity was also reported in previous literatures.[13,20,26,36]The reason for this phenomenon is unclear so far but it may be due to the activation of additional Si active material to react with Li ions in initial cycles. From the 50^{th} cycle onwards, the cycling behavior is quite stable. The reversible discharge capacity attains up to 2505 mAh g^{-1} in the 81^{st} cycle. At the end of the 400^{th} cycle, the reversible discharge capacity is still as high as 2013 mAh g^{-1} with a capacity retention of 80.3%, or 99.9% per cycle. For a comparison, the cycling performance of Si directly deposited on pure Cu foil (with the same deposition conditions as for the 3D porous Cu skeleton) was also tested under the same current density. The capacity dramatically declines within the first 30 cycles and a discharge capacity of only 40 mAh g^{-1} is retained after 50 cycles. On the contrary, 3D pCu-Si nanostructure remarkably exhibits excellent cycling performance in terms of charge/discharge reversibility and cycle life. Figure 5.3 (c) shows the galvanostatic charge and discharge profiles of the 3D pCu-Si anode at different cycle numbers. The shapes of

the profiles do not show noticeable changes, revealing high reversibility of the Li-Si alloying reactions, which is consistent with the CV result.

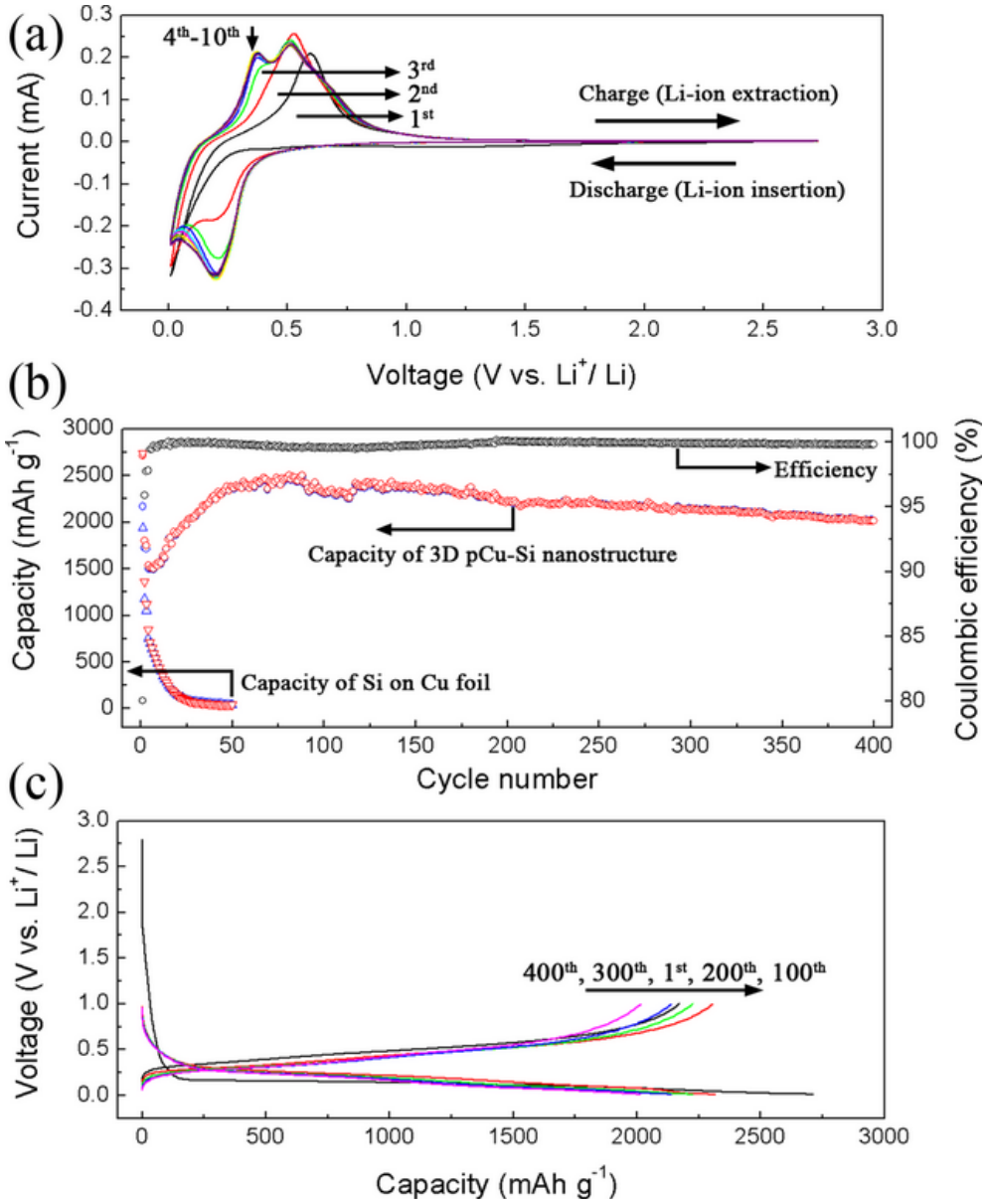

Figure 5.3 (a) CV curves of the 3D pCu-Si anode from the 1st to 10th cycle. (b) Cycling performance of the 3D pCu-Si anode and the Cu foil supported Si anode under current density of 1.4 A g^{-1} (C/3). (c) Galvanostatic discharge-charge profiles of the 3D pCu-Si anode at different cycles.

5.3.3 Morphology of Anode after Cycling

After 400 cycles, the cell was disassembled and the morphology of the cycled 3D pCu-Si nanostructure was characterized by SEM. As shown in figure 5.4 (a), the Si nanostructure cracked into small islands with several microns in size after severe charge and discharge processes. Nevertheless, the Si within each island remains intact and attached to the porous Cu skeleton, therefore the electrical pathway of Si is still well preserved. The porous Cu skeleton plays an important role to impart mechanical support to the Si active material and hence prevents peeling off of the Si from the current collector. As a reference, the Si directly deposited on Cu foil was also characterized by SEM after only 50 cycles. Figure 5.4 (b) shows that the Si film suffered from severe pulverization. The warping of the Si leads to its electrical disconnection from the Cu substrate and consequently causes rapid capacity fading of the electrode. These morphological characterization results prove that the excellent cycling performance of our 3D pCu-Si anode can be ascribed to the 3D porous Cu skeleton which renders both mechanical reinforcement and electrical pathway to the Si active material. Moreover, the engineered empty space provided by the 3D porous Cu skeleton allows facile accommodation of Si volume variation, which helps to alleviate severe pulverization of Si upon Li-Si interactions.

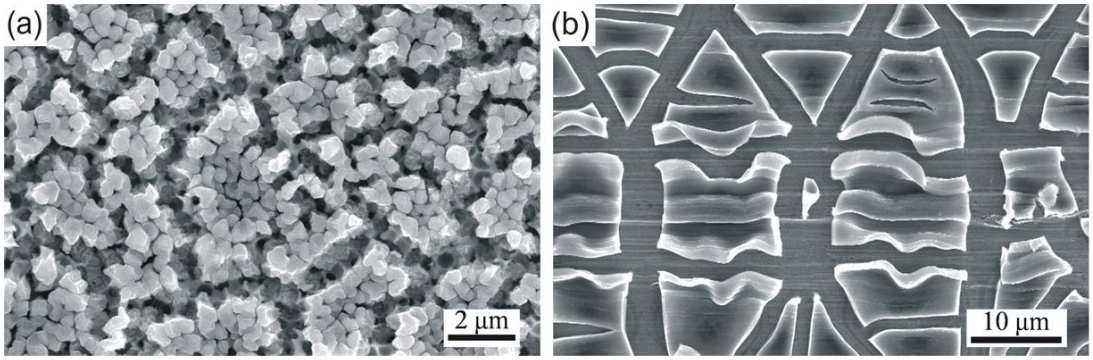

Figure 5.4 SEM images of (a) the 3D pCu-Si anode after 400 cycles, and (b) the Cu foil supported Si after 50 cycles.

5.3.4 Rate Capability and Long-term Cycling under Higher Current Density of 12.6 A g^{-1} (3C)

To determine the rate capability of our 3D pCu-Si anode, another half-cell was cycled under a series of current densities. As shown in figure 5.5 (a), the anode exhibited high rate capabilities at a current density range up to 16.8 A g^{-1} (4C). The average discharge capacity is 2937 mAh g^{-1} at 0.42 A g^{-1} (C/10), 2556 mAh g^{-1} at 0.84 A g^{-1} (C/5), 2006 mAh g^{-1} at 2.1 A g^{-1} (C/2), 1643 mAh g^{-1} at 4.2 A g^{-1} (1C), 1289 mAh g^{-1} at 8.4 A g^{-1} (2C) and 898 mAh g^{-1} at 16.8 A g^{-1} (4C). When the current density was changed from 16.8 A g^{-1} back to 0.42 A g^{-1}, the discharge capacity of the cell recovered to 2800 mAh g^{-1}. The high capacity deliveries under different current densities, together with the excellent capacity recovery verify high rate capability of our 3D pCu-Si nanostructure. Such a remarkable rate performance can be attributed to

the 3D pCu-Si architecture which provides large surface area for facile Li-Si reaction and also facilitates electron transport in the system.

The 3D pCu-Si anode was further examined for its cycling performance under higher current density. Figure 5.5 (b) illustrates the cycling performance of the 3D pCu-Si anode under current density of 12.6 A g^{-1} (3C) in a potential window of 0.01-1 V (vs. Li^+/ Li). Current densities of 0.42 A g^{-1} and 0.84 A g^{-1} were applied in the 1^{st} cycle and 2^{nd}-6^{th} cycles, respectively. The initial cycle delivered a discharge capacity of 2667 mAh g^{-1}. When the current density was changed from 0.84 A g^{-1} to 12.6 A g^{-1} in the 7^{th} cycle, the discharge capacity significantly dropped to only 640 mAh g^{-1} and even 450 mAh g^{-1} in the 21^{st} cycle. However, the discharge capacity gradually recovered and attained the highest reversible discharge capacity of 1463 mAh g^{-1} in the 234^{th} cycle. After 1000 cycles, the discharge capacity was 1218 mAh g^{-1}, with a high capacity retention of 83.3%. Even at the end of the 2000^{th} cycle, a discharge capacity of 955 mAh g^{-1} was still retained, which is 2.6 times higher than the theoretical capacity of graphite (372 mAh g^{-1}). The initial Coulombic efficiency is 82.9% and it stays above 99% from the 11^{th} cycle onwards, suggesting high electrochemical stability of our 3D pCu-Si anode under high current density of 12.6 A g^{-1}. Recently, Wang *et al.* has reported similar porous Cu-Si nanostructure for Li-ion battery with improved electrochemical performance under current density of 4.2 A g^{-1}

(1C) and 8.4 A g^{-1} (2C).[37] However, the Coulombic efficiency of our batteries is better than theirs. In addition, rate capability and long-term cycling of battery have not been demonstrated in their work. The impressive long-term cycling performance of our 3D pCu-Si anode under high current density makes it promising for high-rate LIB, which is desired in nowaday's portable electronic industry.

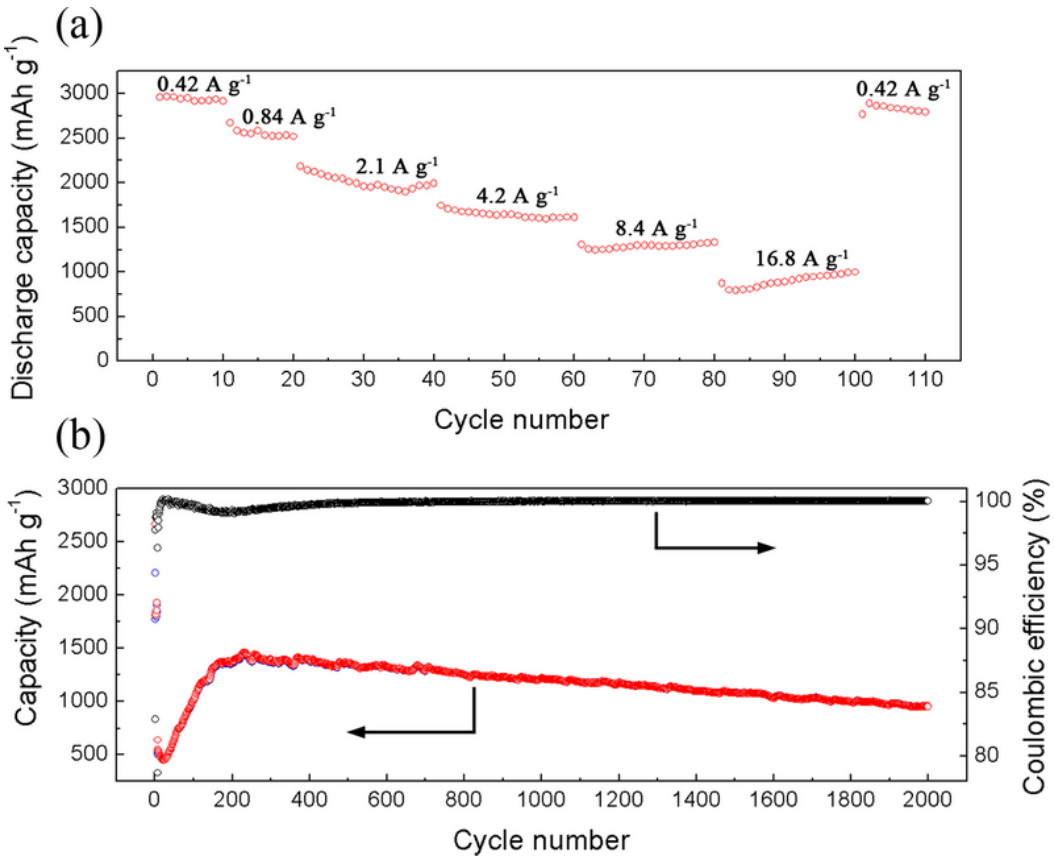

Figure 5.5 (a) Rate capability of the 3D pCu-Si anode. (b) Cycling performance of the 3D pCu-Si anode under current density of 12.6 A g^{-1} (3C) for 2000 cycles.

5.4 Conclusion

In summary, we have successfully fabricated 3D porous Cu supported Si (3D pCu-Si) nanostructure as LIB anode based on an empty space engineering approach.

The 3D pCu-Si anode delivered a reversible capacity as high as 2505 mAh g^{-1} under current density of 1.4 A g^{-1} (C/3), with an average Coulombic efficiency of more than 99% and capacity retention of 80.3% after 400 cycles. The 3D pCu-Si anode also exhibited high rate capability up to current density of 16.8 A g^{-1} (4C) and impressive cycling performance under high current density of 12.6 A g^{-1} (3C) for 2000 cycles. The excellent cyclability and high rate capability of our 3D pCu-Si anodes can be attributed to the novel empty-space design of which the 3D porous Cu skeleton allows facile accommodation of Si volume variation during Li-Si interactions, as well as imparting both structural support and electrical pathway to the Si active material. The 3D porous Cu nanostructure is also promising to be excellent current collector for other electro-active materials that experience significant volume changes upon charge and discharge processes (e.g. Ge and Sn).

5.5 References

[1] R. Teki, M. K. Datta, R. Krishnan, T. C. Parker, T. M. Lu, P. N. Kumta, N. Koratkar. *Small*, **2009**, 5, 2236-2242.

[2] C. J. Wen, R. A. Huggins. *J. Solid State Chem.*, **1981**, 37, 271-278.

[3] C. K. Chan, R. Ruffo, S. S. Hong, R. A. Huggins, Y. Cui. *J. Power Sources*, **2009**, 189, 34-39.

[4] X. Zhou, Y. X. Yin, L. J. Wan, Y. G. Guo. *Adv. Energy Mater.*, **2012**, 2, 1086-1090.

[5] B. A. Boukamp, G. C. Lesh, R. A. Huggins. *J. Electrochem. Soc.*, **1981**, 128, 725.

[6] M. T. McDowell, I. Ryu, S. W. Lee, C. M. Wang, W. D. Nix, Y. Cui. *Adv. Mater.*, **2012**, 24, 6034-6041.

[7] C. K. Chan, H. Peng, G. Lin, K. Mcllwrath, X. F. Zhang, R. A. Huggins, Y. Cui. *Nat. Nanotechnol.*, **2008**, 3, 31-35.

[8] T. Song, J. L. Xia, J. H. Lee, D. H. Lee, M. S. Kwon, J. M. Choi, J. Wu, S. K. Doo, H. Chang, W. I. Park, D. S. Zang, H. Kim, Y. G. Huang, K. C. Hwang, J. A. Rogers, U. Paik. *Nano Lett.*, **2010**, 10, 1710-1716.

[9] L. F. Cui, Y. Yang, C. M. Hsu, Y. Cui. *Nano Lett.*, **2009**, 9, 3370-3374.

[10] L. B. Hu, H. Wu, Y. F. Gao, A. Y. Cao, H. B. Li, J. McDough, X. Xie, M. Zhou, Y. Cui. *Adv. Energy Mater.*, **2011**, 1, 523-527.

[11] W. Wang, P. N. Kumta. *ACS Nano*, **2010**, 4, 2233-2241.

[12] X. L. Chen, K. Gerasopoulos, J. C. Guo, A. Brown, C. S. Wang, R. Ghodssi, J. N. Culver. *ACS Nano*, **2010**, 4, 5366-5372.

[13] F. F. Guo, J. W. Deng, S. Xin, H. X. Ji, O. G. Schmidt, L. J. Wan, Y. G. Guo. *Adv. Mater.*, **2011**, 23, 4415-4420.

[14] J. Qu, H. Q. Li, J. J. Henry, S. K. Martha, N. J. Dudney, H. B. Xu, M. F. Chi, M. J. Lance, S. M. Mahurin, T. M. Besmann, S. Dai. *J. Power Sources*, **2012**, 198, 312-317.

[15] X. L. Chen, K. Gerasopoulos, J. C. Guo, A. Brown, C. S. Wang, R. Ghodssi, J. N. Culver. *Adv. Funct. Mater.*, **2011**, 21, 380-387.

[16] S. C. Zhang, Z. J. Du, R. X. Lin, T. Jiang, G. R. Liu, X. M. Wu, D. S. Weng. *Adv. Mater.*, **2010**, 22, 5378-5382.

[17] Y. M. Liu, B. L. Chen, F. Cao, H. L. W. Chan, X. Z. Zhao, J. K. Yuan. *J. Mater. Chem.*, **2011**, 21, 17083-17086.

[18] Y. Zhao, X. Z. Liu, H. Q. Li, T. Y. Zhai, H. S. Zhou. *Chem. Commun.*, **2012**, 48, 5079-5081.

[19] J. K. Yoo, J. Kim, Y. S. Jung, K. Kang. *Adv. Mater.*, **2012**, 24, 5452-5456.

[20] H. Wu, G. Chan, J. W. Choi, I. Ryu, Y. Yao, M. T. McDowell, S. W. Lee, A. Jackson, Y. Yang, L. B. Hu, Y. Cui. *Nature Nanotechnology*, **2012**, 7, 310-315.

[21] T. H. Hwang, Y. M. Lee, B. S. Kong, J. S. Seo, J. W. Choi. *Nano Lett.*, **2012**, 12, 802-807.

[22] H. Wu, G. Y. Zheng, N. Liu, T. J. Carney, Y. Yang, Y. Cui. *Nano Lett.*, **2012**, 12, 904-909.

[23] N. Liu, H. Wu, M. T. McDowell, Y. Yao, C. M. Wang, Y. Cui. *Nano Lett.*, **2012**, 12, 3315-3321.

[24] A. Esmanski, G. A. Ozin. *Adv. Funct. Mater.*, **2009**, 19, 1999-2010.

[25] H. G. Zhang, P. V. Braun. *Nano Lett.*, **2012**, 12, 2778-2783.

[26] Y. Q. Zhang, X. H. Xia, X. L. Wang, Y. J. Mai, S. J. Shi, Y. Y. Tang, C. G. Gu, J. P. Tu. *J. Power Sources*, **2012**, 213, 106-111.

[27] Z. Edfouf, F. Cuevas, M. Latroche, C. Georges, C. Jordy, T. Hezeque, G. Gaillion, J. C. Jumas, M. T. Sougrati. *J. Power Sources*, **2011**, 196, 4762-4768.

[28] Y. X. Yin, S. Xin, L. J. Wan, C. J. Li, Y. G. Guo. *J. Phys. Chem. C*, **2011**, 115, 14148-14154.

[29] K. L. Lee, J. Y. Jung, S. W. Lee, H. S. Moon, J. W. Park. *J. Power Sources*, **2004**, 129, 270-274.

[30] M. K. Datta, J. Maranchi, S. J. Chung, R. Epur, K. Kadakia, P. Jampani, P. N. Kumta. *Electrochim. Acta*, **2011**, 56, 4717-4723.

[31] J. Nanda, M. Datta, J. T. Remillard, A. O'Neill, P. N. Kumta. *Electrochem. Commun.*, **2009**, 11, 235-237.

[32] C. S. Wang, G. T. Wu, X. B. Zhang, Z. F. Qi, W. Z. J. Li. *Electrochem. Soc.*, **1998**, 145, 2751-2758.

[33] M. T. McDowell, A. M. Leach, K. Gall. *Nano Lett.*, **2008**, 8, 3613-3618.

[34] H. Xia, S. Tang, L. Lu. *Materials Research Bulletin*, **2007**, 42, 1301-1309.

[35] L. B. Chen, J. Y. Xie, H. C. Yu, T. H. Wang. *J. Appl. Electrochem.*, **2009**, 39, 1157-1762.

[36] L. F. Cui, R. Ruffo, C. K. Chan, H. L. Peng, Y. Cui. *Nano lett.*, **2009**, 9, 491-495.

[37] J. Wang, N. Du, Z. Song, H. Wu, H. Zhang, D. Yang. *RSC Advances*, **2013**, 3, 7543-7548.

Chapter 6 Conclusions

In conclusion, large-area and uniform 2D MoS_2 atomic layer was successfully synthesized by simple direct sulfurization of pre-deposited MoO_3 thin film on SiO_2/Si substrate. The Raman peaks of the as-synthesized MoS_2 atomic layer shifted towards each other when the thickness decreased. Both Raman spectroscopy and AFM measurements suggested bi-layer thickness of the MoS_2 atomic layer synthesized from 1 nm pre-deposited MoO_3 thin film. While the MoS_2 synthesized from 10 nm MoO_3 thin film showed no PL signals, the one prepared from 1 nm MoO_3 thin film showed a pronounced PL peak at 652 nm indicating direct excitonic transition of the MoS_2 atomically thin layer. Moreover, the intensity of the MoS_2 PL peak increased with the synthesis temperature, suggesting higher quality of the MoS_2 atomic layer from higher synthesis temperature.

CVD method was conducted to prepare 2D MoS_2 atomic layer at various synthesis pressures in order to investigate the growth behavior of MoS_2. At vacuum, large-area and uniform 2D MoS_2 layer can be prepared if sufficient amount of S vapor was supplied. At ambient pressure, rhombic $MoOS_2$ microplates were formed despite varying the S vapor supply. At higher pressure of 900 Torr, bi-layered MoS_2 triangular flakes with size ~20 μm were successfully synthesized. The OM images revealed the nucleation sites for the MoS_2 growth located at the center of each triangular flake.

Large-area MoS_2 atomic layer with tens of micrometer grain size can be formed when individual MoS_2 triangular flakes grew and merged with each other. The emerging of PL peaks suggested direct excitonic transition of the as-synthesized MoS_2 triangular flakes.

MoS_2 nanospheres were synthesized by facile and scalable hydrothermal reaction with the assist of PVP. The size of the nanospheres decreased with increasing the PVP concentration and 80 nm diameter nanospheres can be prepared in this work. The MoS_2 nanospheres were characterized to have randomly oriented layers with expanded interlayer separation in the (002) plane and the nanospheres interlinked with each other forming a network. LIB anode based on the as-synthesized MoS_2 network exhibited enhanced electrochemical performance in terms of cyclability, rate capability and stability. The enhancement can be attributed to the unique structure of the nanosphere network where the small nanosphere size provided short Li-ion diffusion pathways, the interlinked network facilitated efficient electron transport and the expanded interlayer spacing offered fast Li-ion diffusion channels. Moreover, the MoS_2 nanosphere network showed significant enhancement for HER. The enhancement can be ascribed to the expanded interlayer distance in the (002) plane which exposed more reactive edge sites for electrochemical reactions.

Porous Cu supported Si nanostructure was fabricated through PS nanosphere template assisted growth of porous Cu current collector and subsequent deposition of Si thin film. LIB anode based on the porous Cu supported Si nanostructure exhibited superior electrochemical performance in terms of high specific capacity, long term cyclability and high rate capability. The electrochemical enhancement can be attributed to the unique design of the porous structure which provided empty space for Si strain relaxation during cycling and offered large surface area for Li-Si reactions, as well as efficient electron transport facilitated from the interconnected porous Cu current collector.

Prospective future works can be devoted to the doping and functionalization of the 2D MoS_2 atomic layers for novel electronic and optoelectronic applications. The exploration of catalytic substrates for the synthesis of high quality 2D MoS_2 is also a future prospect. Since Si has the highest specific capacity and MoS_2 has good mechanical properties, core-shell Si-MoS_2 composite nanomaterial is promising to realize higher performance LIB. The electrocatalytic activity of MoS_2 nanospheres for HER can be further enhanced by optimizing the exposure of reactive edge sites, which can be achieved by expanding the interlayer spacing of MoS_2 through Li-ion intercalation.

Appendix: Publication List

1. **Ying-San Chui**, Chundong Wang, Jian-Guo Ren, Wenjun Zhang. Three-dimensional porous copper supported silicon as high performance lithium-ion battery anodes. *in manuscript*.
2. **Ying-San Chui**, Chundong Wang, Zhenyu Zhang, Wenjun Zhang. Facile synthesis of MoS_2 nanospheres as lithium-ion battery anode material with enhanced electrochemical performance. *in manuscript*.
3. Yucheng Dong, **Ying-San Chui**, Ruguang Ma, Chenwei Cao, Hua Cheng, Yang Yang Li, Juan Antonio Zapien. One-pot scalable synthesis of Cu-$CuFe_2O_4$/graphene composites as anode materials for lithium-ion batteries with enhanced lithium storage properties. ***J. Mater. Chem. A***, in press.
4. Yucheng Dong, Chenwei Cao, **Ying-San Chui**, Juan Antonio Zapien. Facile hydrothermal synthesis of $CuFe_2$ hexagonal platelets/rings and graphene composites as anode materials for lithium ion batteries. ***Chem. Comm.***, in press.
5. Chundong Wang, **Ying-San Chui**, Yi Li, Xianfeng Chen, Wenjun Zhang. Binder-free Ge-three dimensional graphene electrodes for high-rate capacity Li-ion batteries. ***Appl. Phys. Lett.***, 2013, 103, 253903.
6. Chundong Wang, **Ying-San Chui**, Ruguang Ma, Tailun Wong, Jian-Guo Ren, Qi-Hui Wu, Xianfeng Chen, Wenjun Zhang. A three-dimensional graphene

scaffold supported thin film silicon anode for lithium-ion batteries. ***J. Mater. Chem. A***, 2013, 1, 10092-10098.

7. Chundong Wang, Yi Li, **Ying-San Chui**, Qi-Hui Wu, Xianfeng Chen, Wenjun Zhang. Three-dimensional Sn–graphene anode for high-performance lithium-ion batteries. ***Nanoscale***, 2013, 5, 10599-10604.
8. Jing Li, Chuang Yue, Yingjian Yu, **Ying-San Chui**, Jun Yin, Zhenguo Wu, Chundong Wang, Yashu Zang, Wei Lin, Juntao Li, Suntao Wu, Qihui Wu. Si/Ge core–shell nanoarrays as the anode material for 3D lithium ion batteries. ***J. Mater. Chem. A***, 2013, 1, 14344-14349.
9. Yang Yang, Jian-Guo Ren, Xin Wang, **Ying-San Chui**, Qi-Hui Wu, Xianfeng Chen, Wenjun Zhang. Graphene encapsulated and SiC reinforced silicon nanowires as an anode material for lithium ion batteries. ***Nanoscale***, 2013, 5, 8689-8694.
10. Jian-An Huang, Ying-Qi Zhao, Xue-Jin Zhang, Li-Fang He, Tai-Lun Wong, **Ying-San Chui**, Wen-Jun Zhang, Shuit-Tong Lee. Ordered Ag/Si Nanowires Array: Wide-Range Surface-Enhanced Raman Spectroscopy for Reproducible Biomolecule Detection. ***Nano Lett.***, 2013, 13 (11), 5039–5045.